Section 3   Optics and Devices

Chapter 1 Optics and Quantum Electronics

Chapter 2 Optical Propagation and Communication

Chapter 3 High-Frequency (> 100 GHz) and High-Speed
(< 10 ps) Electronic Devices

Chapter 1. Optics and Quantum Electronics

Academic and Research Staff

Professor Hermann A. Haus, Professor Erich P. Ippen, Professor James G. Fujimoto, Professor Peter L. Hagelstein, Dr. Brett E. Bouma

Visiting Scientists and Research Affiliates

Dr. Mark E. Brezinski,[1] Dr. Brent E. Little, Dr. Shu Namiki, Dr. Viktor P. Mikhailov,[2] Dr. Martin H. Muendel,[3] Dr. Shu Namiki, Dr. Günter Steinmeyer, William Hodge[4]

Graduate Students

Igor P. Bilinsky, Luc Boivin, Stephen A. Boppart, Jerry C. Chen, Patrick Chou, Leo Chun, Jay N. Damask, Ali M. Darwish, David J. Dougherty, Siegfried B. Fleischer, Marc Fleury, Boris Golubovic, James G. Goodberlet, Matthew Grein, Michael R. Hee, David J. Jones, Sumanth Kaushik, Mohammed J. Khan, Farzana I. Khatri, Gadi Lenz, Lynn E. Nelson, Timothy A. Savas, Guillermo J. Tearney, Eric R. Thoen, Constantine Tziligakis, William S. Wong, Charles Yu

Technical and Support Staff

Mary C. Aldridge, Donna L. Gale, Cynthia Y. Kopf

1.1 Fiber Ring Lasers

Sponsors

Defense Advanced Research Projects Agency/
    MIT Lincoln Laboratory
    Contract MDA972-92-J-1038
Joint Services Electronics Program
    Grant DAAH04-95-1-0038
National Science Foundation
    Grant ECS 94-23737
U.S. Air Force - Office of Scientific Research
    Contract F49620-95-1-0221

Project Staff

Professor Hermann A. Haus, Professor Erich P. Ippen, Matthew Grein, David J. Jones, Lynn E. Nelson, William S. Wong

In the past several years, we have constructed and improved the operation of mode-locked fiber ring lasers in general, stretched pulse fiber ring lasers operating at 1.5 μm wavelength, in particular. The fiber ring lasers are modelocked via intensity-dependent polarization rotation followed by an analyzer, resulting in an effective saturable absorber action. This mechanism is now known as polarization additve-pulse modelocking (P-APM). In the stretched pulse laser, two segments of fiber are used, one of positive dispersion, the other of negative dispersion, the net dispersion being close to zero. The pulse stretches and contracts alternately as it propagates around the loop. Its average intensity is much lower than its peak intensity, and thus the nonlinear effects in the fiber are greatly reduced. Since excessive nonlinearity leads to pulse instabilities, this design of the laser is able to produce much shorter pulses of much higher intensity than any other all-fiber laser. When the polarizer is replaced by a polarization beam splitter (see figure 1), the power normally absorbed in a polarizer, is available as output power. Since up to 50 percent of the power ends up in this polarization, very large output powers can be achieved this way. The output of a stretched pulse laser operated in this manner is two orders of magnitude higher than that of a regular all-fiber ring laser. The pulse shape and spectrum, while not as clean as that in the

---

1 Massachusetts General Hospital, Boston, Massachusetts.

2 International Laser Center, Minsk, Belarus.

3 Polaroid Corporation, Cambridge, Massachusetts.

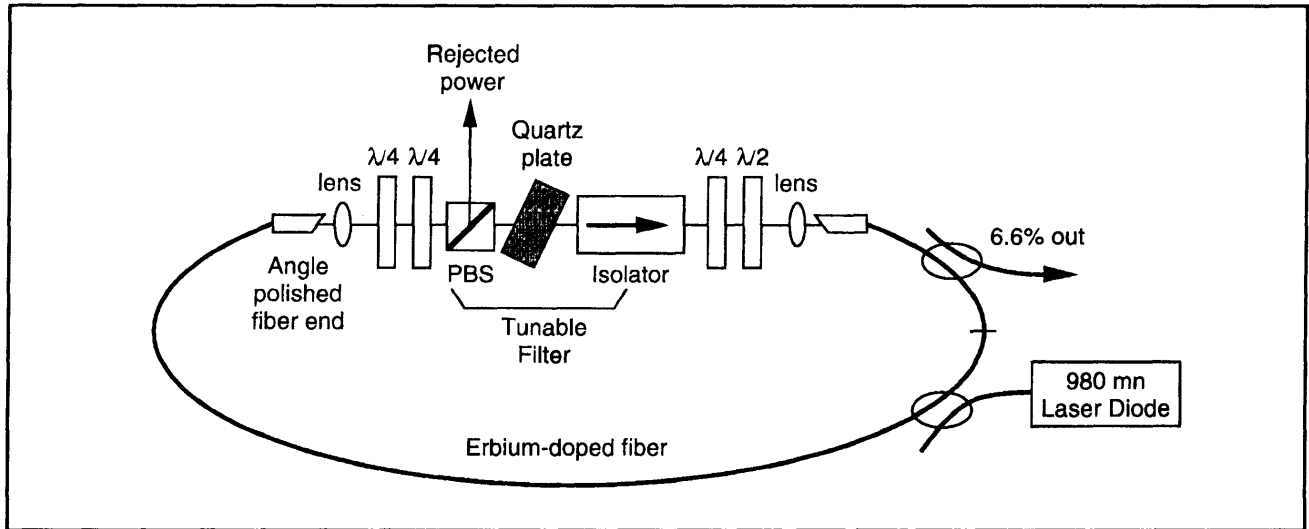4 High Energy Laser Associates, Oakland, California.

Figure 1. Schematic of stretched pulse laser with bulk output coupler.

dominant polarization, is adequate for most applications.[5]

In order to show that the P-APM modelocking scheme is not unique to the erbium doped system, we designed and operated a thulium doped fiber laser,[6] which operates near 1.8 μm. Draper Laboratories has expressed interest in this wavelength regime for fiber gyro applications, and there are possible applications in medicine and eye-safe laser radar. The laser produced sub-500 fs pulses that were broadly tunable from 1798 nm to 1902 nm, with continuous tuning of 50 nm possible by filter adjustment only. Both the thulium-doped fiber and the passive fiber have large negative dispersion in this wavelength region, thus forcing the laser to operate in the soliton regime where the shortest pulse width is limited by continuum generation. Future work may include improved filtering to smooth the pulse spectrum and attempting to stretch the pulse in order to avoid the soliton regime.

Graduate student C.R. Doerr discovered a new actively modelocked system, the asynchronously modelocked fiber ring laser running near 1 GHz, during the previous year. Under normal circumstances (synchronous modelocking), the RF drive to the modulator in the fiber ring laser must be precisely a harmonic of the roundtrip frequency. In the asynchronous laser the phase modulator is detuned 15-30 kHz from a cavity harmonic. The soliton nature of the pulses enable them to survive this detuned modulation. The value of the asynchronous system is that it needs no stabilization of the cavity length with respect to the modelocking drive. With extensive numeric simulations confirmed by both analytic theory and experimental results, we have gained a thorough understanding of the asynchronous modelocking process.[7] In particular, we have found it possible to implement asynchronous modelocking in polarization maintaining (PM) fiber for increased environmental stability. For this reason, it is our intent in the coming year to develop both asynchronous and passively modelocked versions of fiber lasers using PM fiber.

5 K. Tamura, E.P. Ippen, and H.A. Haus, "Pulse Dynamics in Stretched-Pulse Fiber Lasers," Appl. Phys. Lett. 67: 158 (1995); H.A. Haus, K. Tamura, L.E. Nelson, and E.P. Ippen, "Stretched-Pulse Additive Pulse Mode-Locking in Fiber Ring Lasers: Theory and Experiment," IEEE J. Quant. Electron. 31: 591 (1995); G. Lenz, K. Tamura, H.A. Haus, and E.P. Ippen, "All-Solid-State Femtosecond Source at 1.55 μm," Opt. Lett. 20: 1289 (1995).

6 L.E. Nelson, E.P. Ippen, and H.A. Haus, "Broadly Tunable Sub-500 fs Pulses from an Additive-Pulse Mode-Locked Thulium-Doped Fiber Ring Laser," Appl. Phys. Lett. 67: 19 (1995).

7 H.A. Haus, D.J. Jones, E.P. Ippen, and W.S. Wong, "Theory of Soliton Stability in Asynchronous Modelocking," J. Lightwave Technol., forthcoming.

1.1.1 Publications

Haus, H.A., K. Tamura, L.E. Nelson, and E.P. Ippen. "Stretched-Pulse Additive Pulse Mode-Locking in Fiber Ring Lasers: Theory and Experiment." *IEEE J. Quant. Electron.* 31: 591 (1995).

Haus, H.A., D.J. Jones, E.P. Ippen, and W.S. Wong. "Theory of Soliton Stability in Asynchronous Modelocking." *J. Lightwave Technol.* Forthcoming.

Lenz, G., K. Tamura, H.A. Haus, and E.P. Ippen. "All-Solid-State Femtosecond Source at 1.55 μm." *Opt. Lett.* 20: 1289 (1995).

Nelson, L.E., E.P. Ippen, and H.A. Haus. "Broadly Tunable Sub-500 fs Pulses from an Additive-Pulse Mode-Locked Thulium-Doped Fiber Ring Laser." *Appl. Phys. Lett.* 67: 19 (1995).

Tamura, K., E.P. Ippen, and H.A. Haus. "Pulse Dynamics in Stretched-Pulse Fiber Lasers." *Appl. Phys. Lett.* 67: 158 (1995).

1.2 Fiber Storage Rings

Sponsors

Defense Advanced Research Projects Agency/
MIT Lincoln Laboratory
Contract MDA972-92-J-1038
U.S. Air Force - Office of Scientific Research
Contract F49620-95-1-0221

Project Staff

Professor Hermann A. Haus, Professor Erich P. Ippen, William S. Wong

For high bit-rate optical communications, storage and buffering of data at communication nodes is a necessity.[8] With this purpose in mind, we are working on the storage of bits in optical fiber rings. The fiber storage ring demonstrated last year operated at 1 GHz, which required electro-optic amplitude modulation to provide timing stability. A data pattern of 66 bits (ones and zeros) loaded into the ring could be maintained for at least 30 minutes inside the ring.

Graduate student William Wong, working with MIT Lincoln Laboratory researchers, extended the data rate to 20 Gb/s.[9] All-optical long-term storage at 10 Gb/s has also been demonstrated using cross-gain saturation in a semiconductor amplifier to provide the optical modulation.[10]

Using the new technique of rational-harmonic modelocking, where the ratio of the fundamental modulation frequency to the cavity fudamental frequency is rational (nonintegral), 3.8-kbit packets of data can be stored at 50 Gb/s.[11] This method offers the advantage of achieving storage at bit rates a few times that of the modelocking drives. In the near future, we shall attempt to scale the operation to even higher frequencies and to produce streams as well as patterns of ones and zeros.

1.2.1 Publications

Hall, K.L., J.D. Moores, K.A. Rauschenbach, W.S. Wong, E.P. Ippen, and H.A. Haus. "All-Optical Storage of a 1.25 kb Packet at 10 Gb/s." Paper published in the *Conference on Lasers and Electro-Optics.* OSA Technical Digest Series. Washington, D.C.: Optical Society of America, 1995, paper CPD16.

Hall, K.L., J.D. Moores, K.A. Rauschenbach, W.S. Wong, E.P. Ippen, and H.A. Haus. "All-Optical Storage of a 1.25 kb Packet at 10 Gb/s." *IEEE Photon. Technol. Lett.* 7: 1093 (1995).

---

8 K. Rauschenbach, K. Hall, J. Moores, E. Swanson, M. Haner, H.A. Haus, and W. Wong, "Broadband Optical Local Area Network Technologies," in *Digest of IEEE LEOS'94 7th Annual Meeting* (New York: Institute of Electrical and Electronics Engineers, 1994), paper UO4.1; K.A. Rauschenbach, K.L. Hall, J.D. Moores, S.G. Finn, R.A. Barry, W. Wong, H.A. Haus, E.P. Ippen, and M. Haner, "Technologies for Ultra-High-Bit-Rate Time-Division-Multiplexed Networks," *OSA Photonics in Switching Digest '95* 12: 45 (1995).

9 J.D. Moores, K.L. Hall, S.M. LePage, K.A. Rauschenbach, W.S. Wong, H.A. Haus, and E.P. Ippen, "20-GHz Optical Storage Loop/-Laser using Amplitude Modulation, Filtering, and Artificial Fast Saturable Absorption," *IEEE Photon. Technol. Lett.* 7: 1096 (1995).

10 K.L. Hall, J.D. Moores, K.A. Rauschenbach, W.S. Wong, E.P. Ippen, and H.A. Haus, "All-Optical Storage of a 1.25 kb Packet at 10 Gb/s," in *Conference on Lasers and Electro-Optics,* OSA Technical Digest Series (Washington, D.C.: Optical Society of America, 1995), paper CPD16; K.L. Hall, J.D. Moores, K.A. Rauschenbach, W.S. Wong, E.P. Ippen, and H.A. Haus, "All-Optical Storage of a 1.25 kb Packet at 10 Gb/s," *IEEE Photon. Technol. Lett.* 7: 1093 (1995).

11 J.D. Moores, W.S. Wong, and K.L. Hall, "50 Gb/s Optical Pulse Storage Ring Using Novel Rational-Harmonic Modulation," *Opt. Lett.* 20: 2547 (1995).

Moores, J.D., K.L. Hall, S.M. LePage, K.A. Rauschenbach, W.S. Wong, H.A. Haus, and E.P. Ippen. "20-GHz Optical Storage Loop/Laser using Amplitude Modulation, Filtering, and Artificial Fast Saturable Absorption." *IEEE Photon. Technol. Lett.* 7: 1096 (1995).

Rauschenbach, K.A., K.L. Hall, J.D. Moores, S.G. Finn, R.A. Barry, W. Wong, H.A. Haus, E.P. Ippen, and M. Haner. "Technologies for Ultra-High-Bit-Rate Time-Division-Multiplexed Networks." *OSA Photonics in Switching Digest* 12: 45 (1995).

1.3 Long-Distance Fiber Communications

Sponsors

Project Staff

Professor Hermann A. Haus, Farzana I. Khatri, William S. Wong

We continue to pursue theory and numerical simulation of phenomena occuring in long-distance soliton communications. We developed a simple theory of continuum generation by soliton disturbances (such as lumped gain, lumped Kerr effect, lumped filtering).[12] The continuum can affect another soliton in in a bit-stream formed of soliton ONEs and ZEROs (a ZERO is a gap with no soliton pulse present). Quantitatively, we have evaluated the amount of displacement caused by a wave packet of low intensity colliding with a soliton.[13] For example, in figure 2 we show the timing shift as a function of distance due to a soliton colliding with an asymmetric Hermite Gaussian wave packet (shown in figure 2 inset). Theory and simulation are shown by solid and dashed lines, respectively.

In 1995, Professor Haus spent two months at AT&T Bell Laboratories as part of his one-term sabbatical. In collaboration with Drs. W.H. Knox and D.A.B.
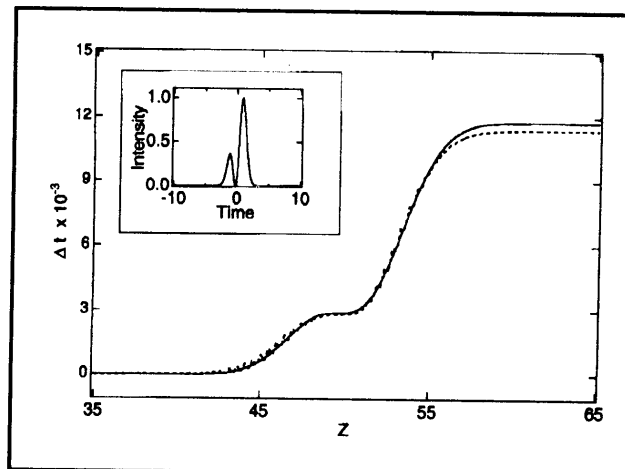

Figure 2. The timing shift due to a collision between a soliton and a low-intensity, asymmetric Hermite Gaussian wave packet. Solid and dashed lines represent theory and simulation, respectively. The inset shows the intitial perturbation as a function of time.

Miller, a scheme was developed that would replace the sliding-frequency guiding filters for soliton stabilization which have been proposed and demonstrated by Mollenauer and Gordon. The disadvantage of sliding-guiding filters is the requirement that each undersea amplification "pod" be equipped with a filter tuned to a different frequency. Our new scheme acts as an effective saturable absorber with all its pods identical. A patent application has been filed.

Another issue confronting long distance soliton communication vis á vis the successfully deployed non-return to zero (NRZ) systems is line monitoring (LM), or supervisory control. In an NRZ system, a low-intensity, low-bit-rate modulation is applied to the high bit-rate pulse stream. A very small fraction of the signal is tapped off at each amplifier stage and returned in the opposite direction. This signal is then processed in order to determine the location of faulty amplifiers or fiber breaks. The NRZ LM scheme is, however, incompatible with nonlinear soliton communications, since low level signals are automatically suppressed.

A soliton LM scheme was developed by Professor Haus, in collaboration with Drs. Stephen Evangelides and Bruce Nyman of AT&T Bell Laborato-

---

[12] H.A. Haus, W.S. Wong, and F.I. Khatri, "Continuum Generation by Perturbation of Soliton," submitted to *J. Opt. Soc. Am. B.*

[13] H.A. Haus, F.I. Khatri, W.S. Wong, K.R. Tamura, and E.P. Ippen, "Interaction of Soliton with Sinusoidal Wave Packet," *J. Quantum Electron.*, forthcoming; H.A. Haus, F.I. Khatri, and W.S. Wong, "Soliton Interaction with Continuum," paper presented at the Conference on Ultrafast Transmission Systems in Optical Fibres, Trieste, Italy, February 1995; H.A. Haus, E.P. Ippen, W.S. Wong, F.I. Khatri, and K.R. Tamura, "Pulse Self-Ordering in Soliton Fiber Lasers," Conference on Lasers and Electro-Optics, Baltimore, Maryland, May 1995, paper JTuA7.
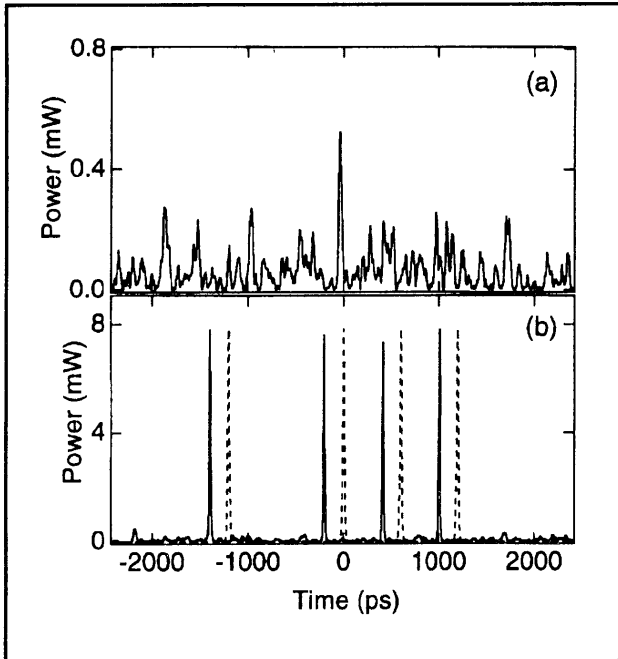
Figure 3. (a) and (b) show simulation results for loop-back "1" and "2." Shown in (b) are the input (dashed) and output (solid) pulse power versus time. Note that we have time shifted loop-back "2" for aesthetic purposes.

ries and graduate student Farzana Khatri.[14] In our scheme, the LM is a separate channel which employs a low-bit-rate wavelength division multiplexed (WDM) channel of soliton pulses encoded with a pseudorandom bit pattern. The couplers employed are stronger than their NRZ counterpart and are located so that the gain is maximized. In addition, the fiber dispersions may be arranged so that the LM experiences "reflective gain" on the return and so that the east- and west-going data channels are spectrally separated, eliminating crosstalk. Results from a simulation of our LM scheme are shown in figure 3. Figure 3a shows the LM signal returning from a degraded amplification stage, while figure 3b shows the LM signal

returning from a normal amplification stage. A patent application has been filed.

1.3.1 Publications

Haus, H.A., W.S. Wong, and F.I. Khatri. "Continuum Generation by Perturbation of Soliton." Submitted to *J. Opt. Soc. Am. B.*

Haus, H.A., F.I. Khatri, and W.S. Wong. "Soliton Interaction with Continuum." Paper presented at the Conference on Ultrafast Transmission Systems in Optical Fibres, Trieste, Italy, February 1995.

Haus, H.A., E.P. Ippen, W.S. Wong, F.I. Khatri, and K.R. Tamura. "Pulse Self-Ordering in Soliton Fiber Lasers." Conference on Lasers and Electro-Optics, Baltimore, Maryland, May 1995, paper JTuA7.

Haus, H.A., W.S. Wong, and F.I. Khatri. "Continuum Generation by Perturbation of Soliton." Submitted to *J. Opt. Soc. Am. B.*

Khatri, F.I., S.G. Evangelides, P.V. Mamyshev, B.M. Nyman, and H.A. Haus. "A Line-Monitoring System for Undersea Soliton Communication Systems with Sliding-Frequency Guiding Filters." Paper presented at the Optical Fiber Communication Conference '96, San Jose, California, February 1996, paper ThH6.

Khatri, F.I., S.G. Evangelides, P.V. Mamyshev, B.M. Nyman, and H.A. Haus. "A Line-Monitoring System for Undersea Soliton Communication Systems with Sliding-Frequency Guiding Filters." Submitted to *IEEE Photon. Technol. Lett.*

Haus, H.A., F.I. Khatri, W.S. Wong, K.R. Tamura, and E.P. Ippen. "Interaction of Soliton with Sinusoidal Wave Packet." *J. Quantum Electron.* Forthcoming.

---

[14] F.I. Khatri, S.G. Evangelides, P.V. Mamyshev, B.M. Nyman, and H.A. Haus, "A Line-Monitoring System for Undersea Soliton Communication Systems with Sliding-Frequency Guiding Filters," paper ThH6, Optical Fiber Communication Conference '96, San Jose, California, February 1996; F.I. Khatri, S.G. Evangelides, P.V. Mamyshev, B.M. Nyman, and H.A. Haus, "A Line-Monitoring System for Undersea Soliton Communication Systems with Sliding-Frequency Guiding Filters," submitted to *IEEE Photon. Technol. Lett.*

1.4 Laser Noise and Squeezing

Project Staff

Professor Hermann A. Haus, Professor Erich P. Ippen, Luc Boivin, Dr. Shu Namiki, Charles Yu

The eventual goal of our squeezing experiments is to develop an all-fiber squeezing system compatible with a fiber gyro for improved gyro sensitivity. Squeezing experiments were performed with GHz rate pulses from a compact Ti:Sapphire laser in the positive dispersion regime of the fiber. The GHz rate is required to suppress the effect of guided acoustic wave Brillouin scattering (GAWBS).[15] The sub-shot noise level was inadequate, mainly due to the amplitude fluctuations of the source. Future work requires better control of the fluctuations of the pulses emitted from a modelocked laser.

In an attempt to develop low-noise sources of modelocked pulses, we have begun a theoretical and experimental study of noise in fiber ring lasers. If used for squeezing experiments, they would be an ideal source for soliton squeezing in the 1.5 μm wavelength regime. We found that timing jitter in these lasers is quantum limited, i.e., due solely to the spontaneous emission noise of the laser amplifier. It is the first demonstration of a quantum limited modelocked operation.[16] The amplitude fluctuations were also found to be lower (0.2 percent) than reported in any other laser system.

The use of short and intense pulses to generate squeezed light in optical fibers is very attractive since large nonlinear shifts can then be achieved using very short fibers. Pulses shorter than about 1

ps are, however, affected by stimulated Raman scattering. The impact of Raman noise on short pulse squeezing was analyzed at zero dispersion[17] and was shown to be surmountable.[18]

In order to design the positive dispersion Ti:sapphire squeezer, a numerical code based on the symmetrized split-step method was developed to evolve both the pump and the quantum noise. Some of our results were published[18] and show that large degrees of squeezing can be achieved over a few centimeters using typical modelocked Ti:sapphire systems.

A possible approach to squeezed fiber gyro makes use of optical solitons. In one of our theoretical projects, we calculated the degree of squeezing for fundamental solitons without using the small quantum noise approximation. This analysis, based on the exact time dependence of the Bethe eigenstates for the quantized nonlinear Schrödinger equation, confirms the results of the linearized theory and establishes its domain of validity.[19] The fluctuations of the position and of the phase of a fundamental soliton were also shown to be limited by the lower bound of the Heisenberg uncertainty relations.

We proposed a new method to generate squeezed light using an optical fiber.[20] Contrary to prevous approaches using the self-phase modulation experienced by intense pulses in these waveguides, the new method relies on cross-phase modulation between pulses with orthogonal polarizations. As the squeezed vacuum and the pump are not degenerate in polarization, they can be easily separated without using a Sagnac interferometer. This feature of the new squeezer leads to a simpler design.

The ultimate limit of noise suppression in squeezing experiments is set by the quantum efficiency of the photo-detectors. If the quantum efficiency is 90 percent, the maximum shot noise suppression pos-

---

[15] R.M. Shelby, M.D. Levenson, S.H. Perlmutter, R.G. DeVoe, and D.F. Walls, *Phys. Rev. Lett.* 54: 691 (1986); K. Bergman, H.A. Haus, and M. Shirasaki, "Analysis and Measurement of GAWBS Spectrum in a Nonlinear Fiber Ring," *Appl. Phys. B* 55: 242 (1992).

[16] S. Namiki, C.X. Yu, and H.A. Haus, "Observation of Nearly Quantum-Limited Timing Jitter in an All-Fiber Ring Laser," submitted to *J. Opt. Soc. Am. B.*

[17] J.H. Shapiro and L. Boivin, "Raman Noise Limit for Four-Wave Mixing," *Opt. Lett.* 18: 925 (1994); L. Boivin, "Sagnac Loop Squeezer at Zero Dispersion with a Finite Response Time for Kerr Nonlinearity," *Phys. Rev. A* 52: 754 (1995).

[18] L. Boivin, C.R. Doerr, K. Bergman, and H.A. Haus, "Quantum Noise Reduction Using a Sagnac Loop with Positive Dispersion," in *Quantum Communications and Measurement,* eds. V.P. Belavkin, O. Hirota, and R.L. Hudson (New York: Plenum Press, 1995), pp. 489-496.

[19] F.X. Kärtner and L. Boivin, "Quantum Noise of the Fundamental Soliton," *Phys. Rev. A* 53 (1996), forthcoming.

[20] L. Boivin and H.A. Haus, "$\chi^{(3)}$-Squeezed Vacuum Generation Without a Sagnac Interferometer," *Opt. Lett.* 21 (1996), forthcoming.

sible is 10 dB. Hence, one may raise the question whether there are ways to overcome this limit. Since phase sensitive amplification can be made noise-free in the ideal limit, we investigated the possibility of phase sensitive preamplification in the spirit of a quantum nondemolition measurement of the twin beams detected in the balanced detector.[21] We found that it is possible to use preamplification, with realistic pump power levels and fiber lengths, to overcome the limits set by the detector quantum efficiency.

1.4.1 Publications

Boivin, L., and H.A. Haus. "$\chi^{(3)}$-Squeezed Vacuum Generation Without a Sagnac Interferometer." *Opt. Lett.* 21 (1996). Forthcoming.

Boivin, L. "Sagnac Loop Squeezer at Zero Dispersion with a Finite Response Time for Kerr Nonlinearity." *Phys. Rev. A* 52: 754 (1995).

Boivin, L., C.R. Doerr, K. Bergman, and H.A. Haus. "Quantum Noise Reduction Using a Sagnac Loop with Positive Dispersion." In *Quantum Communications and Measurement.* Eds. V.P. Belavkin, O. Hirota, and R.L. Hudson. New York: Plenum Press, 1995, pp. 489-496.

Kärtner, F.X., and L. Boivin. "Quantum Noise of the Fundamental Soliton." *Phys. Rev. A* 53 (1996). Forthcoming.

Namiki, S., C.X. Yu, and H.A. Haus. "Observation of Nearly Quantum-Limited Timing Jitter in an All-Fiber Ring Laser." Submitted to *J. Opt. Soc. Am. B.*

1.5 Optical Waveguide Filters

Sponsors

MIT Center for Material Science and Engineering
National Center for Integrated Photonics
  Technology
  Contract DMR 94-00334

National Science Foundation
  Grant ECS 94-23737

Project Staff

Professor Hermann A. Haus, Jerry C. Chen, Mohammed J. Khan, Dr. Brent E. Little

For some years, we have been developing the theory and perfecting the fabrication of filters using passive waveguide gratings. Active filters, while more difficult to fabricate, have many desirable properties. For instance, suppression of undesirable modes is more effective in active filters. A detailed theory of active filters has been published.[22]

We have started to investigate traveling-wave ring resonators as alternatives to quarter-wave-shifted grating resonators for filtering applications. The basic idea originated with Marcatilli[23] in 1969. Since then, fabrication has advanced to a point where adequate Qs can be expected. A ring resonator placed between two waveguides is capable of transfering all the power from one waveguide to another waveguide at a particular wavelength. This is not possible using a single resonator with standing wave resonances. Figure 4 shows a ring resonator and its characteristic narrow band response.[24] Utilizing the Vernier effect of two resonators of different dimensions with one coincident resonator frequency, the free spectral range can be extended. Figure 5 shows such a Vernier filter using rings of different radii. Cascading of ring resonators can lead to the synthesis of desirable filter characteristics, such as Butterworth and Chebyshev response.

Waveguides with large index discontinuities similar to that of photonic bandgap materials can provide large filter bandwidths and large free spectral ranges compatible with optical communication channels of 10 Gbit and 100 GHz spacings. For this reason, we are investigating the design of waveguide-resonator structures that suppress radiation adequately, an unavoidable effect in such compact, open (unshielded) resonator structures.

21 F.X. Kärtner and H.A. Haus, "QND - Measurement of Twin Beams," submitted to *J. Opt. Soc. Am. B.*

22 H.A. Haus and M.J. Khan, "Gain-Distributed Feedback Filters," *J. Lightwave Technol.* 13: 261-274 (1995).

23 E.A.J. Marcatilli, "Bends in Optical Dielectric Waveguides," *Bell Syst. Tech. J.* 14: 2103 (1969).

24 B.E. Little, S.T. Chu, and H.A. Haus, "Micro-Ring Resonator Channel Dropping Filters," *IEEE/LEOS Annual Meeting,* San Francisco, California, 1995, paper WDM 2.3.
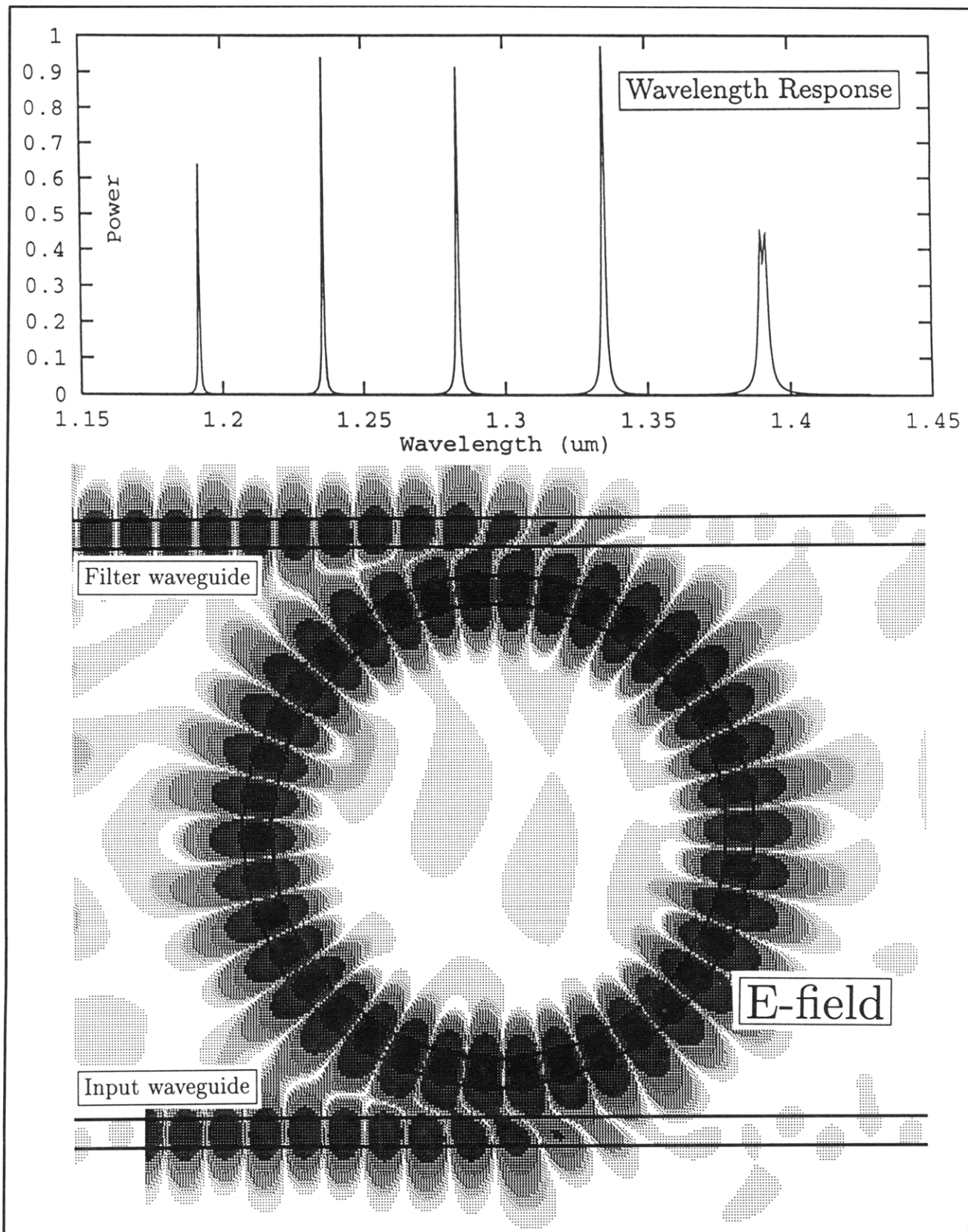
Figure 4. Wavelength response of a single-ring resonator. The upper graph shows the sharp, narrow band peaks at the channel dropping wavelengths. The lower graph is a plot of electric field intensity in the micro-ring resonator at a particular resonator wavelength.
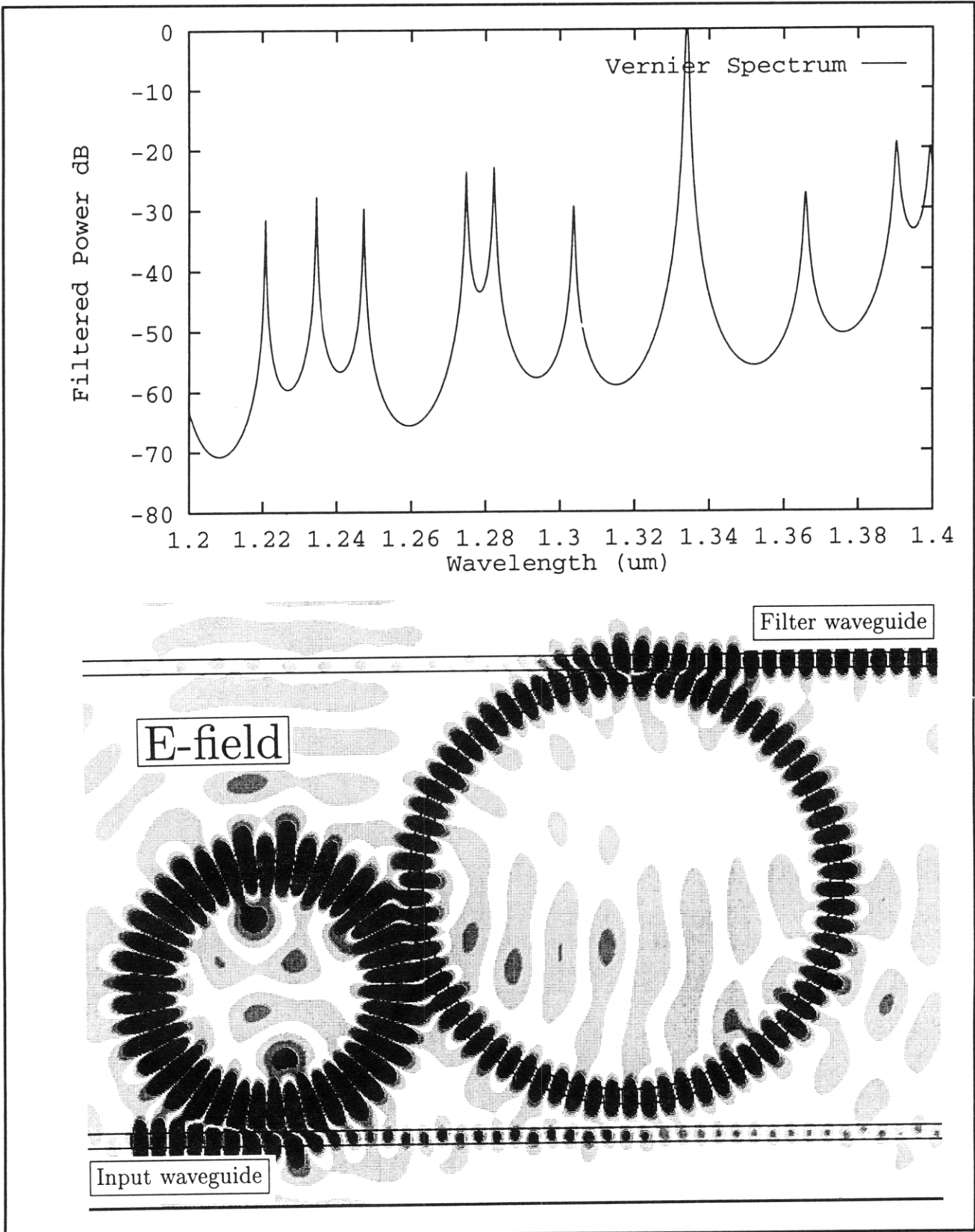
Figure 5. Vernier ring resonator using two dissimilar rings. The upper graph shows the wavelength response. Of the multiple resonator peaks shown, only one at $\lambda = 1.334\,\mu m$ is completely extracted by the filter. Other peaks are suppressed by -25 dB by the Bernier effect. The lower graph shows the electric field intensity in the filter.

We have developed designs for 1.5 μm applications that provide a Q as high as 24,000 in structures that are only 18 μm long[25] (see figure 6). An analytic theory has been developed to take into account higher order effects in deeply etched gratings, such as resonator frequency shifts and radiation loss.[26]

1.5.1 Publications

Chen, J.C., H.A. Haus, S. Fan, and J.D. Joannopoulos. "Optical Filters from Photonic Band Gap Air Bridges." European Conference on Integrated Optics, Delft, The Netherlands, 1995, paper ThC3.

Chen, J.C., H.A. Haus, S. Fan, P.R. Villeneuve, J.D. Joannopoulos, K. Li, and R.T. Shin. "Optical Filters from Photonic Band Gap Air Bridges." *Proceedings of the Photonics Society of the Chinese-Americans Annual Meeting* Baltimore, Maryland, 1995.

Chen, J.C., H.A. Haus, J. N. Winn, S. Fan, and J.D. Joannopoulos. "Wide Stop Band Optical Filters from Photonic Band Gap Air Bridges," in *Guided-Wave Optoelectronics: Device Characterization, Analysis, and Design.* New York: Plenum Press, 1995, pp. 477-483.

Chen, J.C., and K. Li. "Quartic Perfectly Matched Layers for Dielectric Waveguides and Gratings." *Microwave Opt. Technol. Lett.* 10: 319 (1995).

Chen, J.C., H.A. Haus, S. Fan, P.R. Villeneuve, and J.D. Joannopoulos. "Optical Filters from Photonic Band Gap Air Bridges." Submitted to *J. Lightwave Technol.*

Chen, J.C., P.R. Villeneuve, H.A. Haus, and J.D. Joannopoulos. "Narrow-Band Transmmission Filters from Highly Resonant Gratings." Submitted to the *Topical Meeting on Integrated Photonics Research.*

Fan, S., J.N. Winn, A. Devenyi, J.C. Chen, R.D. Meade, and J.D. Joannopoulos. "Guided and Defect Modes in Periodic Dielectric Waveguides." *J. Opt. Soc. Am. B* 12: 1267 (1995).

Haus, H.A., and M.J. Khan. "Gain-Distributed Feedback Filters." *J. Lightwave Technol.* 13: (1995).

Little, B.E. "A Variational Coupled-Mode Theory Including Radiation Loss for Grating-Assisted Couplers." *IEEE J. Lightwave Technol.* 14 (1996).

Little, B.E., and H.A. Haus. "A Variational Copuled-Mode Theory for Periodic Waveguides." *IEEE J. Quantum Electron.* 31: 2258 (1995).

Villeneuve, P.R., S. Fan, I. Kurland, J.C. Chen, and J.D. Joannopoulos. "Photonic Band Gap Structures and Devices." *Quantum Electronics and Laser Science Conference.* Baltimore, Maryland, 1995, paper QWH1.

Villeneuve, P.R., S. Fan, J.D. Joannopoulos, K.-Y. Lim, J.C. Chen, G.S. Petrich, L.A. Kolodziejski, and R. Reif. "Microcavities in Channel Waveguides." *Proceedings of a NATO Advanced Studies Institute of Photonic Band Gap Materials,* Elounda, Greece, 1995.

[25] J.C. Chen, H.A. Haus, S. Fan, and J.D. Joannopoulos, "Optical Filters from Photonic Band Gap Air Bridges," European Conference on Integrated Optics, Delft, Netherlands, 1995, paper ThC3; J.C. Chen, H.A. Haus, S. Fan, P.R. Villeneuve, J.D. Joannopoulos, K. Li, and R.T. Shin, "Optical Filters from Photonic Band Gap Air Bridges, *Proceedings of the Photonics Society of the Chinese-Americans Annual Meeting* Baltimore, Maryland, 1995; P.R. Villeneuve, S. Fan, I. Kurland, J.C. Chen, and J.D. Joannopoulos, "Photonic Band Gap Structures and Devices," *Quantum Electronics and Laser Science Conference,* Baltimore, Maryland, 1995, paper QWH1; P.R. Villeneuve, S. Fan, J.D. Joannopoulos, K.-Y. Lim, J.C. Chen, G.S. Petrich, L.A. Kolodziejski, and R. Reif, "Microcavities in Channel Waveguides," *Proceedings of a NATO Advanced Studies Institute of Photonic Band Gap Materials,* Elounda, Greece, 1995; S. Fan, J.N. Winn, A. Devenyi, J.C. Chen, R.D. Meade, and J.D. Joannopoulos, "Guided and Defect Modes in Periodic Dielectric Waveguides," *J. Opt. Soc. Am. B* 12: 1267 (1995); J.C. Chen, H.A. Haus, J. N. Winn, S. Fan, and J.D. Joannopoulos, "Wide Stop Band Optical Filters from Photonic Band Gap Air Bridges," in *Guided-Wave Optoelectronics: Device Characterization, Analysis, and Design* (New York: Plenum Press, 1995), pp. 477-483; J.C. Chen and K. Li, "Quartic Perfectly Matched Layers for Dielectric Waveguides and Gratings," *Microwave Opt. Technol. Lett.* 10: 319 (1995); J.C. Chen, H.A. Haus, S. Fan, P.R. Villeneuve, and J.D. Joannopoulos, "Optical Filters from Photonic Band Gap Air Bridges," submitted to *J. Lightwave Technol.*; J.C. Chen, P.R. Villeneuve, H.A. Haus, and J.D. Joannopoulos, "Narrow-Band Transmmission Filters from Highly Resonant Gratings," submitted to the *Topical Meeting on Integrated Photonics Research.*

[26] B.E. Little, "A Variational Coupled-Mode Theory Including Radiation Loss for Grating-Assisted Couplers," *IEEE J. Lightwave Technol.* 14 (1996); B.E. Little and H.A. Haus, "A Variational Copuled-Mode Theory for Periodic Waveguides," *IEEE J. Quantum Electron.* 31: 2258 (1995).
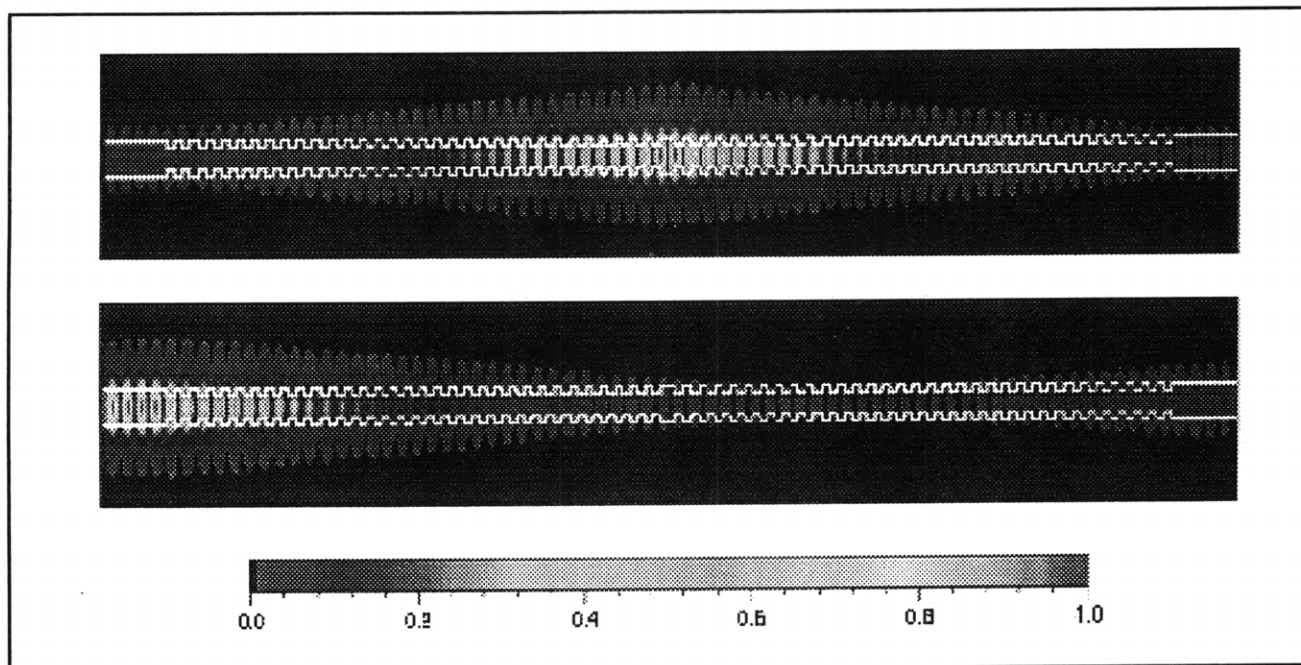
Figure 6. Electric and magnetic field propagating through air bridge filter. Frequency is close to the transmission resonance.

1.6 Integrated Optical Filters and Circuits

Sponsor

National Center for Integrated Photonics
Technology

Project Staff

Professor Hermann A. Haus, Professor Leslie A. Kolodziejski, Professor Henry I. Smith, Jay N. Damask, Juan Ferrera, Mohammed J. Khan, Michael H. Lim, Dr. Brent E. Little, Thomas E. Murphy

The integrated optics program that spans the Optics, Nanostructures, and Chemical-Beam Epitaxy Groups at MIT has significantly expanded this year in both numbers of research staff and in devices being developed. Moreover, the requisite software and theoretical tools have been developed. Waveguide designs can be quickly analyzed, and waveguide device patterns can be automatically laid out and fractured onto an e-beam grid.

The integrated optical devices currently under design and construction include the familiar channel-dropping filter, a matched filter for NRZ-encoded optical data, a co-directional wave-guide coupler with a flat wavelength response, and novel optical circuits. One set of these circuits implement a reconfigurable add/drop switch with a Mach-Zehnder (MZ) interferometer and two channel-dropping filters and the other implements a spectrally-isolated multiple-pole filter. We work with the InGaAsP/InP material system, in collaboration with Professor Leslie A. Kolodziejski and her group, and the Ge-doped SiO_2 system, which can be purchased from PIRI. We are tailoring our filters and couplers for the all-optical network group and space-based communications group at MIT Lincoln Laboratories, the fiber gyro group at RLE (Professor Haus), and the medical imaging group at RLE (Professor Fujimoto).

To lay out the waveguides that are designed for fabrication, a significant amount of code was written within the group. We needed to unambiguously specify with the least amount of input the shape of the waveguides, so that the computer could calculate the remaining dimensional parameters and then fracture the mathematical line onto a grid suitable for e-beam writing. Figure 7 shows the required specification of a waveguide pair and a closeup of the fractured waveguide.

Work this year will focus on the development of the InP and glass material systems to suit the various optical designs and implement most of the current filter and coupler designs.
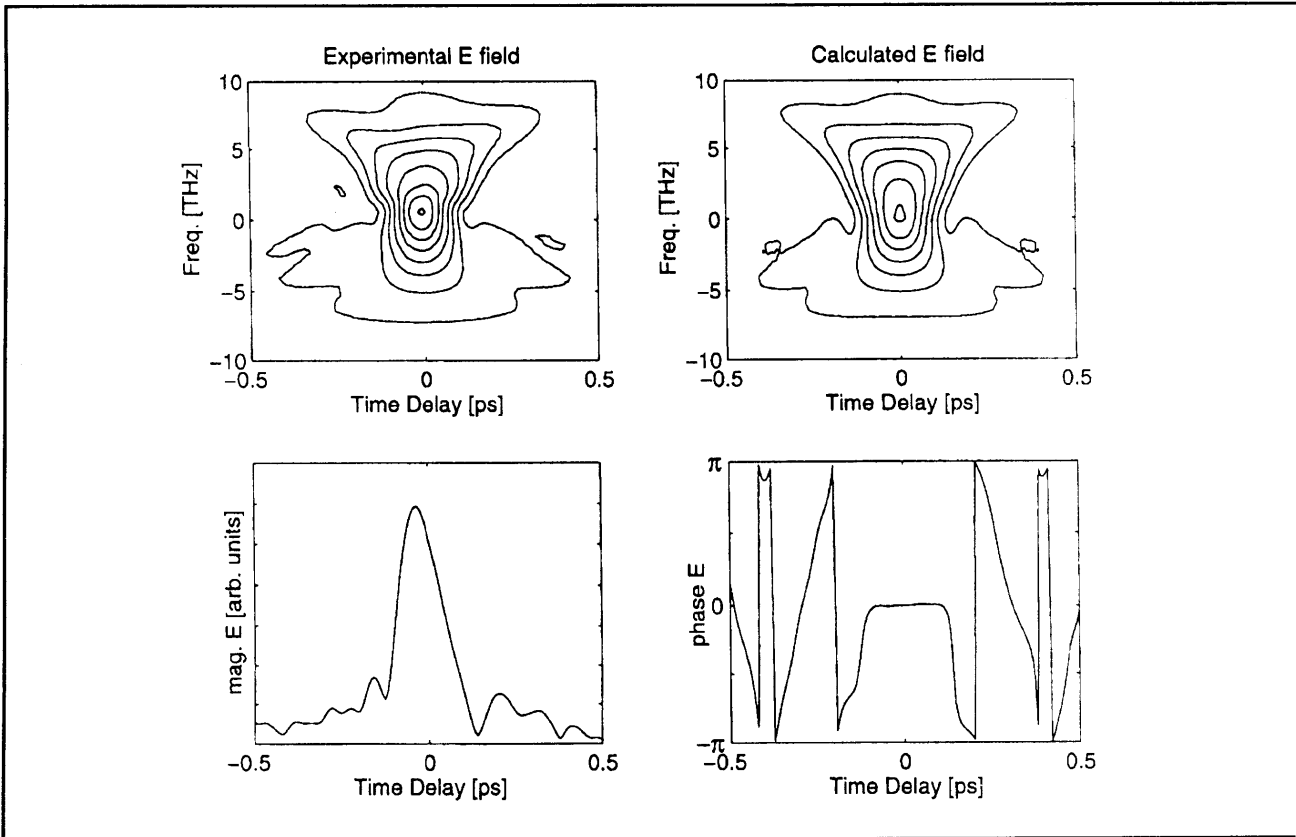
Figure 7. Fracture of waveguide curve to E-beam grid.

1.7 High-Power and Frequency-Doubled Stretched-Pulse Fiber Laser

Sponsors

Project Staff

Professor Erich P. Ippen, Lynn E. Nelson, Siegfried B. Fleischer, Gadi Lenz, David J. Dougherty

Our group's recent work on stretched-pulse additive-pulse mode-locked (SP-APM) fiber lasers has led to a generation of ultrashort pulses (100 fsec) with energies comparable to those of color-center lasers.[27] By using the APM rejection port as the output port, pulse energies of over 2 nJ have been achieved with average powers of > 90 mW. One application for these high power pulses is as a seed for a Ti:Sapphire regenerative amplifier. The output pulses from the fiber laser at 1.55 μm are compressed and passed through a nonlinear crystal to generate pulses at 775 nm which can then seed the amplifier. This frequency-doubled SP-APM fiber laser is an inexpensive, compact seeding source for regenerative amplifiers and could replace the argon-pumped Ti:Sapphire laser.

Our goal has been to optimize the efficiency of the second harmonic generation and the quality of the frequency-doubled pulse width, rather than the fundamental pulse width and quality. By operating the SP-APM laser with a large net positive dispersion and backwards pumping a long piece of erbium-doped fiber, we obtained average output powers of > 95 mW at 35.2 MHz. The highly stretched 1 psec pulses have a 70 nm bandwidth and are compressed with silicon Brewster prisms to 100 fsec pulses with 85 mW of average power.

By focusing the compressed fundamental pulses into a 1 cm-long (uncoated) BaB_2O_4 (BBO) crystal, frequency-doubled powers as high as 7.5 mW can be achieved. These correspond to an 8.5 percent

---

[27] K. Tamura, C.R. Doerr, L.E. Nelson, H.A. Haus, and E.P. Ippen, "Technique for Obtaining High-energy Ultrashort Pulses from an Additive Pulse Mode-locked Erbium-doped Fiber Ring Laser," *Opt. Lett.* 19: 46 (1994).

Figure 8. FROG data on the fundamental pulse: experimental data (top left), calculated fit (top right), derived pulse amplitude (bottom left), and derived pulse phase profile (bottom right).

conversion efficiency and pulse energies of up to 210 pJ. The frequency-doubled pulse width is 73 fsec and the spectrum is 8.5 nm wide centered at 774 nm, resulting in a time-bandwidth product of 0.31, which is near transform-limited assuming secant hyperbolic pulse shapes. Pulse energies on this order are required to seed high-repetition-rate regenerative amplifiers to avoid amplified spontaneous emission background.[28]

In order to better characterize both the fundamental and frequency-doubled pulses, we used frequency-resolved optical gating (FROG), which allows the direct determination of the intensity and phase of an ultrashort pulse.[29] FROG data on the fundamental pulse was taken by measuring the spectrum of the second harmonic generation (SHG) as the pulse delay was changed in a background-free autocorrelation configuration. An iterative Fourier transform

algorithm was then used to derive the pulse amplitude and phase profiles, which are shown in figure 8 along with the SHG FROG trace from the calculated field. The phase is flat across the central portion of the pulse and indicates that the linear chirp has been compensated by the prisms in this region, whereas in the pulse wings, the phase varies rapidly, indicating nonlinear chirp. The high-pulse quality of the frequency-doubled output was confirmed by performing an SHG FROG measurement on this pulse using another background-free autocorrelation setup. The FROG trace was round and smooth, indicating that the phase was flat across the entire pulse. Efficient frequency-doubling at the peak of the fundamental pulse thus selects that part of the pulse which is unchirped, resulting in a visible red beam of transform-limited pulses which may be used for aligning and seeding a Ti:sapphire regenerative amplifier.

28 T.B. Norris, "Femtosecond Pulse Amplification at 250 kHz with a Ti:Sapphire Regenerative Amplifier and Application to Continuum Generation," *Opt. Lett.* 17: 1009 (1992).

29 D.J. Kane and R. Trebino, "Characterization of Arbitrary Femtosecond Pulses Using Frequency-resolved Optical Gating," *IEEE J. Quantum. Electron.* 29: 571 (1993); J. Paye, M. Ramaswamy, J. Fujimoto, and E.P. Ippen, "Measurement of the Amplitude and Phase of Ultrashort Light pulses from Spectrally Resolved Autocorrelation," *Opt. Lett.* 18: 1946 (1993).

1.8 Femtosecond Pulse Amplification and Continuum Generation at 1.55 μm

Sponsors

Project Staff

Professor Erich P. Ippen, Gadi Lenz, David J. Dougherty, Dr. Günter Steinmeyer, Werner Gellermann[30]

High-power femtosecond pulses are needed for a variety of time-resolved spectroscopy applications. They provide intense excitation and make it possible to generate new wavelengths. Particularly useful for the latter process is a phenomenon known as continuum generation, in which a focused pulse produces a broadband femtosecond flash with synchronized spectral components over a wide wavelength range. Most previous sources providing this capablity, notably amplified dye and Ti:sapphire systems, have been centered at near-visible and visible wavelengths. We have been working on a system for use in the longer wavelength 1.5 μm band of importance to optical communications. One such source was demonstrated previously: an additive-pulse-modelocked (APM) NaCl:OH⁻ color-center laser followed by a six pass NaCl:OH⁻ amplifier.[31] This has not been pursued further because of difficulties with oscillator stability, the need for continuous multilaser illumination of the color-center crystals, and poor gain and beam quality in the amplifier. Instead, we have developed a different source using a very stable, diode-pumped femtosecond fiber laser oscillator and a high-gain KCl:Tl⁺ amplifier. With a kilohertz-rep-rate Q-switched Nd:YAG pump for the amplifier pump, only two passes are needed to amplify the fiber laser pulses to 10 μJ/pulse. The output beam quality is excel-

lent, and a broadband continuum can be generated in a variety of materials.[32]

The experimental arrangement is shown in figure 9. The diode-pumped stretched-pulse APM erbium-doped fiber laser[33] puts out highly chirped, 1.5-ps pulses with energies of about 2 nJ, at a rep-rate of 40 MHz. Single pulses are selected from this beam, by a $LiTaO_3$ modulator, at a 1 KHz rep-rate to match that of the Q-switched Nd:YAG laser. Relative timing between the selected pulse and peak amplifier gain can be adjusted with a countdown circuit. Single pass gain through the 2-cm-long KCl amplifier is about 1000 for Nd:YAG pumping of 1.5 mJ/pulse. After only two passes, the pulses have been amplified by a total factor of more than 10^4, to energies on the order of 10 μJ. These pulses are then chirp compensated by a pair of silicon prisms to 200-fs durations and used to generate contiuum. The limitation on pulse duration is due to mismatch between the fiber laser spectrum and amplifier gain spectrum which narrows the output spectrum to 20 nm.

Broadband continuum generation was observed in several different materials. Figure 10 shows typical spectra, observed by focusing into commercially available, 3-mm-thick samples of SF56 glass and ZnSe. In addition to the plotted spectrum limited by the InGaAs photodiode array in our multichannel analyzer, components extending all the way to the visible were apparent. Techniques for performing differential time-resolved spectroscopy with the entire continuum, and for selecting wavelength tunable pulses over the 1.4 to 1.7 μm range, are now being pursued.

1.8.1 Publication

Lenz, G., W. Gellerman, D.J. Dougherty, K. Tamura, and E.P. Ippen. "Femtosecond Fiber Laser Pulses Amplified by a KCl:Tl⁺ Color-center Amplifier for Continuum Generation in the 1.5-μm Region." *Opt. Lett.* 21: 137 (1996).

---

[30] Department of Physics, University of Utah, Salt Lake City, Utah.

[31] G. Sucha, S.R. Bolton, and D.S. Chemla, "Generation of High-Power Femtosecond Pulses Near 1.5 μm Using a Color-Center Laser System," *IEEE J. Quantum Electron.* 28: 2163 (1992).

[32] G. Lenz, W. Gellerman, D.J. Dougherty, K. Tamura, and E.P. Ippen, "Femtosecond Fiber Laser Pulses Amplified by a KCl:Tl⁺ Color-center Amplifier for Continuum Generation in the 1.5-μm Region," *Opt. Lett.* 21: 137 (1996).

[33] K. Tamura, E.P. Ippen, H.A. Haus and L.E. Nelson, "77-fs Pulse Generation From a Stretched-Pulse Mode-Locked All-Fiber Ring Laser," *Opt. Lett.* 18: 1080-1082 (1993).
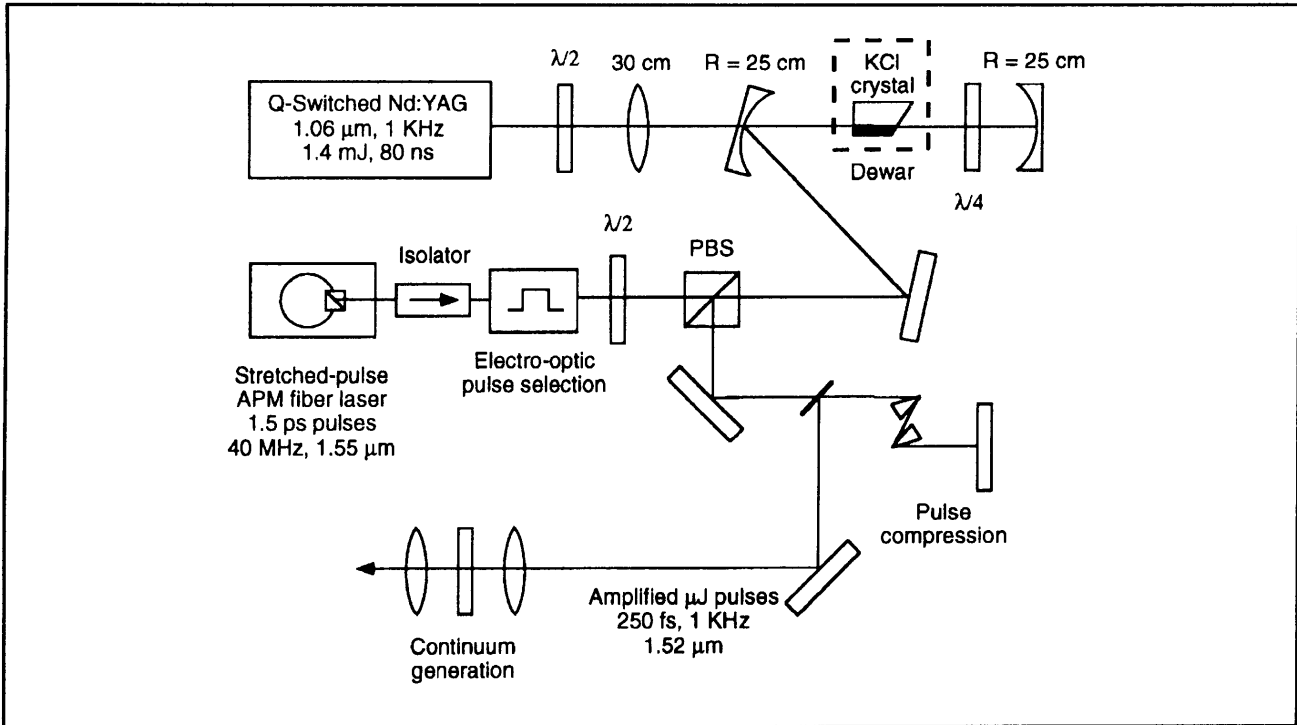
Figure 9. Experimental setup of the amplified fiber laser. λ/2s, half-wave plates; λ/4, quarter-wave plate; PBS, polarizing beam splitter.
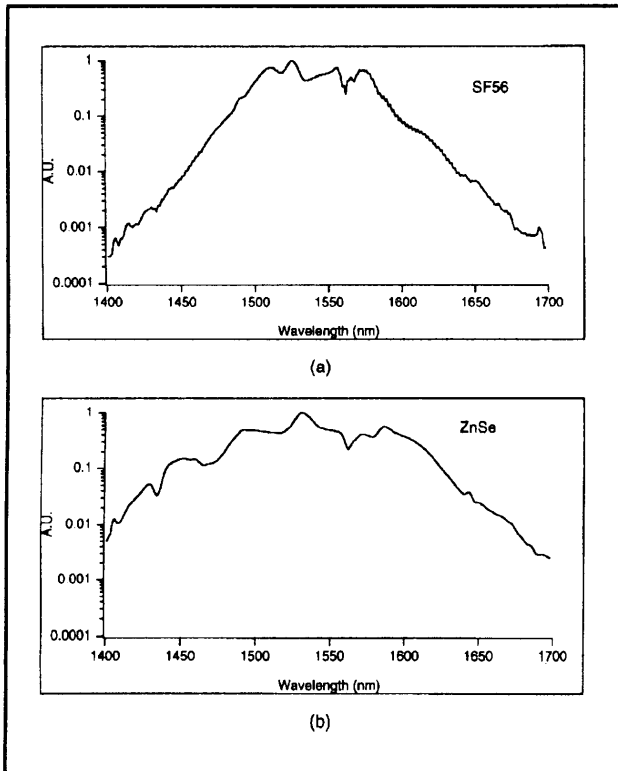

Figure 10. Continuum generated (a) in SF56 glass and (b) in ZnSe. The spectrum is displayed on a log axis normalized to the spectrum maximum and covers a spectral range of 1400-1700 nm.

1.9 Wavelength Shifting in Passive Semiconductor Waveguides

Sponsors

Project Staff

Professor Erich P. Ippen, Ali M. Darwish

Nondegenerate four-wave mixing (FWM) is a parametric process for frequency conversion in wavelength division multiplexing systems. We study FWM at λ = 1.5 μm in passive InGaAsP/InP waveguides since in passive waveguides the nonlinearity relies on virtual transitions and is therefore ultrafast. Our preliminary picosecond[34] and CW[35] experimental results are promising. In a 7.5-mm-long passive InGaAsP/InP single quantum well waveguide, a conversion efficiency of -11 dB was accomplished for a wavelength shift of 25 nm (3.3 THz) with picosecond pulses. Figure 11 shows a typical output spectrum for this case. A conversion efficiency of -20 dB, with a wavelength shift of 20 nm, was also achieved with CW light. To assess the suitability of InGaAsP/InP waveguides for communication systems, we measured the fundamental parameters of the waveguides. For example, we measured group velocity dispersion using FWM phase matching nulls, linear loss coefficient using Fabry-Perot techniques, and two photon absorption (TPA) coefficient using a power saturation technique.

Nonlinear loss mechanisms such as TPA can place fundamental limitations on the FWM conversion efficiency. We investigated the effect of nonlinear loss by solving a system of coupled first-order differential equations. The analysis indicates the presence of a geometry-independent maximum conversion efficiency equal to $e^{-2}|\chi^{(3)}/\text{Im}\{\chi^{(3)}\}|^2$. The analysis allows us to find the optimum device length and operating conditions and to understand some important issues in short pulse FWM. We are verifying the theoretical results with picosecond pulse FWM experiments.
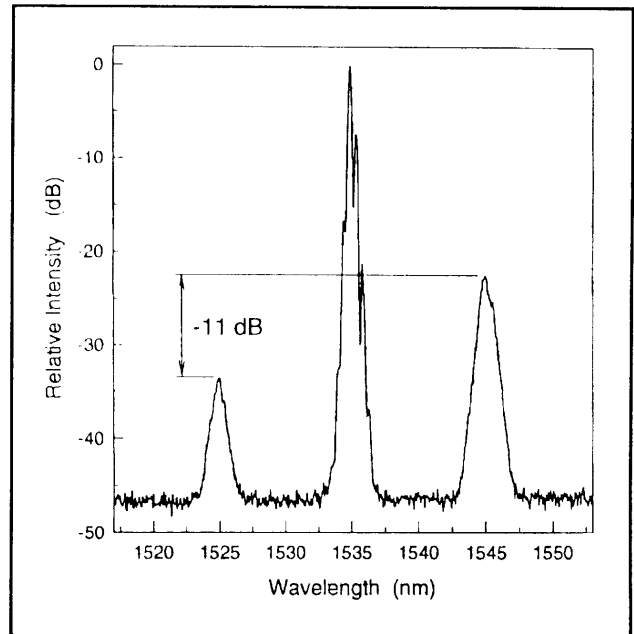

Figure 11. A conversion efficiency of -11 dB is achieved for a wavelength shift of 20 nm with high-peak power picosecond pulses.

Since the FWM process is phase sensitive, nonlinear index changes are expected to play an important role. Hence, we extended the FWM analysis to the case where nonlinear index changes dominate (e.g., a material with good nonlinear index switching figure of merit) and to the general case where both nonlinear index and loss mechanisms participate. The analysis indicates the presence of an improved geometry-independent maximum conversion efficiency that approaches unity as the nonlinear index changes dominate. In addition, the conversion efficiency has an oscillatory behavior with pump power since the nonlinear index changes drive the FWM process in- and out-of-phase. Compared to the case where nonlinear loss dominates, the optimum pump intensity and device length become significantly smaller when nonlinear index participate. While this is desirable for the CW case, it places serious restrictions on pump power for the short-pulse case. Finally, phase distortions due to nonlinear index changes lead to very complicated temporal pulse shaping at high pump powers.

This work is being carried out in collaboration with H. Le, J.P. Donnelly, S. Groves and E.A. Swanson at MIT Lincoln Laboratories. New multiple-

---

[34] A.M. Darwish, E.P. Ippen, H.Q. Le, J.P. Donnelly, S.H. Groves, and E.A. Swanson, "Short Pulse Wavelength Shifting by Four Wave Mixing in Passive InGaAsP/InP Waveguides," *Appl. Phys. Lett.*, forthcoming.

[35] J.P. Donnelly, H.Q. Le, E.A. Swanson, S.H. Groves, A. Darwish, and E.P. Ippen, "Nondegenerate Four-Wave Mixing Wavelength Conversion in Low-Loss Passive InGaAsP/InP Quantum-Well Waveguides," *Photonics Technol. Lett.*, forthcoming.

quantum-well structures are being designed with their collaboration for enhanced nonlinearity.

1.9.1 Publications

Darwish, A.M., E.P. Ippen, H.Q. Le, J.P. Donnelly, S.H. Groves, and E.A. Swanson. "Short Pulse Wavelength Shifting by Four Wave Mixing in Passive InGaAsP/InP Waveguides." *Appl. Phys. Lett.* Forthcoming.

Donnelly, J.P., H.Q. Le, E.A. Swanson, S.H. Groves, A. Darwish, and E.P. Ippen. "Nondegenerate Four-Wave Mixing Wavelength Conversion in Low-Loss Passive InGaAsP/InP Quantum-Well Waveguides." *Photonics Technol. Lett.* Forthcoming.

1.10 Visible and Near IR Femtosecond Pump-Probe Studies on C_{60} and Alkali-doped C_{60} Films

Sponsors

Joint Services Electronics Program
  Contract DAAH04-95-1-0038
U.S. Air Force - Office of Scientific Research
  Contract F49620-95-1-0221

Project Staff

Professor Erich P. Ippen, Siegfried B. Fleischer

Many novel photonic materials, such as C_{60}, are first available as thin films, since this is the easiest way to fabricate them. The nonlinear effects obtained from such sub-micron films are, however, many orders of magnitude smaller than for millimeter-size potential devices. It is thus important to detect very small signal modulations. In some cases, such as the present, high sensitivity is even more important because the samples are known to undergo long-lived photo-transformation under optical pumping.

At low chopping frequencies in pump-probe experiments, the signal-to-noise, and thus the lowest detectable signal, is in generally determined by intensity fluctuations of the femtosecond laser source. This requires the use of relatively high pump excitations for measurements of nonlinear properties. But at modest power levels (~ 1 mW), most laser sources with a sufficiently high

repetition-rate are shot-noise-limited at radio frequencies (RF). We implemented a RF modulation and heterodyne detection system for our pump-probe measurements that allows us to do shot-noise-limited-detection from 1 mW down to 2 μW detected power (at 800 nm). The modulation is done with an AOM at 10 MHz, and for the detection, we used a tuned detector to obtain a noise-equivalent power of about 1 pW $/\sqrt{Hz}$ at 10 MHz. The RF modulation also makes it possible to eliminate slow thermal background signals interfering with the picosecond or subpicosecond nonlinear response. Modulating both pump and probe eliminates scattered pump light and radiative RF pickup.

With this high sensitivity, we performed low-excitation-intensity pump-probe measurements on C_{60} thin films to study the ultrafast initial relaxation processes in the excited state. Pump excitation wavelengths throughout the visible spectrum and near UV and a variety of probe wavelengths in the visible and near IR were used. The signal, idler and pump beams of a Ti:Sapphire-pumped optical parametric oscillator (OPO) served as the femtosecond pulse source. Second harmonic generation and other mixing processes were used to generate quasi-continuously tunable light in the visible. An initial ultrafast response given by a step-response without any ultrafast decay on a picosecond or subpicosecond time-scale was observed. These results are in contrast to previously reported nonexponential decays obtained with higher fluence levels. We attribute those earlier results to laser induced changes in sample structure. Our experiments show further that the simple step response we observe at low powers changes to a more complicated, non-exponential response at higher pump fluence.[36] This effect is pronounced for shorter wavelength excitation. An average excitation fluence as low as 5 W/cm² at 460 nm was necessary to avoid it.

We also performed similar pump-probe studies on superconducting alkali-doped C_{60} films. Potassium- and rubidium-doped films were studied. The superconducting transition temperatures were measured for the samples used in this work and correspond to the 18 K and 33 K reported for K_3C_{60} and Rb_3C_{60}. Besides an instantaneous and a long-lived response, we observe two different decay processes with time-constants about 0.3 ps and 1 ps which we attribute to electronic scattering and vibrational relaxation. Our collaborators on this

---

36 S.B. Fleischer, B. Pevzner, D.J. Dougherty, M.S. Dresselhaus, and E.P. Ippen, "Visible and Near-IR Femtosecond Low-excitation Pump-Probe Studies on C_{60} and Alkali-doped C_{60} Films," MRS Fall Meeting, Boston, Massachusetts, November 1995.

topic are Boris Pevzner and Professor Mildred S. Dresselhaus. Investigations of the superconducting films are continuing.

1.10.1 Publication

Fleischer, S.B., B. Pevzner, D.J. Dougherty, M.S. Dresselhaus, and E.P. Ippen. "Visible and Near-IR Femtosecond Low-excitation Pump-Probe Studies on C_{60} and Alkali-doped C_{60} Films." MRS Fall Meeting, Boston, Massachusetts, November 1995.

1.11 Characterization of ZnSe/GaAs Heterojunctions

Project Staff

Professor Erich P. Ippen, David J. Dougherty, Professor Leslie A. Kolodziejski, Jody L. House

The investigation of the III-V/II-VI heterojunction formed between GaAs and ZnSe is important for several optoelectronic applications such as reliable blue laser diodes, and for linear and nonlinear optical communication devices.[37] By using a new technique which is a combination of photoreflectance (PR) and internal photo-emission (IPE) spectroscopies, we obtained an estimate of 200 meV for value of the conduction band offset. This is different from the commonly accepted value of 300 meV. We also have determined the magnitude and sign of the interface charge and trap densities for our sample.

The usual diagnostic tools for semiconductor characterization such as photoluminescence, Hall effect, and capacitance voltage measurements are either not specific to the interface, or cannot be used in this case because the films must be kept thin (< 0.15 μm) to avoid dislocations. Photoreflectance (PR) spectroscopy, a form of modulation spectroscopy which detects built-in electric fields, can be used to measure interface trap and charge densities and is thus well suited to characterizing

heterointerfaces. The bottom four traces in figure 12 (left) show PR spectra taken with different pump lasers for a 0.12 μm ZnSe film on an n-type GaAs buffer layer. The oscillation at 2.6 eV is the ZnSe bandgap signal, and the signals at 2.9 eV and 3.1 eV are due to the GaAs E1 and E1 + Δ1 signals. These E1 and E1 + Δ1 features were previously considered to be caused by spatially indirect cross over transitions and were used to deduce the currently accepted value of 300 meV for the ZnSe/GaAs conduction band offset.[38] Our data for a bare GaAs substrate, shown in the top trace, clearly demonstrate that the 2.9 eV signal originates from the GaAs alone and make the value of the conduction band offset an open question.

Analysis of the lineshapes of these signals as well as the signal from the GaAs bandedge (not shown) indicates the presence of a large (1.8 $\times$ 10^{12} cm^{-2}) surface charge density on the interface while the pump saturation intensities indicate a much smaller surface trap density of approximately 10^{10} to 10^{11} cm^{-2}. The bottom three traces in figure 12 (left) were taken with pump photon energies well below the ZnSe bandgap but still above the GaAs bandedge. The GaAs features are still present since electrons and holes are created in the GaAs, but a small signal at the ZnSe edge is also apparent. In a slab charge one-dimensional model of the electrostatics of the interface, carriers confined to the GaAs cannot screen fields in the ZnSe, so this signal must originate from electrons skipping over the barrier and into the ZnSe. This explanation accounts for the sign change as well as the drastically increased saturation intensity observed for this signal.

Tuning further towards the GaAs band edge eventually reduces the ZnSe signal as electrons do not have enough energy to enter the ZnSe. Figure 12 (right) shows the dependence on the ZnSe signal (hollow circles) amplitude as compared to the GaAs E1 signal (filled circles) as the pump wavelength is tuned from 840 nm to 688 nm corresponding to an energy range of 65 meV to 340 meV above the GaAs bandedge. The quadratic increase of the ZnSe signal above 160 meV is strikingly similar to internal emission photoconductivity results in other semiconductor heterojunctions.[39] In this experiment, tuning above the barrier results in a quadratic increase in current as described by Fowler-Nordheim emission theory. In our technique, the

---

[37] J.L. House, D.J. Dougherty, G.S. Petrich, L.A. Kolodziejski, and E.P. Ippen, *Appl. Surf. Sci.*, forthcoming.

[38] L. Kassel, H. Abad, J.W. Garland, M. Raccah, J.E. Potts, M.A. Haase, and H. Cheng, *Appl. Phys Lett.* 56: 42 (1990).

[39] H.K. Yow, P.A. Houston, and M. Hopkinson, *Appl. Phys. Lett.* 66: 2852 (1995).
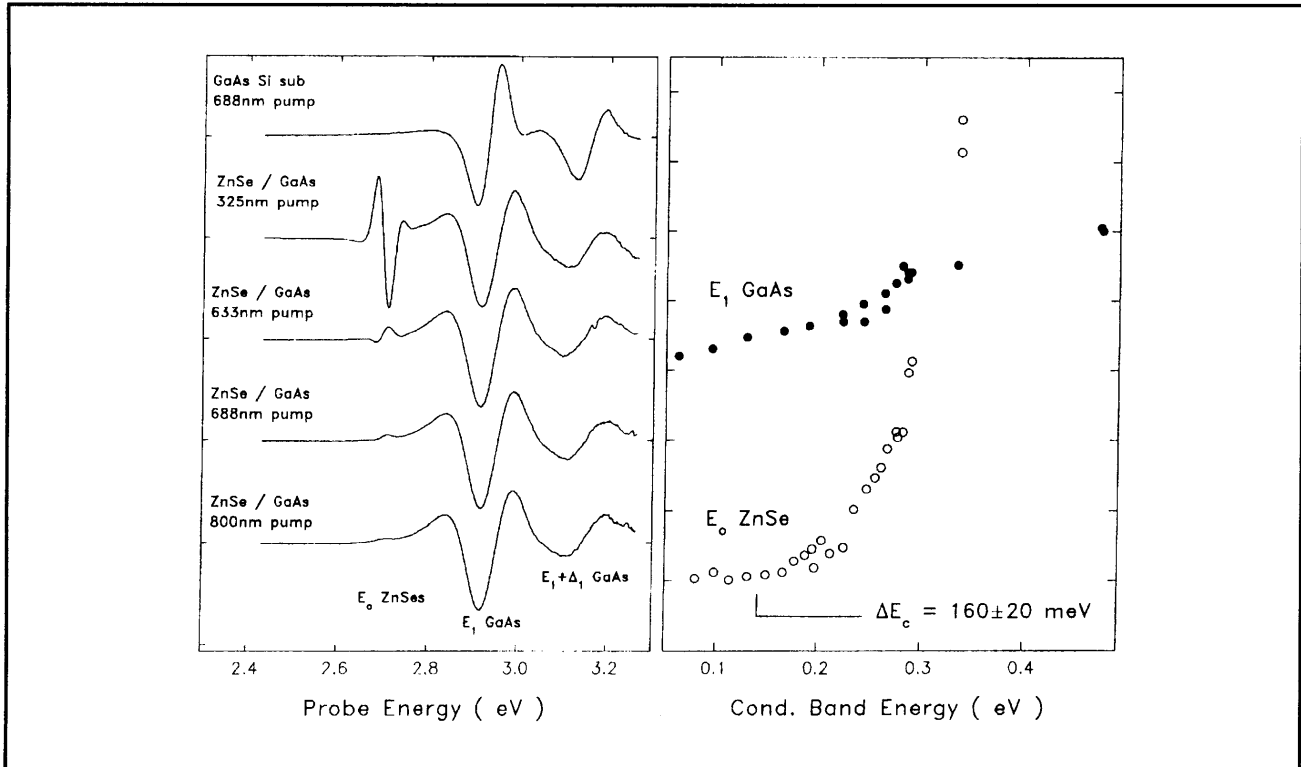
Figure 12. (left) PR spectra for a GaAs:Si substrate and a ZnSe/GaAs heterostructure taken with different pump sources. The features at 2.9 eV and 3.2 eV are due to transitions from the valence band to the L valley in GaAs. The signal at 2.67 eV is due to the ZnSe bandedge. (right) Signal amplitudes as a function of pump photon energy measured as electron conduction band energy in the GaAs. The threshold in the E_0 curve denotes the minimum electron energy necessary to escape into the ZnSe from the GaAs.

arrival of the electrons in the ZnSe is detected by the Franz-Kelydsh effect rather than as photocurrent, making it an equivalent noncontact technique. Note that the E1 GaAs signal, which remains relatively constant over this range, is, in fact, a measure of the absorption spectrum of the GaAs in a manner similar to photoluminescence excitation spectroscopy. The 160 meV threshold energy can be combined with a solution of Poisson's equation to arrive at a value for conduction band offset of 200 meV.

With this technique, we can measure surface charge and trap densities as well as the fundamental band alignment of semiconductor heterostructures. Relating these parameters to MBE growth and layer nucleation conditions should lead to improved understanding of semiconductor interfaces and interesting new materials such as ZnSe/GaAs quantum wells.

1.11.1 Publications

House, J.L., D.J. Dougherty, G.S. Petrich, L.A. Kolodziejski, and E.P. Ippen. *Appl. Surf. Sci.* Forthcoming.

Yow, H.K., P.A. Houston, and M. Hopkinson. *Appl. Phys. Lett.* 66: 2852 (1995).

1.12 Wavelength-Tunable Femtosecond Diagnostic Methods for Characterizing Photonic Bandgap Device Performance

Sponsors

Project Staff

Professor Erich P. Ippen, Constantine Tziligakis, Gadi Lenz, Siegfried B. Fleischer, Dr. Günter Steinmeyer

A major area of potential applications for photonic bandgap materials is in the development of new devices with improved characteristics in the optical regime. Submicron structures are being fabricated for the near-infrared wavelengths by Professor Kolodziejski's group, and we are developing wavelength-tunable-femtosecond (WTF) techniques to investigate the actual device characteristics.

For that purpose, we are building a WTF experimental setup for characterizing one dimensional air-bridge photonic bandgap devices in the 3-5 micron range. These devices, currently being fabricated, consist of a dielectric waveguide periodically punctuated with holes and suspended in air, thus forming an air-bridge structure which exhibits an optical bandgap in the 3-5 micron wavelength range. The introduction of an appropriate defect region (absence of a hole) in the middle of the periodic structure creates a microcavity characterized by a high Q resonance placed inside the bandgap. In the fabrication of the structures, GaAs is used for the waveguide and $Al_xGa_{1-x}As$ for the underlying substrate. The experimental setup we are using to test these structures takes advantage of the unique features of femtosecond Ti:sapphire lasers and optical parametric oscillators (OPOs). By synchronously pumping an OPO with a Ti:sapphire laser, two well-synchronized femtosecond pulse trains are obtained with tens of milliwatts average power tunable in the 1-2 micron wavelength range. Femtosecond pulses at longer wavelengths are then obtained by difference frequency generation in a $LiIO_3$ nonlinear crystal. Wavelength conversion of femtosecond pulses to the 3-5 micron regime is possible with an average powers of hundreds of microwatts available for coupling into the photonic bandgap structures. Reflecting microscope objectives couple the infrared pulses into the waveguides and provide imaging of the output. With the output light coupled into a spectrometer, we take advantage of the very wide spectrum of the femtosecond pulses to obtain essentially single-shot measurement of the device bandgap and filtering character-

istics. In preliminary work these diagnostics are being applied to test waveguide structures.[40]

1.12.1 Publication

Tziligakis, C., K.Y. Lim, J.C. Chen, G.S. Petrich, L.A. Kolodziejski, E.P. Ippen, S. Fan, P.R. Villenuve, and J.D. Joannopolous. "Wavelength-Tunable Femtosecond Diagnostic Methods for Characterizing Photonic Bandgap Device Performance." *NATO Advanced Studies Institute of Photonic Bandgap Materials,* Elounda, Greece, June 18-30, 1995.

1.13 Ultrashort Pulse Generation in Solid-State Lasers

Sponsors

Joint Services Electronics Program
   Grant DAAH-04-95-1-0038
U.S. Air Force - Office of Scientific Research
   Contract F49620-95-1-0221
U.S. Navy - Office of Naval Research (MFEL)
   Contract N00014-94-1-0717

Project Staff

Dr. Brett E. Bouma, Igor P. Bilinsky, Boris Golubovic, Dr. Viktor P. Mikhailov, Professor James G. Fujimoto

1.13.1 Compact Ultrashort Pulse Sources

Advances in signal processing, high-speed communications, and the investigation of ultrafast nonlinear processes in semiconductor devices and materials may be facilitated through the development of compact ultrashort pulse laser sources. Generally, these sources must be technologically simple, robust, and cost effective. While solid state gain media are well suited to meet these criteria, their relatively low-gain cross-sections have required the use of fast saturable absorption for modelocking. During the last few years, significant advances have been made in the development of fast saturable absorbers utilizing the electronic Kerr effect. Kerr

---

[40] C. Tziligakis, K.Y. Lim, J.C. Chen, G.S. Petrich, L.A. Kolodziejski, E.P. Ippen, S. Fan, P.R. Villenuve, and J.D. Joannopolous, "Wavelength-Tunable Femtosecond Diagnostic Methods for Characterizing Photonic Bandgap Device Performance," *NATO Advanced Studies Institute of Photonic Bandgap Materials,* Elounda, Greece, June 18-30, 1995.

lens modelocking (KLM),[41] in fact, has allowed the generation of the shortest pulses ever produced directly from a laser oscillator.[42] A theoretical understanding of Kerr effect modelocking has been developed by Professors Eric P. Ippen and Hermann A. Haus in conjunction with our group.[43]

In the past year, we have applied our theoretical model of KLM to facilitate optimization of modelocking performance and allow the extension of this simple pulse-forming mechanism to novel resonator geometries. Two Ti:Al$_2$O$_3$ KLM lasers in our laboratory, currently producing pulses of ~ 10 fs duration, are the direct result of the accuracy of our modeling.

KLM lasers utilize self-focusing in the presence of soliton-like pulse shaping arising from self-phase modulation and net negative intracavity group-velocity dispersion (GVD) to generate chirp-free ultrashort pulses. Negative GVD is most commonly achieved in KLM lasers by use of an intracavity prism pair; however, this places constraints on laser geometry and size. To date, KLM lasers have almost exclusively used a folded X- or Z-cavity geometry with the prism pair in one arm of the laser. Repetition rates have not exceeded the 100 MHz range.

In the past year, we have advanced our theoretical understanding of KLM to include novel compact laser geometries. We have demonstrated that alternative Kerr-lens mode-locked resonator designs can simultaneously reduce overall laser size and complexity while actually enhancing functionality.[44] These new resonator designs enable the self-starting generation of 100 fs pulses at repetition rates of 1 GHz. These lasers have important implications for compact, all-solid-state, femtosecond laser technology, especially because it can readily be extended to the modelocking of diode-pumped lasers.

1.13.2 Flashlamp Pumped Ti:Al$_2$O$_3$ Laser Modelocking

Simple and affordable high-power, short-pulse laser sources are important for numerous applications such as optical frequency conversion including harmonic generation and parametric generation, studies of nonlinear optical properties of materials, materials processing, and laser surgery. To date, the most common approach to obtaining short pulses in the microjoule to millijoule range from modelocked Ti:Al$_2$O$_3$ lasers is by using multipass or regenerative amplifier systems. Such systems achieve excellent performance, however they are relatively complex and costly. A simple, alternative method for the generation of high-power, picosecond pulses directly from a single laser oscillator is the use of flashlamp pumped, modelocked systems.[45]

In collaboration with Dr. Victor Mikhailov at the International Laser Center in Minsk, Belarus, we have extended our previous work by investigating the applications of new materials capable of providing passive saturable absorber action in the near infrared. We have explored the spectroscopy and absorption dynamics of materials such as CuIn$_{2-x}$Se$_x$ nanoparticles in glass, CuS and Fe ion films, and V^{3+}:YAG. The relative simplicity of these materials allows the inexpensive fabrication of laser quality samples. Our preliminary studies have indicated that these materials may be appropriate for the passive modelocking of flashlamp pumped Ti:Al$_2$O$_3$.

1.13.3 Broad Spectrum Solid-State Laser Development

Numerous studies, including the investigation of ultrafast carrier relaxation processes in semiconductors and semiconductor devices and biomedical imaging, require the availability of broad spectral coverage in the infrared and near infrared wave-

[41] D.K. Negus, L. Spinelli, N. Goldblatt, and G. Feuget, "Sub-100 fs Pulse Generation by Kerr Lens Modelocking in Ti:Al$_2$O$_3$," Postdeadline paper presented at the Topical Meeting on Advanced Solid State Lasers, Optical Society of America, Washington, DC, May 1991.

[42] J. Zhou, G. Taft, C-P. Huang, M.M. Murnane, H.C. Kapteyn, and I.P. Christov, "Pulse Evolution in a Broad-Band Ti:Sapphire Laser," *Opt. Lett.* 19: 1149 (1994).

[43] H.A. Haus, J.G. Fujimoto, and E.P. Ippen, "Structures for Additive Pulse Modelocking," *J. Opt. Soc. Am. B* 8: 2068 (1991); H.A. Haus, J.G. Fujimoto, and E.P. Ippen, "Analytic Theory of Additive Pulse and Kerr Lens Mode Locking," *IEEE J. Quant. Electron.* 28: 2086 (1992).

[44] B.E. Bouma and J.G. Fujimoto, "Compact Kerr-lens Mode-locking Resonators," *Opt. Lett.* 21: 256 (1996).

[45] B.E. Bouma, A. Gouveia-Neto, J. A. Izatt, J. Russel, R. Sierra, U. Keller, and J. G. Fujimoto, "Hybrid Mode Locking of a Flash-Lamp-Pumped Ti:Al$_2$O$_3$ Laser," *Opt. Lett.* 19: 1858 (1994).

length range. Several broad bandwidth, tunable solid state sources have been developed, most notably Ti:Al$_2$O$_3$ (titanium sapphire), Cr:Mg$_2$SiO$_4$ (Cr:Forsterite), and Cr:YAG. The combination of these three sources alone can, in principle, cover the entire range from .65 μm to 1.65 μm. However, of these sources only titanium sapphire has been demonstrated to tune throughout its fluorescent emission range. This fact is largely due to the presence of excited state absorption, parasitic absorption, and poor figure of merit in the Chromium doped crystals.

During the past year, we have explored two approaches to enhancing the wavelength coverage of the three laser crystals listed above. The first approach involves the development of novel pumping strategies which allow the use of shorter laser crystals and thereby reduce the deleterious effects of excited state and parasitic absorption. The second approach has explored new crystal growth procedures which may allow the development of more strongly doped and higher figure of merit crystals.

Fluorescent emission from Cr:Forsterite suggests the possibility of producing modelocked laser pulses in the wavelength range of 1.05 μm to 1.35 μm. However, an overlap with the absorption band on the short wavelength end of the spectrum and the presence of water absorption lines near 1.35 μm have limited the tuning range for modelocked operation. The convenience of pumping with the standard 1.06 μm Nd:YAG lasers, where the absorption of Cr:Forsterite is relatively weak, dictates the use of long laser crystals which preclude tuning below 1.18 μm. We have constructed a Nd:YAG pumped KLM Cr:Forsterite laser and have demonstrated tuning over the range 1.18 μm to 1.32 μm. This laser produces modelocked pulse durations of 30 fs and is currently being used for short coherence length biomedical imaging.

In collaboration with the International Laser Center, in Minsk, Belarus, we have investigated new crystal growth procedures which may allow the development of more strongly doped Cr:Forsterite crystals. Higher doping will allow the use of shorter laser crystals than previously used and should result in both greater tuning range and the production of shorter modelocked pulse durations. During the

past year, we have investigated the spectroscopy and laser action of Cr:Forsterite crystals grown along the crystallographic c-axis, comparing their performance to the standard crystal growth which progresses along the a-axis. Our preliminary investigation focused on crystals from the two growth procedures having equivalent concentrations of chromium ions and indicated that this new crystal growth process can produce laser gain media with performance comparable to that of the standard crystals. Future work will explore the spectroscopy and laser performance of highly doped c-axis grown Cr:Forsterite crystals.

1.13.4 Publication

Bouma, B.E., and J.G. Fujimoto. "Compact Kerr-lens Mode-locking Resonators." *Opt. Lett.* 21: 256 (1996).

1.14 Ultrafast Phenomena in Materials and Devices

Sponsors

Project Staff

Igor P. Bilinsky, Boris Golubovic, Dr. Brett E. Bouma, Professor James G. Fujimoto, Dr. Christopher Stanton,[46] Dr. Norman Tolk[47]

1.14.1 Carrier Dynamics in InGaAs Strained Layer Diodes

Nonlinear gain and transient carrier dynamics in diode lasers play important roles in laser line width, modulation bandwidth, amplification, and short pulse generation. Previous studies by our group[48] have used a new heterodyne multiple wavelength pump-probe technique to investigate nonlinear gain dynamics in InGaAs/AlGaAs graded-index single-

---

[46] University of Florida, Gainsville, Florida.

[47] Vanderbilt University, Nashville, Tennessee.

[48] C.-K. Sun, B. Golubovic, J.G. Fujimoto, H.K. Choi, and C.A. Wang, "Heterodyne Nondegenerate Pump-Probe Measurement Technique for Guided Wave Devices," *Opt. Lett.* 20: 210-212 (1995).

quantum-well diode lasers. To our knowledge, preceding this work, no multiple wavelength gain and transient carrier dynamics measurements were reported. We were able to map the femtosecond gain dynamics at a range of wavelengths for a fixed excitation pulse. The transient measurements showed a pump-induced transmission decrease in both the gain and loss regions. Around zero time delay, a sharp transmission decrease was observed with a spectral peak around the pump wavelength and a time-resolution limited recovery. This transient may be attributed to a combination of two-photon absorption, spectral hole burning, and coherent artifacts. Shortly after the pump pulse, a thermalized carrier distribution with higher temperature and lower concentration is established. Gain depletion throughout the investigated spectral region was observed. For time delays longer than 1 ps, the gain partially recovers as the temperature reaches equilibrium with the lattice. The residual gain changes are produced by the decrease in the carrier population and recover on a much longer time scale.

In collaboration with theoretical physicists at the University of Florida, Gainsville, detailed theoretical models for the gain dynamics for InGaAs strained layer diodes were developed. Calculations of the femtosecond gain dynamics in InGaAs/AlGaAs strained layer single-quantum-well diode lasers were compared to experiments which used a multiple-wavelength pump probe technique.[49] In the model developed, transient gain and differential transmission are computed in a multiband effective mass model including biaxial strain, valence subband mixing, and scattering both within and between subbands. The transient photogeneration of electron-hole pairs by the pump pulse and subsequent relaxation of carriers by both polar optical phonon scattering and carrier-carrier scattering are calculated within a Boltzmann equation framework. A relaxation approximation for the carrier-carrier scattering is made and the coupled Boltzmann equation is solved using an adaptive Runge-Kutta technique.[50] This formalism aids the full understanding of the obtained experimental results and may aid future device design.

1.14.2 Multiwavelength Studies of The Nonlinear Index of Refraction in Narrow Bandgap Semiconductors

The nonlinear optical properties of semiconductor materials are of great interest because of their role as components of various optical semiconductor devices. The dominant nonlinear contribution to the index of refraction is the third order nonlinear response of the material. It is important for various applications including optical limiting, all optical switching and modulation as well as for frequency modulation behavior of diode lasers.

Theory predicts the scaling of nonlinear index with semiconductor bandgap, E_g, as E_g^4.[51] For this reason, narrow bandgap semiconductor materials, such as InAs, GaSb, etc., are of particular importance. To date, most previous investigations of nonlinear index effects have used fixed wavelength or narrowly tunable laser sources and inferred the scaling behavior and wavelength dependence by performing experiments in different materials systems. Tunability constraints have been especially severe for these experiments which require high-intensity, short laser pulses. Using the Vanderbilt Free Electron Laser (FEL) as a broadly tunable, high-intensity source, we have initiated the first systematic study of wavelength dependence of nonlinear index in narrow gap semiconductors.

There are several techniques for measuring the nonlinear index. One of the simplest and most sensitive is Z-scan.[51] It uses nonlinear propagation in order to measure the integrated nonlinear index. A high intensity laser beam is focused onto a material and the position of the material is scanned in the axial or Z direction. Scanning the Z position varies the focusing parameters of the beam in the nonlinear material and changes the propagation of the beam in the far field. Changes in the divergence of the beam are measured by measuring the transmission through an aperture positioned in the far field region behind the sample. From these transmission changes, the sign and magnitude of the nonlinear index can be calculated.

[49] G.D. Sanders, C.-K. Sun, B. Golubovic, J.G. Fujimoto, and C.J. Stanton, "Carrier-carrier Scatering in the Gain Dynamics of InGaAs/GaAs Diode Lasers,", submitted to *Phys. Rev. B.*; G.D. Sanders, C.J. Stanton, C.-K. Sun, B. Golubovic, and J.G. Fujimoto, "Theory of Carrier Gain Dynamics in InGaAs/GaAs Strained-layer Single-quantum-well Lasers," paper presented at the Eighth International Conference on Superlattices Micorstructures and Microdevices, Cincinnati, Ohio, August 20-25, 1995.

[50] G.D. Sanders, C.-K. Sun, B. Golubovic, J.G. Fujimoto, and C.J. Stanton, "Hot Carrier Effects in Femtosecond Gain Dynamics of InGaAs/AlGaAs Quantum Well Lasers," paper presented at the Ninth International HCIS Conference, Chicago, August 1995.

[51] M. Sheik-Bahae, A.A. Said, T.-H, Wei, D.J. Hagan, and E.W. Van Stryland, *J. Quant. Electron.* 26: 760 (1990).

In collaboration with Professor Norman Tolk's group at Vanderbilt University, we have used the Vanderbilt FEL to perform Z-scan experiments in InAs, GaSb and Ge. The Vanderbilt FEL is a high intensity laser source continuously tunable in the wavelength region from 2 to 10 microns which is relevant for narrow bandgap semiconductors. The Z-scan experiments were performed in the region from 4 to 6.5 microns which allowed us to observe both the bound and free carrier contributions to the nonlinear index as well as the two photon absorption coefficients as a function of wavelength. The measured values of the components of the nonlinear index are in fair agreement with ones obtained from theoretical predictions. By utilizing a pulse selection mechanism, it should be possible to eliminate thermal effects and further separate the bound and free carrier components of the nonlinear index. Thus the sensitivity and accuracy of the measurements will be increased.

1.14.3 Publications

Sanders, G.D., C.-K. Sun, B. Golubovic, J.G. Fujimoto, and C.J. Stanton. "Carrier-carrier Scatering in the Gain Dynamics of InGaAs/GaAs Diode Lasers." Submitted to *Phys. Rev. B.*

Sanders, G.D., C.J. Stanton, C.-K. Sun, B. Golubovic, and J.G. Fujimoto. "Theory of Carrier Gain Dynamics in InGaAs/GaAs Strained-layer Single-quantum-well Lasers." Paper presented at the Eighth International Conference on Superlattices Micorstructures and Microdevices, Cincinnati, Ohio, August 20-25, 1995.

Sanders, G.D., C.-K. Sun, B. Golubovic, J.G. Fujimoto, and C.J. Stanton. "Hot Carrier Effects in Femtosecond Gain Dynamics of InGaAs/AlGaAs Quantum Well Lasers." Paper presented at the Ninth International HCIS Conference, Chicago, Illinois, August, 1995.

Sun, C.-K., B. Golubovic, J.G. Fujimoto, H.K. Choi, and C.A. Wang. "Heterodyne Nondegenerate Pump-Probe Measurement Technique for Guided Wave Devices." *Opt. Lett.* 20: 210-212 (1995).

1.15 Laser Medicine

Sponsors

Project Staff

Stephen A. Boppart, Dr. Brett E. Bouma, Professor James G. Fujimoto, Dr. Mark E. Brezinski, Michael R. Hee, Guillermo J. Tearney, Professor James G. Fujimoto, Eric A. Swanson,[52] Dr. Cynthia A. Toth,[53] Dr. Reginald Birngruber,[54] Dr. Clarance P. Cain,[55] Gary D. Noojin,[55] Dr. W.P. Roach,[56] Dr. Cheryl D. DiCarlo[56]

1.15.1 Optical Coherence Tomography Technology

Optical biopsy, or micron scale, cross-sectional, optical imaging of tissue microstructure in situ, would aid the diagnosis and clinical management of many diseases. Optical coherence tomography (OCT) is a new optical imaging technique that uses low coherence interferometry to perform high-resolution, cross-sectional imaging in biological systems. OCT is analogous to ultrasound B mode imaging except that it uses an infrared light source and low coherence interferometry to perform micron resolution ranging and imaging. For an interferometric signal to be detected, the optical path lengths of the object and reference beam must be matched to within the coherence length of the source. Since multiply scattered photons from the object have traveled different optical path lengths than the reference beam, multiple scattering effects are minimized in the OCT image. Tissue reflectance is obtained axially by varying the reference arm delay and digitizing the magnitude of the inter-

---

[52] MIT Lincoln Laboratory, Lexington, Massachusetts.

[53] Duke University Eye Center, Durham, North Carolina.

[54] Medizinisches Laserzentrum, Lubeck, Germany.

[55] TASC, San Antonio, Texas.

[56] Armstrong Laboratory, Brooks Air Force Base, Texas.

ference. A cross-sectional image is produced by recording axial reflectance profiles while the beam on the tissue specimen is scanned.

OCT has been extensively applied in ophthalmology to provide tomographic images of the transparent structures in the eye.[57] Clinical studies have shown that OCT provides high resolution, cross-sectional images of the retina and can be used to diagnose a wide range of retinal macular diseases.[58] OCT imaging in other human tissues is made difficult due to optical scattering. However, recent *in vitro* studies have shown that OCT can image architectural morphology in highly optically scattering tissues.

An important application of OCT is imaging the vascular system to identify atherosclerotic lesions that are prone to rupture.[59] OCT has ten times greater resolution than state-of-the-art catheter-based ultrasonography, intravascular ultrasound (IVUS). Additional research has shown that OCT can perform high-resolution imaging of other organ systems such as the gastrointestinal and urinary tracts.[60]

Research in this laboratory, performed to advance optical coherence tomography technology, has yielded significant improvements in image resolution, acquisition speed, and the development of endoscopic imaging techniques. One of the key technological areas which greatly enhances the performance of OCT is the development of high power, ultrashort coherence length light sources. Recently, OCT imaging with axial resolutions of 2 to 4 μm have been demonstrated using broad bandwidth, short pulse femtosecond laser sources which have a short coherence length.[61]

Improvement in image acquisition times have also been recently demonstrated. The image acquisition times of OCT systems used in previous studies (60 seconds) is adequate for *in vitro* imaging but is insufficient for *in vivo* imaging because of motion artifacts. The development of higher power sources is critical to increasing image acquisition speed since the image acquisition rate directly trades off against detection sensitivity. To achieve image acquisition times below one second, alternatives to mechanical reference arm scanning technologies must also be developed. Recent work using these new technologies have achieved an acquisition rate of up to four images per second.[62]

Another technology which is necessary to apply OCT to imaging of internal organ systems is a catheter/endoscope which can deliver, focus, scan, and collect a single spatial mode optical beam. The catheter must be flexible and have a small diameter to facilitate its entry into internal channels such as coronary arteries, pancreatic or biliary ducts. A single mode fiber optic scanning OCT catheter/endoscope prototype has been developed during the past year.[63] This device is an enabling technology for developing a wide range of endoscopes and will permit OCT imaging of the *in vivo* gastrointestinal tissues.

This work is an ongoing collaboration with researchers at MIT, MIT Lincoln Laboratories, Massachusetts General Hospital's Cardiology Department, Pathology Department, and the Wellman Laboratories of Photomedicine. MIT Lincoln Laboratories has provided much of the OCT technology and equipment for use in ophthalmic and multiply scattering tissue studies. Massachusetts General Hos-

[57] G.D. Sanders, C.-K. Sun, B. Golubovic, J.G. Fujimoto, and C.J. Stanton, "Hot Carrier Effects in Femtosecond Gain Dynamics of InGaAs/AlGaAs Quantum Well Lasers," paper presented at the Ninth International HCIS Conference, Chicago, Illinois, August 1995.

[58] C.A. Puliafito, M.R. Hee, C.P. Lin, E. Reichel, J.S. Schuman, J.S. Duker, J.A. Izatt, E.A. Swanson, and J.G. Fujimoto, "Imaging of Macular Diseases with Optical Coherence Tomography," *Ophthalmol.* 102: 217-229 (1995).

[59] M.E. Brezinski, G.J. Tearney, B.E. Bouma, J.A. Izatt, M.R. Hee, E.A. Swanson, J.F. Southern, and J.G. Fujimoto, "Optical Coherence Tomography for Optical Biopsy: Properties and Demonstration of Vascular Pathology," *Circulation,* forthcoming.

[60] G.J. Tearney, M.E. Brezinski, M.R. Hee, B. Bouma, J.A. Izatt, E.A. Swanson, J.F. Southern, and J.G. Fujimoto, "Optical Biopsy in Human Tissue using Optical Coherence Tomography and Microscopy," paper presented at the Conference on Lasers and Electro-Optics, Optical Society of America, May 1995; G.J. Tearney, M.E. Brezinski, B.E. Bouma, J.F. Souther, and J.G. Fujimoto, "High Resolution Imaging of Gastrointestinal Tissue using Optical Coherence Tomography," Annual Meeting of the American Gastrointestinal Association, May 1996.

[61] B.E. Bouma, G.J. Tearney, S.A. Boppart, M.R. Hee, M.B. Brezinski, and J.G. Fujimoto, "High Resolution Optical Coherence Tomographic Imaging Using a Modelocked Ti:Al$_2$O$_3$ Laser Source," *Opt. Lett.* 20(13): 1486-1488 (1995).

[62] G.J. Tearney, B.E. Bouma, S.A. Boppart, B. Golubovic, E.A. Swanson, and J.G. Fujimoto, "High Speed Optical Coherence Tomography," paper to be presented at the Conference on Advances in Photon Migration, Orlando, Florida, March 1996.

[63] G.J. Tearney, S.A. Boppart, B.E. Bouma, M.E. Brezinski, N. Weissman, J.F. Southern, and J.G. Fujimoto, "Scanning Single Mode Fiber Optic Catheter/Endoscope for Optical Coherence Tomography," *Opt. Lett.,* forthcoming.

pital has been instrumental in providing the tissue samples and pathology and performing research aimed at evaluating the potential for OCT to obtain micron level "optical biopsies" of human tissue.

1.15.2 High-Resolution Optical Coherence Tomography

Chromium doped Forsterite is a new tunable solid-state laser material with a broad emission band near 1.2 μm. Cr:Forsterite has been modelocked using KLM, and pulse durations as short as 25 fs have been achieved. The peak output power from this laser is sufficient to generate significant spectral broadening within optical fiber. The zero dispersion point of standard single mode fiber overlaps with the spectral output of the Cr:Forsterite laser. This coincidence results in a strongly modulated spectral output inappropriate for biomedical imaging. We have avoided this problem by using dispersion shifted fiber and can obtain high resolution, high contrast coherence gating. The high average output power provided by this source enables high image acquisition speeds at high sen-

sitivities since speed, sensitivity, and optical source power directly trade off against each other.

Coherence ranging is performed with the self-phase modulated spectral source using a fiber optic Michelson interferometer. Wavelength flattened splitters were used to preserve the spectral extent of the source as it was routed to the scanning reference arm mirror, the biological sample, and back to the detectors. Dual balanced heterodyne detection enabled near shot-noise limited detection.

An image of human adipose tissue, shown in figure 13, demonstrates the high resolution imaging capability of this system. For this image, the transverse resolution, determined by the numerical aperture of the focusing objective, matches the measured longitudinal resolution of 5.7 microns.

Ultrahigh resolution OCT imaging using mode locked solid state lasers is a powerful technology for performing optical biopsy which can be applied for diagnosis, interoperative guidance, and clinical management in a wide range of medical applications.
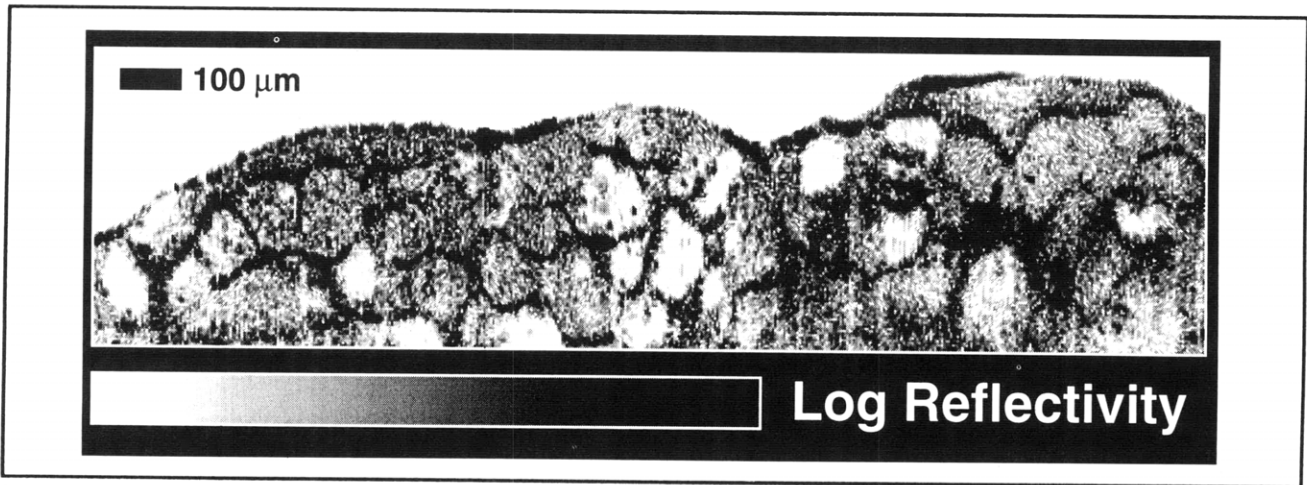

Figure 13. High-resolution OCT image of human adipose tissue.

1.15.3 High-Speed Optical Coherence Tomography

Currently, typical OCT systems used to image human tissue are implemented using superluminescent diodes (SLD) with center wavelengths of 850 or 1300 nm. These OCT systems have free space axial resolutions of 20-40 μm, a sample arm power of 50-150 μW, and signal-to-noise ratios (SNR) ranging from 90 to 110 dB. The image acquisition times of these systems (5 to 60 seconds) make difficult their application to *in vivo* imaging because of motion artifacts. To achieve image acquisition times below one second, alternative technologies to mirror translation scanning must

be developed. Because a high SNR is necessary for imaging to significant depths within turbid media, any increase of image acquisition rate must be accompanied by a commensurate increase in source optical power. We have constructed a novel OCT system which addresses both of these concerns and achieves an acquisition rate of four images per second. Each image consists of 292 x 250 pixels covering a sample area of 3 mm x 2.5 mm.

Previous OCT systems have utilized a mechanically translated reference arm mirror to enable axial scanning. The mirror velocity is typically in the range of 30 mm/s corresponding to a Doppler fre-

quency of 50 kHz. To enable image acquisition rates of two frames per second the Doppler frequency must be increased ~ 100 fold to 5 MHz. This would necessitate a reference mirror velocity of 3 m/s. Additionally, this velocity must be held constant over distances of 3-5 mm and repetition rates of ~ 0.5 kHz. Because no cost effective translator meeting these specifications is currently available, we have developed an alternative technology that uses piezo-electric transducers to induce stretch in an optical fiber. 40 m of single mode optical fiber is wrapped under constant tension about a piezo-electric modulator (PZM). As the PZM expands, the fiber is stretched inducing temporal delay on the light propagating within it. The long length of the fiber allows the small expansion of the PZM to be magnified to a length of approximately 3 mm. The deleterious effects of static and dynamic birefringence incurred in the fiber are compensated using Faraday rotators placed in the free space region of the interferometer arms. A triangle wave voltage tailored to minimize hysteresis

To maintain the high SNR necessary for deep imaging into turbid media such as human tissue, the decrease in image acquisition time must be matched by an increase in optical power. To enable high-speed, high-SNR imaging, we have employed the Cr:Forsterite laser source discussed above. At the high modulation frequency induced by the fast scanning piezo delay line, the noise due to amplitude fluctuation in the mode locked laser is low, but prevents Shot noise limited detection. Heterodyne dual balanced detection is used to reduce the laser noise below the Shot noise level and allows for OCT imaging with a SNR of 112 dB. This dynamic range is sufficient to allow OCT imaging to depths of greater than 2 mm within human tissue

1.15.4 Scanning Catheter/Endoscope for Optical Coherence Tomography

In order to apply OCT for imaging of internal organ systems, a flexible, small diameter, catheter/endoscope which is capable of delivering, focusing, scanning, and collecting a single spatial mode optical beam must be constructed. In the past year, we have developed a prototype single mode fiber optic scanning OCT catheter with a diameter

of 1 mm. The OCT catheter consists of a drive motor at its proximal end, a single mode fiber running the length of the catheter, and optical focusing and beam directing elements at the distal end. During image acquisition, the catheter is inserted into an internal tissue channel and the focused beam is scanned perpendicular to the axis of the catheter. An OCT image is acquired as the beam angle of rotation is varied over some range (usually 360 degrees). The speed of imaging depends on the speed of the rotation and the OCT unit acquisition speed. Preliminary images have been acquired using a superluminescent diode based OCT system.

To demonstrate imaging with the catheter, we have performed OCT of an *in vitro* human saphenous vein (figure 14A). The intact specimen was taken postmortem and imaged with the catheter in the center of the lumen of the vessel. The rectangular raw data image array was displayed in polar coordinates using a linear interpolation algorithm. The image was also processed to correct for the depth dependent exponential power loss caused by the optical attenuation of the tissue. A 30 MHz Intravascular Ultrasound image of the vein is displayed adjacent to the OCT image (figure 14B). As demonstrated by the figure, the OCT image shows a significant enhancement in resolution and capability to differentiate tissue morphology.

While many engineering issues still must be addressed in order to perform OCT imaging *in vivo*, the key enabling technologies required to achieve this objective have been developed and demonstrated by this laboratory. Improvement in image resolution, acquisition time, and the development of a fiber optic endoscope have been shown to be technically feasible. We believe that the results of this research will accelerate progress towards performing *in vivo* optical biopsies and should have a significant impact on medical diagnosis and the management of disease.

1.15.5 Ophthalmic Imaging and Diagnosis With Optical Coherence Tomography

In collaboration with MIT Lincoln Laboratory, we have developed a clinically effective, ophthalmic imaging OCT system.[64] A compact superluminescent diode (SLD) light source is utilized to provide approximately 500 μW of 840 nm light onto

---

[64] M.E. Hee, J.A. Izatt, E.A. Swanson, D. Huang, C.P. Lin, J.S. Schuman, C.A. Puliafito, and J.G. Fujimoto, "Optical Coherence Tomography of the Human Retina," *Arch. Ophthalmol.* 113: 325-332 (1995); M.R. Hee, J.A. Izatt, E.A. Swanson, D. Huang, J.S. Schuman, C.P. Lin, C.A. Puliafito, and J.G. Fujimoto, "Optical Coherence Tomography for Micron-resolution Ophthalmic Imaging," *IEEE Eng. Med. Bio.* 14: 67 (1995).
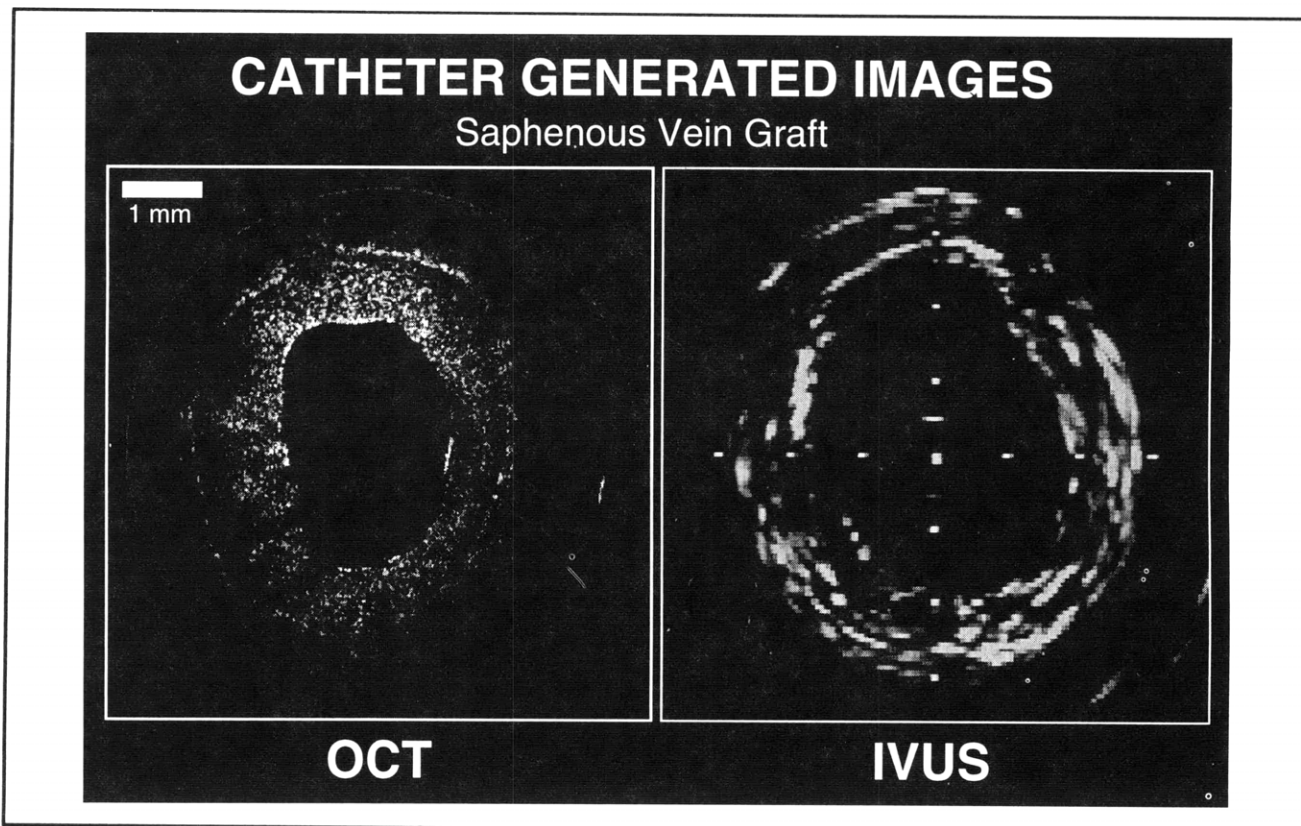
Figure 14. OCT and IVUS image of human saphenous vein graft.

the retina with a longitudinal resolution of 10 μm. The OCT system is integrated with a conventional ophthalmic slit-lamp biomicroscope using fiber-optics. Imaging of the retina occurs through a +78 diopter condensing lens mounted in front of the slit-lamp. A infrared sensitive video camera provides a view of the scanning probe beam on the fundus so that the location of each scan on the retina can be monitored. The operator is able to simultaneously view this video image and a false-color OCT tomogram on a computer monitor, which is updated in real time every 2.5 seconds. The system is fully computer controlled to allow fast positioning of a variety of scanning patterns at different locations on the retina. Imaging of different retinal regions occurs by translating either the patient's fixation point or the location of the scanning beam on the fundus, both under computer control. The fixation target provided in the ipsilateral eye allows the position of each OCT image relative to fixation to be automatically recorded, and permits follow-up scans to be accurately placed on the retina.

Image processing algorithms have been developed to minimize the effects of longitudinal patient eye motion during scanning and to automatically extract the thickness of various retinal layers directly from the OCT images. Longitudinal eye motion is accounted for by cross-correlating pairs of adjacent A-scans which form the tomogram to create an estimate of the retinal contour. The contour estimate is then digitally filtered to remove high frequency variations corresponding to patient motion. Quantitative measurements of retinal and retinal nerve fiber layer thickness are potentially useful in the diagnosis and monitoring of ocular diseases such as glaucoma and macular edema. These measurements may be performed using standard edge-detection image processing techniques.

Approximately 2000 patients with a variety of macular diseases and diseases of the optic nerve head have been examined at the New England Eye Center, Tufts University School of Medicine. In patients with macular pathology, OCT images have been correlated with the conventional clinical techniques of slit-lamp biomicroscopy and fluorescein

angiography.[65] We have found that the cross-sectional view of OCT is effective in the diagnosis and monitoring of macular holes, retinal detachment, macular edema, epiretinal membrane, and age-related macular degeneration. In patients with glaucoma, the ability of OCT to directly measure retinal nerve fiber layer thickness with micron scale resolution may lead to the first truly objective diagnostic for the presence or progression of this degenerative disease.

Macular hole is a frequently encountered retinal disease that is often difficult to diagnose accurately because there are a number of ophthalmoscopically similar appearing lesions. The disease progresses to involve a complete loss of the retina directly in the fovea leading to a devastating reduction in visual acuity. However, surgical intervention can often prevent or correct vision loss. OCT greatly facilitates the diagnosis and staging of macular holes, ensuring appropriate treatment. OCT is diagnostically useful in separating macular holes from other ophthalmoscopically similar appearing lesions and evaluating the stage of macular hole progression and the risk of hole formation in the second eye of patients who already have a unilateral macular hole. This information is useful in considering candidates for surgical treatment. Furthermore, OCT has been able to provide information on the pathogenesis of hole formation and the conditions which lead to the development of macular holes which may eventually lead to better treatment of this disease.[66]

OCT is superior to conventional slit-lamp biomicroscopy in evaluating retinal detachments, such as those occurring with central serous chorioretinopathy.[67] In a series of patients with this disease, OCT was effective in objectively quantifying the extent of neurosensory and pigment epithelial detachment many of which were undetected at the slit-lamp. Longitudinal OCT measurements were successful in monitoring the resolution of subretinal fluid. The ability of OCT to objectively and quantitatively monitor these detachments over time is useful in evaluating the necessity or effectiveness of treatment.

Diabetic retinopathy is the second leading cause of blindness in the United States. The development of macular edema is a major treatable cause of vision loss in patients with diabetic retinopathy. Macular edema is also common manifestation of a variety of other retinal diseases including epiretinal membranes, uveitis, and retinal vascular occlusions. Macular edema is traditionally evaluated by assessing (1) retinal thickening with slit-lamp biomicroscopy and (2) leakage of fluorescein dye from blood vessels into the retina, a relatively poor indicator of vision loss. OCT was used to measure retinal thickness in 72 eyes with the clinical diagnosis of nonproliferative or proliferative diabetic retinopathy, 34 eyes in diabetic patients who had no evidence of retinopathy, and 59 healthy control eyes. The mean±SD central foveal thickness measured by OCT was 146±22 μm in healthy eyes and 150±24 μm in diabetic eyes without evidence of retinopathy. In patients with diabetic retinopathy, OCT could objectively monitor the development and resolution of macular edema following treatment with 10 μm precision. In these patients, the central foveal thickness was 172±35 μm in the 49 eyes without macular edema as assessed by slit-lamp biomicroscopy, and 339±101 μm in the 23 eyes with macular edema. Central foveal thickness correlated with best corrected visual acuity in eyes with nonschemic retinopathy. These results show that OCT is a more sensitive indicator of retinal thickening due to macular edema than either slit-lamp biomicroscopy or fluorescein angiography, useful in objectively tracking the resolution of edema following laser therapy, and may be effective as a screening tool for the development of retinal edema in these patients.[68]

Current diagnostic techniques for epiretinal membranes in the macular region include slit-lamp biomicroscopy and fluorescein angiography. OCT images are useful in confirming the diagnosis of faint, diaphanous membranes, and in providing a cross-sectional assessment of factors contributing to vision loss, such as membrane opacity, retinal distortion or tractional detachment, and macular edema. The amount of foveal distortion,

65 M.R. Hee, J.A. Izatt, E.A. Swanson, D. Huang, J.S. Schuman, C.P. Lin, C.A. Puliafito, and J.G. Fujimoto, "Optical Coherence Tomography of the Human Retina," *Arch. Ophthalmol.* 113: 325-332 (1995).

66 C.A. Puliafito, M.R. Hee, C.P. Lin, E. Reichel, J.S. Schuman, J.S. Duker, J.A. Izatt, E.A. Swanson, and J.G. Fujimoto, "Imaging of Macular Diseases with Optical Coherence Tomography (OCT)," *Ophthalmol.* 102: 217-229 (1995).

67 M.R. Hee, C.A. Puliafito, C. Wong, J.S. Duker, E. Reichel, J.S. Schuman, E.A. Swanson, and J.G. Fujimoto, "Optical Coherence Tomography of Macular Holes," *Ophthalmol.* 102: 748-746 (1995).

68 M.R. Hee, C.A. Puliafito, C. Wong, J.S. Duker, E. Reichel, J.S. Schuman, E. A. Swanson, and J.G. Fujimoto, "Optical Coherence Tomography of Central Serous Chorioretinopathy," *Am. J. Ophthalmol.* 120: 65-74 (1995).

detachment, or edema provides an indication of the severity of the membrane. The thickness and reflectivity of the membrane on the OCT tomogram gives information on membrane opacity. Many studies have attempted to define prognostic indicators, such as membrane thickness or the presence of pre-operative cystoid macular edema, to predict eventual visual outcome after epiretinal membrane surgery. OCT provides a means to evaluate the cross-sectional characteristics of an epiretinal membrane, allowing a quantitative measurement of retinal thickness, membrane thickness, and the separation between the membrane and inner retina. These measurements may eventually prove useful for pre-operative characterization of surgical prognosis.

Age-related macular degeneration is the leading cause of blindness in the United States. Vision loss in this disease is often due to the formation of choroidal neovascularization (CNV). However, many eyes with CNV lack the fluorescein angiographic features required for treatment eligibility according to the Macular Photocoagulation Study guidelines and OCT may represent a new technique for visualizing such occult CNV. We have found that OCT is effective in the identification and quantification of subretinal and intraretinal fluid, and is particularly useful in evaluating possible foveal involvement of fluid accumulation or CNV. Measurements of retinal thickness with OCT provide an objective means of following edema and subretinal fluid in a patient through successive examinations. In patients with untreated exudative AMD, OCT was compared with fluorescein angiography in the classification of CNV. CNV could be morphologically divided into three categories on OCT: well-defined, poorly-defined, and fibrovascular pigment epithelial detachment (PED). CNV classified as well-defined or fibrovascular PED on OCT had well demarcated boundaries and might be potentially treatable. These membranes included most angiographically classic CNV and a subset of angiographically occult CNV which would not be traditionally eligible for treatment. OCT was also useful in monitoring CNV before and after laser photocoagulation. These studies suggest that OCT may have potential in defining the boundaries of a subset of occult CNV, leading to the possibility of more effective treatment delivery in these cases.

Glaucoma is the third leading cause blindness in the United States. The clinical evaluation of this pervasive disease is presently difficult. Current diagnostic techniques such as stereoscopic visualization of the optic nerve, nerve fiber layer photography, and evaluation of the cup-to-disc ratio are subjective with variation occurring even among experienced observers. Glaucoma is a disease of insidious onset, often leading to significant losses in peripheral vision that may not be immediately noticed by the patient. Quantitative visual field testing can provide early identification of these visual defects; however, up to 50 percent of the retinal nerve fiber layer may be lost before detection by standard clinical techniques. The ability of OCT to directly measure nerve fiber layer thickness may lead to an objective, early diagnostic for the onset of glaucoma, and a sensitive indicator of glaucomatous progression.

OCT provides a quantitative method of directly measuring the thickness of the retina and retinal nerve fiber layer (NFL) with high resolution as a potential early glaucoma diagnostic.[69] In a series of patients with and without glaucoma, NFL thickness as measured by OCT correlated well with the functional status of the optic nerve as measured by traditional visual field examination, and correlated better with visual field loss than either cupping or neuroretinal rim area. There was a highly significant difference in NFL thickness measured by OCT between normal and glaucomatous eyes. Longitudinal studies of measurement reliability indicate that retinal nerve fiber layer thickness measurements with OCT are reproducible to within 10 to 20 μm. These studies indicate that OCT is potentially able to detect the onset of glaucoma or glaucomatous progression before significant and irreversible damage to the retina occurs.

1.15.6 Cardiovascular Imaging Using Optical Coherence Tomography

Acute myocardial infarction (AMI), commonly referred to as "heart attack", is the leading cause of death in the industrialized world. AMI represents the abrupt loss of blood flow to a region of the heart resulting in tissue death. The cessation of blood flow results from the rupture of small to moderate sized cholesterol laden lesions in the arteries of the heart (coronary arteries), followed by clot formation and vessel occlusion. The current inability to identify these plaques prospectively is due to inadequacies of existing imaging techniques in defining plaque composition. Our hypothesis is that OCT, a new method of fiber optic based micron scale

[69] M.R. Hee, C.A. Puliafito, C. Wong, J.S. Duker, E. Reichel, B.K. Rutledge, J.S. Schuman, E.A. Swanson, and J.G. Fujimoto, "Quantititative Assessment of Macular Edema with Optical Coherence Tomography," *Arch. Ophthalmol.* 113: 119-129 (1995).

tomographic imaging, can be developed as a method of high-resolution vascular imaging to ultimately address these limitations in cardiac diagnostics. We have demonstrated with initial *in vitro* studies that OCT identifies plaques which are structurally unstable with a resolution, between 4 and 20 μm, superior to that of any clinically available imaging technology. In addition, OCT was capable of generating high contrast between tissue microstructure, and imaging could be performed through even the most heavily calcified samples. We also directly compared OCT with high frequency ultrasound, the current imaging technology with the highest resolution (110 μm). OCT consistently identified tissue microstructure which was not seen in the ultrasound images. Finally, an imaging catheter was developed which will be used for *in vivo* imaging. The catheter is less than 1 mm in diameter and no transducer was present within it, resulting in a relatively low cost in construction. Future studies will focus on catheter based imaging and optimizing the system for patient imaging. The latter will include improved data acquisition rates, optimizing the wavelength of the incident source, and combination with spectroscopy.

1.15.7 Histological Correlation of Laser-Induced Retinal Lesions with OCT Images

With an increase in the medical technologies using lasers, a thorough understanding of laser-tissue interactions is necessary. In particular, interactions with sensitive ocular structures have been of interest for both clinical medical applications and for laser safety. Much of the laser-tissue interaction data obtained from ocular structures has relied on the use of (1) *in vivo* ophthalmoscopic or fluorescein angiographic examination,[70] or (2) post-mortem histological preparations to assess effects and extent of possible damage.[71]

In the past year, we have correlated results obtained in our investigation of laser-induced retinal injury using OCT to the corresponding histological preparations. OCT is a new imaging technique which utilizes fiber optic based low-coherence interferometry along with a super luminescent diode laser source to provide micron scale cross-sectional

tomographic images of retinal structure. In contrast to conventional histopathology techniques, OCT is noninvasive, and thus it is possible to image laser induced retinal lesions at different time intervals ranging from immediately after laser exposure to several days. This provides a direct tomographic measurement of the formation and healing response to laser retinal exposure. Comparative OCT studies were performed at Brooks Air Force Base in Texas, using cw argon, nanosecond, picosecond, and femtosecond, laser-induced lesions. Histopathology was acquired at selected time points for comparisons with OCT images.

Direct comparisons between OCT images and corresponding histology reveal consistent tissue morphology in addition to several types of artifacts that result from histological processing. Because OCT images represent the *in vivo* orientation of the microstructure, preparation artifacts can be identified. In addition, with the clinical ophthalmic implementation of OCT, our histological correlations provide a more definitive explanation of what retinal structures are represented by the differential optical backscatter measured with the OCT instrument.

These studies are the first *in vivo* microstructural measurements which document the formation and healing response of retinal laser exposure. The histological evidence confirms the observations made using OCT and improves our understanding of laser-tissue interactions by enhancing visualization of retinal structure. These results have important implications for ophthalmic laser surgery as well as establishing laser retinal injury standards.

1.15.8 Optical Coherence Tomographic Investigation of Developing Embryonic Morphology

Recent advances in molecular biology techniques have permitted the site-specific insertion of predetermined mutations into embryos for the investigation of normal and abnormal development. Not only does this have fundamental scientific interest, but also has the potential for the study, understanding, and possible cure for genetic diseases. Currently, there are several imaging modalities available to observe the expression of genetic

70 J.S. Schuman, M.R. Hee, C.A. Puliafito, C. Wong, T. Pedut-Kloizman, C.P. Lin, E. Hertzmark, J.A. Izatt, E.A. Swanson, and J.G. Fujimoto, "Quantification of Nerve Fiber Layer Thickness in Normal and Glaucomatous Eyes using Optical Coherence Tomography: A Pilot Study," *Arch. Ophthalmol.* 113: 586-596 (1995).

71 R. Birngruber, V.-P. Gabel, and F. Hillenkamp, "Threshold Criteria and Derivation of Safe Levels for Laser Radiation," in *Current Concepts in Ergophthalmology*, eds. B. Tengroth, D. Epstein, A. Anseth, A. Hedin, A.H. Keeney, M.J. Roper-Hall, and D.H. Sliney (The Hague, The Netherlands, 1978).

mutations including light, confocal, and electron microscopy, but these typically require small, transparent, or fixed specimens. Progress has also been made to reimplement the clinical magnetic resonance imaging, computed-tomography, and ultrasound technologies as high-resolution, microscopic imaging modalities. High-resolution MRI,[72] CT,[73] and ultrasound backscatter microscopy[74] have achieved resolutions on the order of 15-50 μm. These techniques, however, still present limitations in acquisition time, resolution, cost, or complexity. Optical coherence tomography (OCT) offers the ability to image *in vivo* developing morphology in many of the animal models used for genetic studies. In addition, OCT has the potential to rapidly and repeatedly acquire optical histology to assess development and to identify the expression of normal and abnormal genes.

We have acquired OCT images of *in vivo* developing morphology from several developmental biology animal models (leopard frog, African frog, zebra fish) which demonstrate that numerous anatomical features can be distinguished with high resolution (figure 15). Images correlate strongly with corresponding histology. Optical histology performed with OCT preserves the *in vivo* orientation of the morphology and can be used to identify normal and abnormal morphology. Images can be acquired from single specimens throughout development thereby allowing longitudinal studies to be performed rather than acquiring multiple time-points from multiple specimens. Cross-sectional images can also be acquired at spatial intervals and later used to reconstruct a three-dimensional representation of the specimen. From this 3D data set, arbitrary section planes can be repeatedly obtained to highlight specific anatomy. This is in contrast to the one-time orientation with histological sectioning.

Optical coherence tomography offers numerous possibilities for the investigation of *in vivo* embryonic morphology and for developmental biology in general. Utilizing solid-state laser sources, cellular resolutions of 4 μm have already been demonstrated.[75] This high-resolution instru-

ment has potential for the microscopic investigation of normal and abnormal developing biology.

1.15.9 Publications

Bouma, B.E., G.J. Tearney, S.A. Boppart, M.R. Hee, M.B. Brezinski, and J.G. Fujimoto. "High Resolution Optical Coherence Tomographic Imaging Using a Modelocked Ti:Al2O3 Laser Source." *Opt. Lett.* 20(13): 1486-1488 (1995).

Brezinski, M.B., G.J. Tearney, B.E. Bouma, J.A. Izatt, M.R. Hee, E.A. Swanson, J.F. Southern, and J.G. Fujimoto. "Optical Coherence Tomography for Optical Biopsy: Properties and Demonstration of Vascular Pathology." *Circulation.* Forthcoming.

Hee, M.R., J.A. Izatt, E.A. Swanson, D. Huang, J.S. Schuman, C.P. Lin, C.A. Puliafito, and J.G. Fujimoto. "Optical Coherence Tomography for Micron-resolution Ophthalmic Imaging." *IEEE Eng. Med. Bio.* 14: 67 (1995).

Hee, M.R., J.A. Izatt, E.A. Swanson, D. Huang, J.S. Schuman, C.P. Lin, C.A. Puliafito, and J.G. Fujimoto. "Optical Coherence Tomography of the Human Retina." *Arch. Ophthalmol.* 113: 325-332 (1995).

Hee, M.R., C.A. Puliafito, C. Wong, J.S. Duker, E. Reichel, J.S. Schuman, E.A. Swanson, and J.G. Fujimoto. "Optical Coherence Tomography of Macular Holes." *Ophthalmol.* 102: 748-746 (1995).

Hee, M.R., C.A. Puliafito, C. Wong, J.S. Duker, E. Reichel, J.S. Schuman, E.A. Swanson, and J.G. Fujimoto. "Optical Coherence Tomography of Central Serous Chorioretinopathy." *Am. J. Ophthalmol.* 120: 65-74 (1995).

Hee, M.R., C.A. Puliafito, C. Wong, J.S. Duker, E. Reichel, B.K. Rutledge, J.S. Schuman, E.A. Swanson, and J.G. Fujimoto. "Quantititative

---

[72] B. Lorentz, "Morphologic Changes of Chorioretinal Argon Laser Burns during the First Hour Post Exposure," *Lasers in Life Sci.* 2(3): 207-226 (1988).

[73] R.E. Jacobs and S.E. Frase, "Magnetic Resonance Microscopy of Embryonic Cell Lineages and Movements," *Sci.* 263: 681-684 (1994).

[74] E.J. Morton et al., "Three-dimensional X-ray Microtomography for Medical and Biological Applications," *Phys. Med. Biol.* 35: 805-820 (1990).

[75] B.E. Bouma, G.J. Tearney, S.A. Boppart, M.R. Hee, M.B. Brezinski, and J.G. Fujimoto, "High Resolution Optical Coherence Tomographic Imaging Using a Modelocked Ti:Al2O3 Laser Source," *Opt. Lett.* 20(13): 1486-1488 (1995).
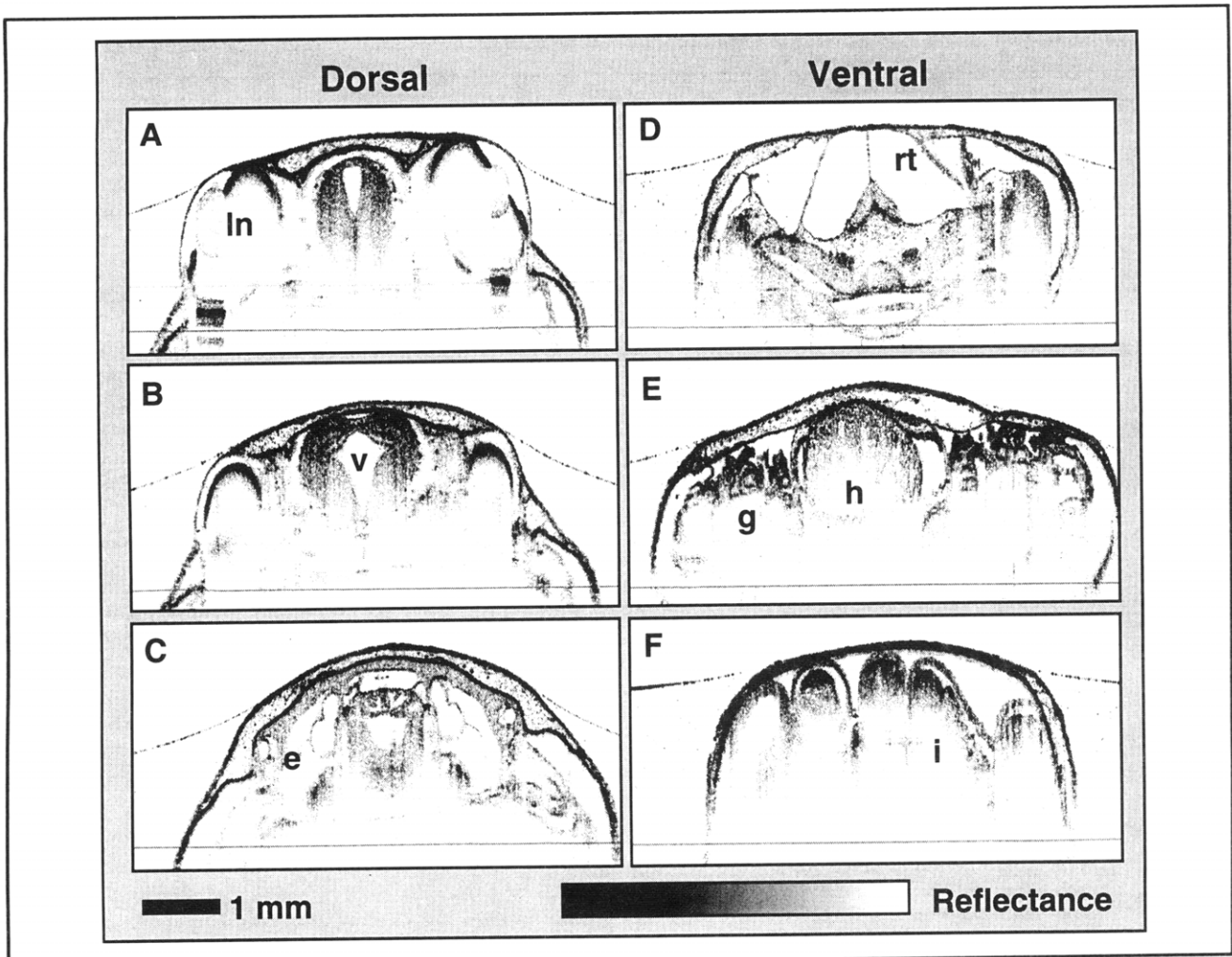
Figure 15. Cross-sectional OCT images of an *in vivo* leopard frog tadpole. Images were acquired from the dorsal (A-C) and the ventral (D-F) sides of the specimen to highlight particular anatomical features. Abbreviations: e = ear, g = gills, h = ventricle of heart, i = intestine, ln = lens of eye, rt = respiratory tract, v = fourth ventricle of brain.

Assessment of Macular Edema with Optical Coherence Tomography." *Arch. Ophthalmol.* 113: 119-129 (1995).

Hee, M.E., J.A. Izatt, E.A. Swanson, D. Huang, C.P. Lin, J.S. Schuman, C.A. Puliafito, and J.G. Fujimoto. "Optical Coherence Tomography of the Human Retina." *Arch. Ophthalmol.* 113: 325-332 (1995).

Puliafito, C.A., M.R. Hee, C.P. Lin, E. Reichel, J.S. Schuman, J.S. Duker, J.A. Izatt, E.A. Swanson, and J.G. Fujimoto. "Imaging of Macular Diseases with Optical Coherence Tomography (OCT)." *Ophthalmol.* 102: 217-229 (1995).

Puliafito, C.A., M.R. Hee, C.P. Lin, E. Reichel, J.S. Schuman, J.S. Duker, J.A. Izatt, E.A. Swanson, and J.G. Fujimoto. "Imaging of Macular Diseases with Optical Coherence Tomography." *Ophthalmol.* 102: 217-229 (1995).

Schuman, J.S., M.R. Hee, C.A. Puliafito, C. Wong, T. Pedut-Kloizman, C.P. Lin, E. Hertzmark, J.A. Izatt, E.A. Swanson, and J.G. Fujimoto. "Quantification of Nerve Fiber Layer Thickness in Normal and Glaucomatous Eyes using Optical Coherence Tomography: A Pilot Study." *Arch. Ophthalmol.* 113: 586-596 (1995).

Tearney, G.J., M.E. Brezinski, M.R. Hee, B. Bouma, J.A. Izatt, E.A. Swanson, J.F. Southern, and J.G. Fujimoto. "Optical Biopsy in Human Tissue using Optical Coherence Tomography and Microscopy." Paper presented at the Conference on Lasers and Electro-Optics, Optical Society of America, May 1995.

Tearney, G.J., M.E. Brezinski, B.E. Bouma, J.F. Souther, and J.G. Fujimoto. "High Resolution Imaging of Gastrointestinal Tissue using Optical Coherence Tomography." Annual Meeting of the American Gastrointestinal Association, May 1996.

Tearney, G.J., B.E. Bouma, S.A. Boppart, B. Golubovic, E.A. Swanson, and J.G. Fujimoto. "High Speed Optical Coherence Tomography." Paper presented at the Conference on Advances in Photon Migration, Orlando, Florida, March 1996.

Tearney, G.J., S.A. Boppart, B.E. Bouma, M.E. Brezinski, N. Weissman, J.F. Southern, and J.G. Fujimoto. "Scanning Single Mode Fiber Optic Catheter/Endoscope for Optical Coherence Tomography." *Opt. Lett.* Forthcoming.

Turnbull, D.H., et al. "Ultrasound Backscatter Microscope Analysis of Early Mouse Embryonic Brain Development." *Proc. Nat. Acad. Sci.* 92: 2239-2243 (1995).

1.16 EUV and Soft X-ray Laser Research

Sponsor

MIT Lincoln Laboratory
Contract BX-5098

Project Staff

Professor Peter L. Hagelstein, James G. Goodberlet, Marc Fleury,[76] Dr. Martin H. Muendel,[77] William Hodge,[78] Shourov Chattevji

Significant amplification in the EUV and soft x-ray regime was first demonstrated in 1984 at Lawrence Livermore National Laboratories (LLNL) and Princeton University. Since that time, short wavelength laser research has been explored at a large number of laboratories in the U.S. and around the world. When we began our efforts at MIT, it was thought that kilojoule pump lasers were required to drive short wavelength lasers using the collisional scheme. Recombination lasers could be studied at much lower energy, but these lasers have historically been plagued with difficulties in achieving a high total gain length. We set out to try to develop EUV lasers using a table-top facility in order to pump collisional lasers at the joule level instead of at the kilojoule level.

Since that time, many things have occured. We succeeded in developing a laboratory for studying laser-produced plasmas relevant to short wavelength lasers, and we have tested a number of laser schemes. In 1992, we demonstrated apparent gain in Ni-like Nb at 204 Å using a pump energy later estimated to be 2-3 joules. Later on, experiments on recombining H-like boron plasmas indicated the presence of somewhat higher gain.

Elsewhere, laser plasma experiments on the Ne-like and Ni-like sequences have provided systematic demonstrations of gain in a wide variety of neon-like ions from S to Mo and in the nickel-like sequence from Sn to Au.

Significant gain has been detected in neon-like ions with somewhat less than 100 J pump energy being required for the observation of gain in Ti. The field has been stimulated by a number of notable recent results including: the demonstration of significant gain in recombining Li at 135 Å pumped by a femtosecond laser; the development of a saturated neon-like argon laser in a capillary discharge; the demonstration of very high gain in neon-like titanium pumped using a few joule nanosecond pulse to create a plasma and then a few joule picosecond pulse to heat it; and the demonstration of optical field ionization for creating a plasma for collisional excitation in Pd-like Xe.

During the past few years, U.S. funding in this area has been very low outside of LLNL; one hopes that this will change. The advent of short wavelength lasers will stimulate research in a number of areas: nonlinear spectroscopy will be extended into the EUV and soft x-ray regimes; new EUV and x-ray optical instruments and techniques have come into existence; and short wavelength lasers have been successfully applied to the problem of imaging of dense plasmas and biological systems. Some think that these lasers will find applications in the semiconductor industry for use either in fabrication or inspection of devices.

In the following sections, we discuss recent developments in our effort at MIT.

---

[76] Graduate student, Ecole Polytechnique, Paris, France.

[77] Polaroid Corporation, Cambridge, Massachusetts.

[78] High Energy Laser Associates, Oakland, California (Sponsor: National Science Foundation SBIR Grant 90-06960).

1.16.1 Constant Dose Gain Measurements

Amplified spontaneous emission in long, narrow lasers has been of interest for many years in laser science; it is especially important in short wavelength laser research since the reflectivity of the best mirrors in this regime (which are multilayer mirrors) is poor. If the gain is assumed to be constant, then the laser intensity exponentiates according to

$$I(\lambda) = I_0(e^{\alpha(\lambda)L} - 1)$$

along rays that traverse the full length of the laser L. The laser linewidth is usually quite narrow $\lambda/\Delta\lambda \sim 10^4$, so that the observed intensity for a wavelength averaged diagnostic is

$$< I > = I_0 \int (e^{\alpha(\lambda)}L - 1) \, d\lambda$$

This integral depends weakly on the details of the gain lineshape α; it is typically approximated by the Linford expression

$$< I > \sim \frac{(e^{\alpha L} - 1)^{3/2}}{(\alpha L e^{\alpha L})^{1/2}}$$

An experimental determination of the presence of gain or loss in short wavelength laser experiments is usually done by measuring the wavelength averaged intensity versus the laser length L, and then fitting the results to the Linford curve to determine α. For a high-gain system, αL can be more than 10, and it is obvious that the laser works as a laser. For smaller values of αL, it is possible to fit the Linford curve to estimate the gain coefficient α, but the accuracy of the resulting estimate will depend on the linearity of the detection system and its geometry.

One way to minimize the nonlinearities associated with the detection system is to use a constant dosage measurement scheme.[79] In such a scheme, the experiments are carried out to produce approximately the same signal at the detector for different conditions. To measure gain, values of the wavelength averaged intensity are needed at different lengths L; if the gain is low, then the signal will be approximately proportional to the length. In order to develop a constant dosage scheme for such a measurement, the signal at the detector must somehow be doubled for a measurement at length L/2 to compare with a measurement at length L. This was accomplished in our laboratory by using film to sum up the results from several shots and then scaling the number of shots taken according to the inverse of the length. For example, four shots summed at length L can be compared in a constant dosage measurement with eight shots summed at length L/2, and so forth.

In our previous experiments on a possible recombination laser in H-like B, fitting the wavelength averaged I from streak camera measurements at different lengths L yielded an apparent result of several gain lengths in H-like B at 262 Å.[80] A confirmation of this result was attempted taking advantage of the constant dose measurement scheme. It was found that for the same experimental conditions that the signal grew linearly as measured with the constant dosage technique as shown in figure 16. The previous measurements are believed to be in error and can be attributed to nonlinearities in the detection system.
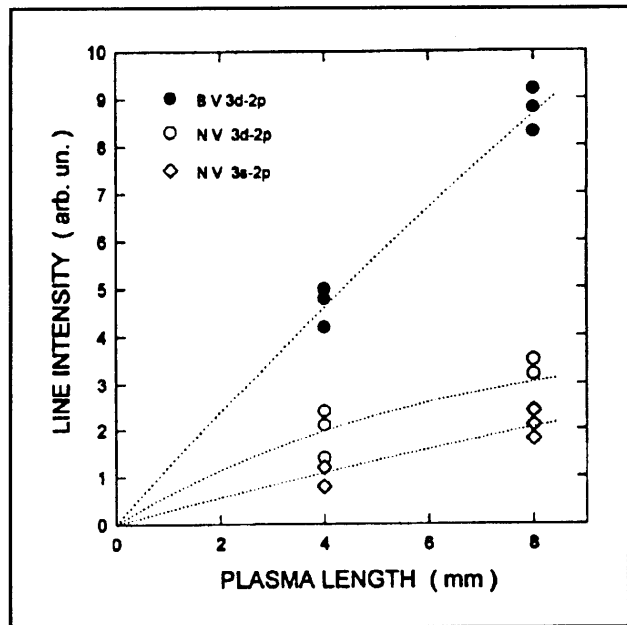

Figure 16. Wavelength averaged intensity I versus length L for H-like B.[79]

[79] J. Goodberlet, *An Experimental Investigation of a Table-Top, Laser Drive Extreme Ultraviolet Laser*, Ph.D. diss., Dept. of Electr. Eng. and Comput. Sci., MIT, 1996.

[80] J. Goodberlet et al., "Observation of Gain in a Recombining H-like Boron Plasma," *J. Opt. Soc. Am. B* 12: 980 (1995).

1.16.2 Survey of Recombination Laser Schemes

Our earlier experimental efforts on recombination lasers focused on the 3d-2p transition at 262 Å in H-like B. This work was stimulated by number of reports of the observation of significant gain on the same transition in H-like C at low energy. The absence of detectable gain in our experiments as discussed above is a relatively recent result, the explanation of which is a current research question. It was decided to explore experimentally other recombination laser schemes with our facility, including the He-like 3d-2p, Li-like 4f-3d and 5g-4f, and Na-like 5g-4f schemes.

The motivation for these experiments comes from a number of considerations. Gain on many of these transitions has been studied in laser plasma experiments at other laboratories, in many cases with low pump laser energy. Additionally, the experimental requirements for the development of gain at longer wavelengths tend to be less demanding. One other consideration included the issue of radiation trapping; while radiation trapping is expected to impact many of the recombination laser schemes (and has the potential to spoil the gain). The Li-like 5g-4f scheme will not be affected as much by radiation trapping and has been shown to give high gain in related experiments.

Representative of the results is the case of the 4f-3d transition in Li-like F at 381.8 Å. The observation and identification of the candidate laser line was reasonably straightforward, which is typical of recombination lasers in the EUV and soft x-ray regimes. Using a CaF_2 target, the candidate laser line was observed to be the dominant feature locally in the spectrum[81] (see figure 17). Intensity versus length experiments showed a linear growth of intensity with length; no detectable gain was observable (see figure 18).[81]
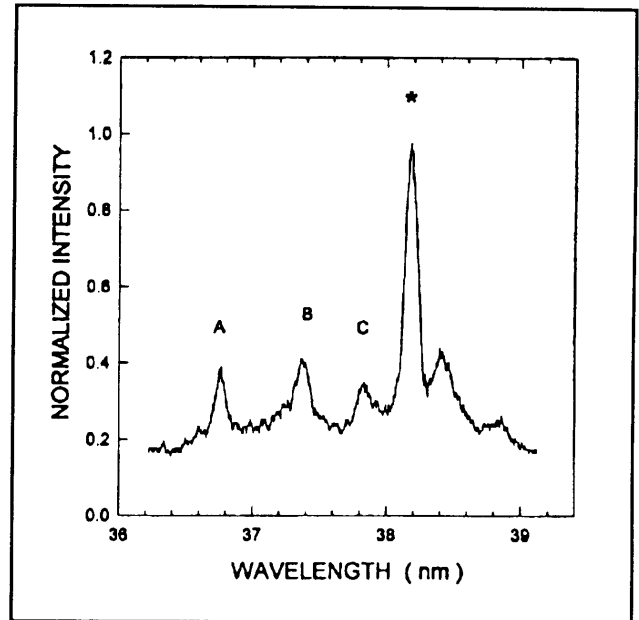

Figure 17. Li-like F spectrum. Line identifications are: * - Li-like F 4f-3d (381.8 Å); A - Li-like F 4d-3p (367.9 Å); B - Mg-like Ca (373.9 Å); C - Mg-like Ca (378.1 Å).[81]
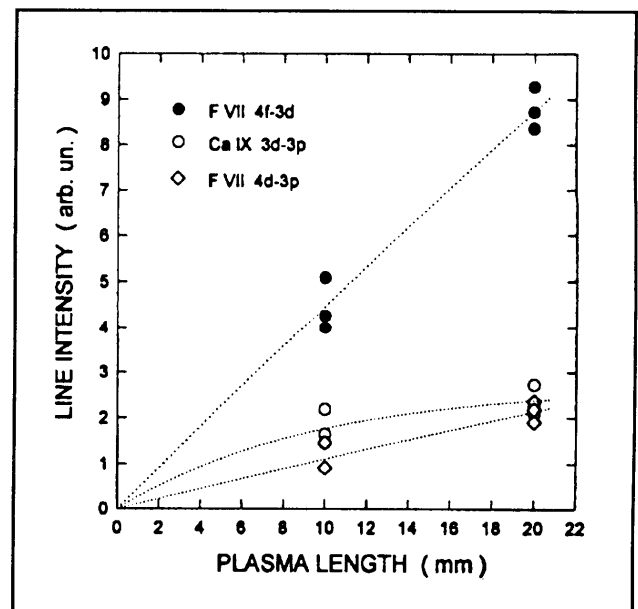

Figure 18. Li-like F spectrum intensity versus length measurement.[81]

[81] J. Goodberlet, *An Experimental Investigation of a Table-Top, Laser Drive Extreme Ultraviolet Laser*, Ph.D. diss., Dept. of Electr. Eng. and Comput. Sci., MIT, 1996.

Experiments were performed additionally on: He-like 1s3d ^{1}D – 1s2p ^{1}P transition in He-like C at 267.2 Å, the 5g-4f transition in Li-like Mg at 404.3 Å, and the 5g-4f transition in Na-like Ca at 401.6 Å (see figure 19).[82]
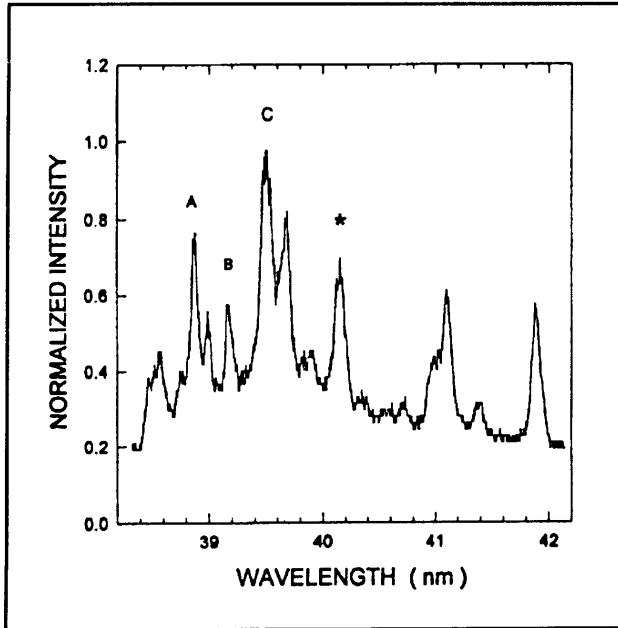

Figure 19. Na-like Ca spectrum. Line identifications are: * - Na-like Ca 5g-4f (401.6 Å); A - Mg-like Ca (388.8 Å); B - Li-like F (291.8 Å); C - Mg-like Ca (395.0 Å).[82] The observation of the candidate laser line in Na-like Ca may be the first time that this line has been identified.

1.16.3 Survey of Collisional Excitation Laser Schemes

The first experimental campaign to detect gain conducted on our laser facility focused on a candidate laser line in Ni-like Nb,[83] as reported in previous *RLE Progress Reports*. In this work, a strong line appeared at 204 Å and based on a number of considerations, this line was identified as the J=0 4d-4p laser transition showing weak gain. The arguments supporting this included: (1) the line was within a few tenths of an Angstrom of the expected wave-length from isoelectronic interpolation; (2) it appeared to be significantly brighter than the nearby Cu-like lines under conditions where the highest gain was expected; (3) the line showed a strong threshold behavior with intensity, consistent with what would be expected of a transition within an excited state manifold; (4) an intensity versus length measurement showed weak exponentiation. One problem with this result is that the streak data showed the emission from the candidate laser line to typically last longer than would be possible if pumped by collisional excitation alone (although short temporal emission of this line was observed in the presence of a long background on occasion).

The development of the constant dose measurement technique has indicated that nonlinearities in detector and film response can mimic the presence of gain in an intensity versus length experiment as described above. While much effort went into the calibration of the nonlinear response of the measurement system in these experiments, we now consider that the intensity versus length measurement for this experiment may also suffer from similar problems. Consequently, the present experiment results weakens the previous claims. This experiment needs to be repeated using a constant dosage measurement scheme. Such an experiment was attempted, but it was not possible to reproduce the pumping conditions of the experiment with the existing laser set up (we are not able safely to reach the same intesity levels as required for these experiments as discussed in previous *RLE Progress Reports*).

There have been numerous recent reports of gain in low-Z, Ne-like ions, such as argon, calcium, and titanium. Gains in the range of a few per centimeter have been observed in a number of laboratories under a wide range of conditions. We attempted to observed the candidate J=0 laser line in Ne-like Ca and Ne-like Ti. Numerous experiments were performed using both line pumping and a spot focus. We were unable to obtain a clear observation of the laser line, although in Ca some emission was observed in the vicinity of the expected wavelength (see figure 20).

82 J. Goodberlet, *An Experimental Investigation of a Table-Top, Laser Drive Extreme Ultraviolet Laser*, Ph.D. diss., Dept. of Electr. Eng. and Comput. Sci., MIT, 1996.

83 S. Basu et al., "Amplification in Ni-like Nb at 20.4 nm Pumped by a Table-top Laser," *Appl. Phys. B* 57: 303 (1993).
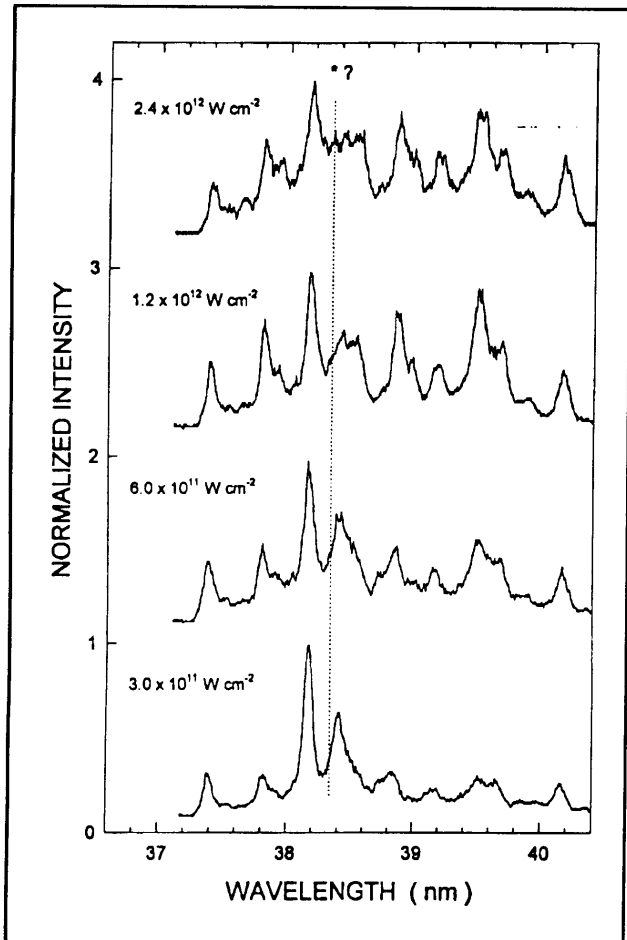
Figure 20. Ca spectra for increasing pump-laser intensity. The pump-laser intensity was increased for a 5 mm long plasma. A spectral feature was observed at the location of the candidate Ne-like Ca 3p-3s lasing line, marked with the dotted line.

1.16.4 Axicon and Tube Experiments

The efficiency of EUV and soft x-ray lasers as demonstrated at various laboratories around the world is typically quite low, on the order of 10^{-6} conversion of incident pump laser light to output laser radiation. For EUV lasers to be applied, we need to develop more efficient designs. In laser-plasma experiments, usually a high-intensity laser ablates plasma from material that is initially a solid. In the course of the irradiation, much of the thermal energy that is deposited is converted into kinetic energy that drives the ablation. Much of the remaining energy drives ionization in nearby high-density material, and some is lost to radiation. Eventually, a small fraction of the energy is used to populate the upper laser state, but at the high-electron density that maximizes the laser gain, most of this upper state population is lost to collisional deexcitation.

From these considerations, it is easy to see why such short wavelength lasers are inefficient. To improve significantly the overall efficiency, a way must be found to reduce the loss for each of the individual mechanisms. To this end, we proposed some time ago the possibility of using a low-density plasma to develop an efficient short wavelength laser. The collisional scheme at low density can be made to be quite efficient (the intrinsic efficiency of the kinetics can approach 10 percent). The basic problem then is how to create and heat such a plasma efficiently. Inverse bremsstrahlung absorption becomes ineffecient at low density, and it is not possible to absorb a significant fraction of the incident pump energy into such a plasma using a single pass. We proposed the use of an axicon and tube to provide a way to re-use the pump laser light. Another approach to this problem is to use optical field ionization instead of inverse bremsstrahlung absorption to create a plasma and to couple energy to the plasma; this approach was recently demonstrated at Stanford University.[84]

An axicon and tube was recently designed[85] and fabricated at the Lawrence Livermore National Laboratory[86] using diamond turning on oxygen-free copper. This optic was designed to focus an incident-collimated pump laser beam at 1.0 μ into a line using a reflective axicon, and the tube refocuses the light four times to produce a plasma roughly 6 cm in length. The optic was constructed with a surface figure precision on the order of a micron and with a local surface smoothness on the order of 25 Å. Preliminary experiments are currently being performed with this optic, and a plasma has been generated in argon.[87] Intense focusing of the light to a line within the axicon and tube on the micron scale is predicted, and plasma formation observed with single-pulse irradiation is consistent.

[84] B.E. Lemoff et al., "Demonstration of a 10-Hz Femtosecond-pulse-driven XUV Laser at 41.8 nm in XE IX," *Phys. Rev. Lett.* 74: 1574 (1995).

[85] M. Fleury, Ph.D. diss., *Ecole Polytechnique*, forthcoming.

[86] The optic was built by Tony Demeris of LLNL during the spring of 1995.

[87] M. Muendel, M. Fleury, S. Chatterji, and P. Hagelstein, presented at the 1996 *International X-ray Laser Conference*, Lund, Sweden.

1.17 Elastic and Inelastic Neutron Hopping

Sponsors

Electric Power Research Institute
    Contract RP3170-25
ENECO

Project Staff

Professor Peter L. Hagelstein with contributions from Steve Crouch-Baker and Michael McKubre

For several years, a number of anomalies have been reportedly observed in metal hydrides. The claims of excess heat production, if correct, are perhaps the most important. In PdD, the largest excess power production claimed so far is a factor of about three over the input power; many laboratories claim observations of smaller effects. The total energy claimed to have been generated involves on the order of a hundred times the chemical energy that would be released if the cathode were replaced by an explosive and detonated. Recent claims have also been made by a few individuals of the observation of power gains on the order of 50 or more in NiH electrolysis experiments, with considerably larger energy production per cathode atom. If this larger effect proves to be real, then it would perhaps follow that commercial applications are not far off; such a strategy is currently being pursued by a company, Clean Energy Technologies, Inc.

Claims have also been made for the generation of tritium and other radioactive isotopes, and neutron generation has been reported. If these effects are real, then they are clearly secondary processes compared to whatever primary process is responsible for heat production.

Currently, neither heat production nor any of the other claimed effects is generally accepted by the scientific community. These results, if real, indicate the presence of a new physical effect that allows nuclear reactions to take place in a way very different from that which have been studied in nuclear physics for more than 60 years. Most physicists do not believe in such a possibility and simply reject all claims.

From our perspective, the key experiments relating to heat production in PdD appear to be reproducible at a number of laboratories; they work with different types of calorimetry; they show similar dependencies on loading and current at different laboratories;

and the effects seem to be correlated with the average rate of exothermic desorption. If there is a new physical effect, then according to the experimental claims it is a very big effect; a primary goal of our research is to try to understand theoretically what is the basic effect.

We have found during the past several years two new physical mechanisms that may be relevant: (1) neutron hopping and (2) anomalous energy transfer by phonon frequency shifting. Elastic neutron hopping is proposed to be analogous with electron hopping as a second order process. This effect is found to be maximized in deuterated vacancy phase NiH and PdH. Anomalous energy transfer requires the presence of a phonon laser and would allow neutron hopping to occur between inequivalent nuclei. Inelastic neutron hopping is proposed to be responsible for excess heat and tritium production. These and related issues are discussed in the following sections.

1.17.1 The Neutron Mixed Valence Model

The premise of neutron hopping theory is that there exists a finite coupling between bound neutron states and continuum neutron states. The origin of this process is ultimately in correlation effects associated with the nuclear structure problem.[88] For example, in a multiconfigurational Hartree-Fock description of a nucleus, configurations including both bound and free neutrons should be included. Strong force interaction matrix elements will lead to a coupling between configurations with bound neutrons and with free neutrons.

The largest effects are expected to occur when the free neutron has no net angular momentum (the centripetal potential keeps a slow neutron away from the nucleus in the case of non-zero angular momentum); stable isotope pairs that would be described by this theory occur in the elements H, He, Si, Cd, Sn, Te and Xe. The first such example that we studied was the coupling between ground state ^{29}Si and ground state ^{28}Si plus a free s-wave neutron.

In the crudest single configuration description, ^{29}Si can be thought of as a ^{28}Si core plus an outer 2s valence neutron. Mixing between the ^{29}Si ground state and the ionized system would involve a single neutron excitation. From Brillouin's theorem, it is known that in the Hartree-Fock description, direct coupling between such states is forbidden; conse-

---

[88] P.L. Hagelstein, "Neutron Hopping in Crystals," submitted to *Phys. Rev. B.*

quently, we must go to second order to obtain matrix elements of the type required. One can use perturbation theory to include correlation effects

$$< \Psi_0 | H | \Phi_k > = \sum_n \frac{< \Phi_0 | V_s | \Phi_n > \cdot < \Phi_n | V_s | \Phi_k >}{E_0 - E_n} + \cdots$$

The resulting matrix element are expected to be on the order of the characteristic strong force potential (MeV) weighted by the square root of the ratio of nuclear to atomic volumes

$$< \Psi_0 | H | \Phi_k > \sim V_s \sqrt{\frac{V_n}{V_a}}$$

which is on the order of 100 meV. We have examined the second order coupling in detail in the case of ^{29}Si and ^{2}H; in the case of ^{29}Si, the numerical results from summing over several hundred configurations are consistent with such an estimate.

In the case of ^{2}H, the intermediate states are isobaric deuteron configurations (corresponding to internal proton and neutron excitations), and the resulting nuclear matrix element is estimated to be on the order of 500 meV. There is a significant uncertainty in this number originating from the current uncertainty in isobaric content of the deuteron. We estimate the interaction matrix element to be linear in the isobaric deuteron fraction according to

$$< \Psi_0 | H | \Phi_k > \sim 500 \, p_{iso}(\%) \, meV$$

A 1 percent deuteron isobar content corresponds to a 500 meV interaction matrix element. Theoretical estimates for the total isobaric content of the deuteron in the literature are in the range of a few percent.

In the case of isolated nuclei, the coupling discussed above leads to minor corrections in the nuclear energy and very little else. For a collection of nuclei in a lattice, it seems appropriate to adopt models that have been successful to describe analogous effects for electrons. The relevant model in this case is a version of the periodic Anderson model, which might be termed a neutron mixed valence model;[88] the associated Hamiltonian is

$$\hat{H} = \sum_{k,\sigma} \varepsilon_k \hat{c}_{k,\sigma}^\dagger \hat{c}_{k,\sigma} + \sum_{i,\lambda} \varepsilon_\lambda \hat{X}_{\lambda\lambda}(i) + \sum_{i,\mu} \varepsilon_\mu \hat{X}_{\mu\mu}(i)$$

$$+ \frac{1}{\sqrt{N}} \sum_i \sum_{k,\sigma\lambda,\mu}$$

$$[V_{\lambda\sigma\mu}(k) e^{-ik \cdot \hat{R}_i} \hat{c}_{k,\sigma}^\dagger \hat{X}_{\lambda\mu}(i) + V_{\mu\sigma\lambda}(k) e^{ik \cdot \hat{R}_i} \hat{X}_{\mu\lambda}(i) \hat{c}_{k,\sigma}]$$

This Hamiltonian includes the valence neutron energy, the free neutron energy, and the coupling between bound and free neutrons. The physical content of this model is minimal; it describes basic configuration interaction effects for a collection of nuclei in a lattice. This Hamiltonian differs from the electron mixed valence Hamiltonian in two respects: (1) phonon interactions are more important since neutrons are much heavier than electrons, and (2) the valence and conduction bands are widely separated (by MeV in the neutron model). We have assumed in our work a harmonic lattice, which is suppressed in the above Hamiltonian.

1.17.2 Predicted Neutron Hopping Rates

The neutron mixed valence model can be used to examine the possibility of elastic neutron hopping from one site to a neighboring site. For two nuclei in isolation, this probability is calculated from this model to be exponentially small due to extreme destructive interference among the different free neutron states. In a lattice, the model predicts that resonant Bragg scattering causes a relatively small number of free neutron states to avoid this destructive interference, which gives rise to a small probability of the valence neutron being delocalized on the atomic scale. If the delocalized neutron is resonantly captured by a neighboring nucleus, then a neutron hopping event will have occurred.

We can calculate neutron hopping rates directly from second order perturbation theory[88]

$$\Gamma = - \left[\frac{2}{\hbar} \right] \times$$

$$Im < \hat{V}[E - \hat{H}_0]^{-1} \hat{V}^\dagger [E - \hat{H}_0]^{-1} \hat{Q} \hat{V} [E - \hat{H}_0]^{-1} \hat{V}^\dagger >$$

where the transition operator $\hat{V}$ is taken from the neutron mixed valence Hamiltonian

$$\hat{V} = \frac{1}{\sqrt{N}} \sum_i \sum_{k,\sigma\lambda,\mu} V_{\mu\sigma\lambda}(k) e^{-ik \cdot \hat{R}_i} \hat{X}_{\mu\lambda}(i) \hat{c}_{k,\sigma}$$

The operator $\hat{Q}$ is a projection operator.

Elastic neutron hopping rates for a variety of crystals are shown in figure 21. In the high temperature limit, the Mössbauer contribution to the neutron hopping rate is proportional to an exponential factor

$$\Gamma_0 \sim e^{-\Delta\varepsilon_{ij}/kT}$$

The effective barrier energy $\Delta\varepsilon_{ij}$ for neutron hops from site i to site j within a unit cell is approximately

$$\Delta\varepsilon_{ij} = \frac{1}{2} M\omega_0^2 |\Delta R_{ij}|^2$$

where M is the mass of the nucleus after a neutron hop, where $|\Delta R_{ij}|$ is the atomic site separation in a unit cell, and where ω_0 is the classical frequency associated with the nucleus consistent with the experimentally observed Debye-Waller factor.

Some interesting physics can be seen in the predicted hopping rates. Considerable destructive interference among the free neutron Bragg states occurs, and finite neutron hopping rates are pre-

dicted only when this effect is minimized. To minimize the destructive interference, the number of Bragg states must be minimized; this is predicted to occur at high temperature in materials where phonons are generated via recoil most easily. To maximize neutron hopping, we seek crystals with "soft" inter-atomic potentials. The potentials for hydrogen in metal hydrides, especially PdH, are predicted to be superior in this regard to all monatomic crystals. The largest neutron hopping rates are predicted to occur in metal hydrides that have extreme host lattice metal vacancy content (as can be seen in figure 21), because the local hydrogen potential in such materials is even softer.

1.17.3 Predicted Gamma Emission Rates

We computed neutron hopping rates that result from a bound neutron developing a small probability of being delocalized by resonant Bragg scattering in a lattice. A bound neutron that is delocalized may be captured by a neighboring nucleus if the capture process is exothermic. This neutron capture event would be expected to be accompanied by the emission of a gamma, which could then be observed. We have proposed this as a way to indirectly demonstrate experimentally that elastic neutron hopping occurs.[88]

In the case of virtual neutrons originating from deuterium, neutron capture is energetically allowed (since the neutron is most weakly bound on deuterium of all stable nuclei). The gamma capture
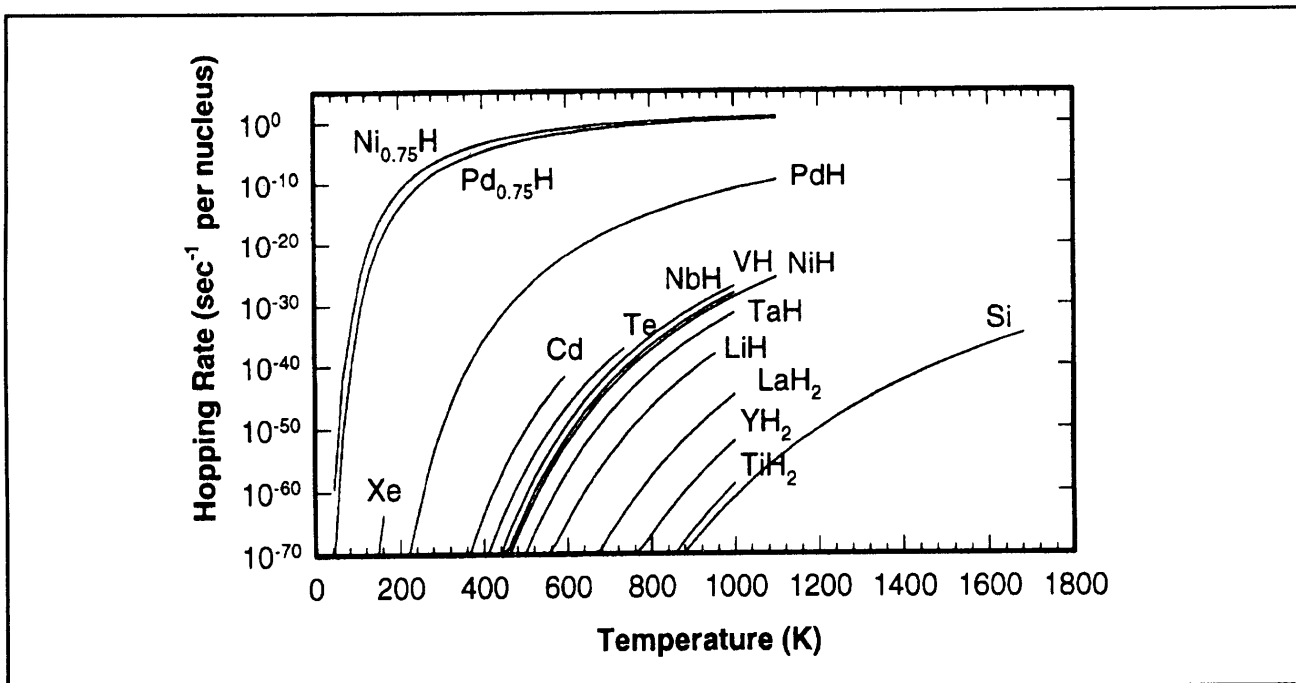

Figure 21. Predicted neutron hopping rates in various crystals assuming an optimum isotopic mix.

rate can be estimated from the neutron mixed valence model by adding a complex potential due to (n, y) absorption to the Hamiltonian

$$\hat{H}_0 + \hat{V} \rightarrow \hat{H}_0 + \hat{V} - i\hat{U}$$

from which the gamma emission rate can be computed to be[88]

$$\Gamma_y = -\left[\frac{2}{\hbar I_n^3}\right] \text{Re} < \hat{V}\hat{U}\hat{V}^\dagger [E - \hat{H}_0]^{-1} \hat{V}\hat{V}^\dagger >$$

$$-\left[\frac{2}{\hbar I_n^3}\right] \text{Re} < \hat{V}\hat{V}^\dagger [E - \hat{H}_0]^{-1} \hat{V}\hat{U}\hat{V}^\dagger >$$

Gamma emission can come about in a metal hydride through capture by deuterium nuclei or through capture by the host metal nuclei. While the cross section for virtual neutron capture is expected to be much larger for the host metal nuclei, the probability that a virtual neutron will be at the site of

a host metal lattice has been computed and is quite small. Consequently, the dominant decay process is expected to be gamma capture by deuterium, leading to the emission of a 4.0 MeV gamma. The associated gamma emission rate for this type of process is shown in figure 22. The largest gamma emission rates are predicted for deuterated vacancy phase nickel hydride and palladium hydride. The gamma emission rate for vacancy phase deuterated nickel hydride is shown in figure 23.

1.17.4 Thermodynamics of Vacancy Phase NiH and PdH

An experimental demonstration of elastic neutron hopping according to the predictions of the neutron mixed valence model outlined above requires the production of vacancy phase metal hydrides in cubic centimeter-sized samples. Fukai and Okuma demonstrated recently that extreme vacancy production occurs thermodynamically in NiH and PdH at high temperature at a rate limited by vacancy diffusion from the surface.[89]
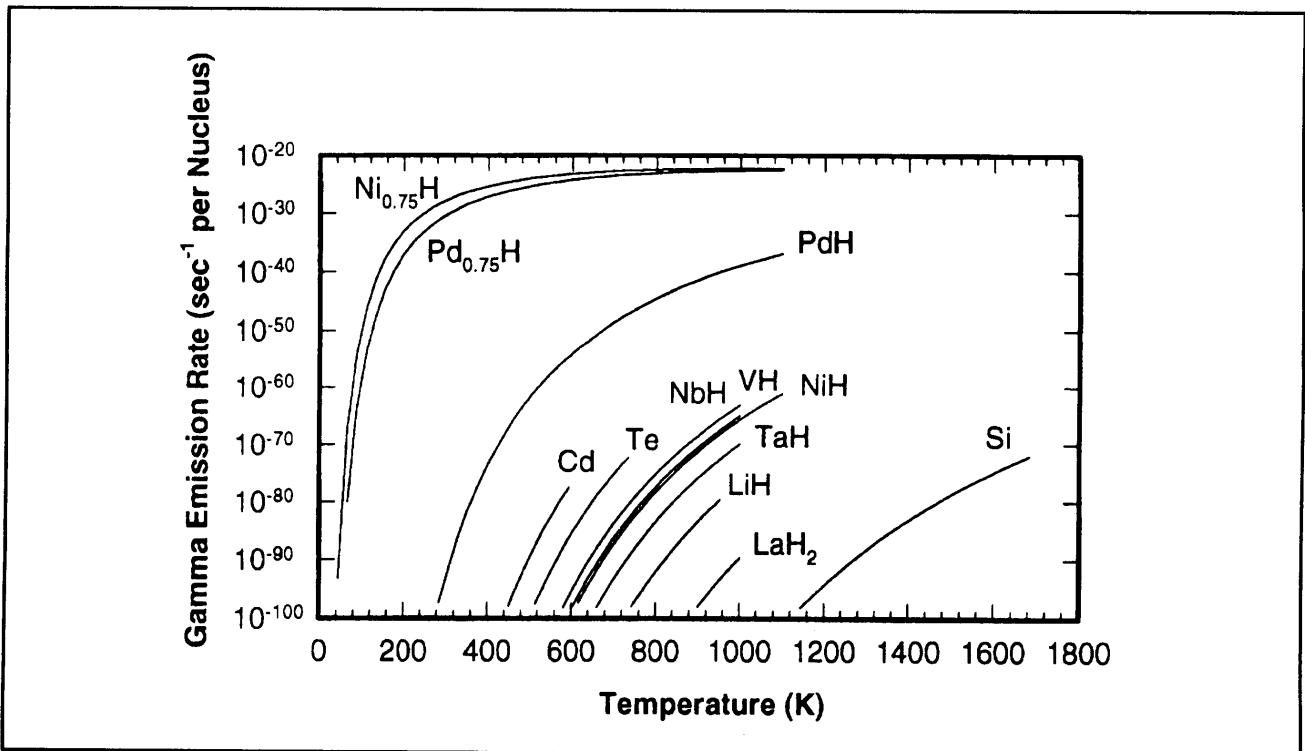

Figure 22. Gamma emission rates estimated in the high temperature limit for a variety of materials. Gamma emission due to same-element capture is assumed in all cases (consistent with 4.0 MeV emission in the deuterated metal hydrides).

[89] Y. Fukai and N. Okuma, "Evidence of Copious Vacancy Formation in Ni and Pd under High Hydrogen Pressure," *Jpn. J. Appl. Phys.* 32L: 1256 (1993); Y. Fukai and N. Okuma, "Formation of Superabundant Vacancies in Pd Hydride under High Hydrogen Pressures," *Phys. Rev. Lett.* 73: 1640 (1994).

We have recently examined a simple model for the thermodynamics of vacancy phase PdH and NiH. The equilibrium vacancy concentration x_v can be determined from the entropy S_k and enthalpy h_f of vacancy formation through

$$\frac{x_v}{1 - x_v} = e^{S_k/k}e^{-h_f/kT}$$

The entropy of point defect formation S_k is known for a variety of materials at low concentration, and according to Fukai and Okuma is of the order of 2.5k (we follow Fukai and Okuma and use $e^{S_k/k} = 10$ here for both Ni and Pd).

The enthalpy of formation h_f has been studied theoretically using density functional theory, and from experiment. At high loading, the enthalpy of formation is approximately linear in the hydrogen concentration. If we define x_c to be the hydrogen concentration referenced to the number of host metal atom sites (and independent of the number of vacancies), then

$$h_f \approx h_f^0 + x_c\frac{dh_f}{dx_c}$$

We can then determine the hydrogen loading x_c required to establish an equilibrium vacancy concentration x_v; we obtain

$$x_c = -\left[\frac{dh_f}{dx_c}\right]^{-1}\left\{h_f^0 - kT\left[\frac{S_k}{k} - \ln\frac{x_v}{1-x_v}\right]\right\}$$

We have plotted in figure 24 results from this model for a variety of specified vacancy concentrations.

This model predicts that the vacancy phase is thermodynamically favored at high loading under normal conditions; both NiH and PdH are unstable against spontaneous vacancy phase formation at high loading, rate limited only by the vacancy diffusion rate. This provides the basis for possible routes for vacancy phase sample generation: We could in principle generate internal sources of vacancies (by electron or ion bombardment), and then transiently heat the sample. Alternatively, we could attempt to grow vacancy phase NiH or PdH on a highly loaded vacancy phase substrate.
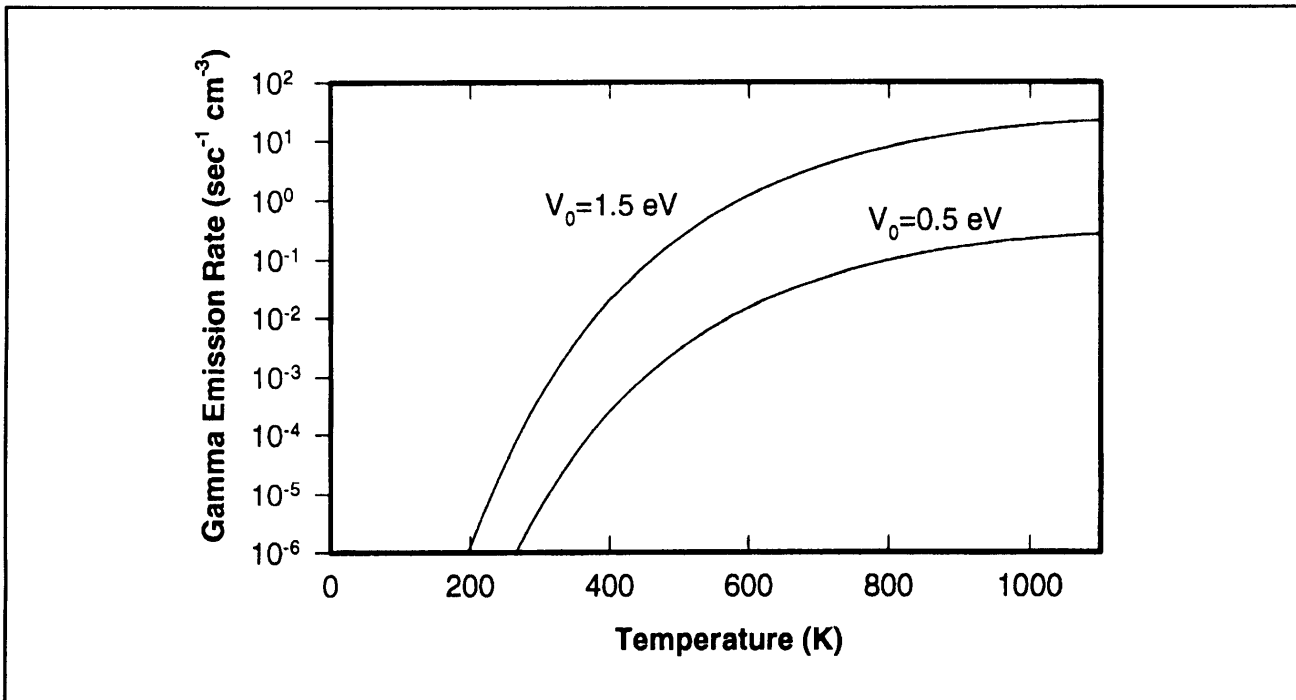

Figure 23. Gamma emission rate for deuterated nickel hydride $Ni_{0.75}H_{0.33}D_{0.67}$ as a function of temperature. Significant uncertainties exist in the nuclear transition matrix element. We have included predictions for what we consider to be a conservative estimate ($V_0 = 0.5$ eV, corresponding to 1 percent deuteron total isobar content) and also for a less conservative estimate ($V_0 = 1.5$ eV, corresponding to 3 percent total isobar content) that is representative of isobar content values found in the literature.
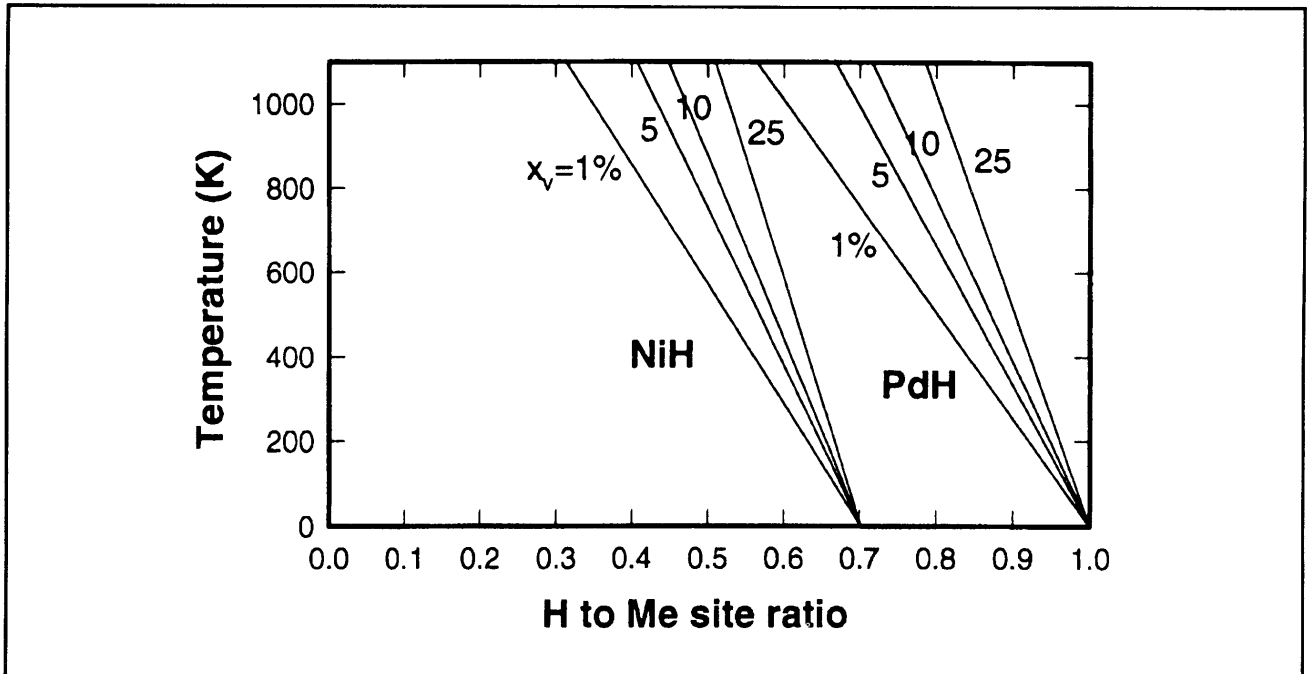
Figure 24. Estimated temperature and hydrogen loading required for the production of vacancy phase $Pd_{1-x}H$ and Ni_{1-x}

1.17.5 Inelastic Neutron Hopping

The possibility of neutron hopping as an elastic process has been discussed above; here we consider the possibility of inelastic neutron hopping, in which a neutron hops from one nucleus to an inequivalent nucleus, and the excess energy is dissipated. One motivation for our interest in this possibility comes from numerous reports of excess heat, tritium, neutrons, and significant induced radioactivity in electrochemical experiments involving palladium and from reports of excess heat in NiH experiments. While these experiments are not currently accepted by the scientific community, many of these effects have been reproduced numerous times in different laboratories. Should these experiments eventually be accepted as being fundamentally correct, then an explanation will be required; inelastic neutron hopping is one candidate explanation.

The basic idea is as follows: Inelastic neutron hopping would involve the transfer of a neutron from a nucleus to an inequivalent nucleus, with the energy difference transferred elsewhere. It is not difficult to show that such a large energy cannot be transferred through a general interaction that

creates large numbers of low energy quanta. Instead, we have examined the possibility that such an energy transfer can proceed through a minor frequency shift of a macroscopic oscillator that is highly excited.

It has been known for decades (and now discussed in textbooks) that a small number of phonon modes of a lattice can jump across a phonon band gap due to a modification of the mass or force constants associated with an atom at one site in the lattice.[90] In molecular physics, the effect is known as the Duschinsky effect[91] when the molecular force constants are altered due to an electronic transition. A prototypical example of a lattice version of this effect is the case of hydrogen and deuterium impurities in a dilute metal hydride.[92] If initially there are N_H hydrogen atoms and N_D deuterons in a metal lattice, then there will be $3N_H$ phonon modes near the hydrogen resonant frequency ω_0 and $3N_D$ phonon modes near the deuteron resonant frequency $\omega_0/\sqrt{2}$. A neutron capture by a proton causes these numbers to change neutron capture. There are $N_H - 1$ hydrogen atoms with $3(N_H-1)$ associated phonon modes at ω_0, and $N_D + 1$ deuterons with $3N_D + 1$ associated phonon modes

[90] P.G. Dawber and R.J. Elliott, "The Vibrations of an Atom of Different Mass in a Cubic Crystal," *Proc. Phys. Soc.* 81: 483 (1963).

[91] F. Duschinsky, "Zur Deutung der Elektronenspektren mehratomiger Molekule," *Acta Physiochemica* (URSS) 7: 521 (1937).

[92] P.L. Hagelstein, "Possibility of Mössbauer Effect in Neutron Capture," *Hyperfine Interact.* 92: 1059 (1994).

at $\omega_0/\sqrt{2}$. In this example, the phonon modes are impurity continuum modes within a band, and it is the three lowest energy phonon modes of the hydrogen impurity band that jump to form three new highest modes of the deuteron band.

It can also be shown that, to within a reasonable approximation, that the phonons originally in a mode that jumps undergo a frequency shift according to the frequency shift of the phonon mode. The total associated energy transfer is then[92]

$$\Delta E = n_{ph}\hbar\delta\omega$$

where n_{ph} is the number of phonons initially in the modes that jump, and $\delta\omega$ is the associated frequency shift. In the limit that the number of phonons n_{ph} is great, then the resulting energy transfer will be large. For example, phonon lasers were developed soon after the advent of the optical laser; with a phonon laser it is possible to achieve a very high number of phonons in a mode. Phonon lasers have been demonstrated up to 0.87 THz by optical pumping of impurity atoms in a crystal.[93] We have developed and published a model for the anomalous broadening and shifting of the gamma transition associated with neutron capture by protons in a dilute metal hydride due to frequency shifts of thermally generated and phonon laser produced phonons.[92]

Consequently, a mechanism that enables an inelastic neutron hopping effect may exist, provided that an appropriate phonon band gap is present, and that in addition a phonon laser is operating. We have begun an investigation of a model for inelastic neutron hopping mediated by phonon exchange through the frequency shift of a large number of phonons. Within the framework of the neutron mixed valence model, the associated inelastic hopping rate can be computed from[94]

$$\Gamma = -\left[\frac{2}{\hbar I_n^2}\right] \mathrm{Im} < \hat{V}_{bc} V_{cb'}^2 [E - \hat{H}_0]^{-1} \hat{V}_{b'c} \hat{V}_{cb} >$$

where the index b refers to orbitals of the donor nuclei, where c refers to the continuum, and where b′ refers to orbitals of the acceptor nuclei. This theory is formally closely related to the elastic

neutron hopping theory discussed above. For an exothermic neutron hopping reaction, if the energy is transferred to the lattice, then there exists the possibility that the lattice will decay. The basic theory for this has been developed and published earlier;[95] the primary lattice decay modes are likely to be Coulomb mediated electronic and atomic recoils that alter the number of vacancies. If we assume that this is so, then the resulting reaction rate for inelastic neutron hopping in the high temperature limit is[94]

$$\Gamma \sim \left[\frac{V_D^2 V_A^2 N_A N_D N}{2 I_D^2}\right] \times$$

$$\sum_{i \neq j} f_\mu^{(i)} f_\lambda^{(j)} \frac{e^{-\Delta\varepsilon_{ij}/kT}}{\det^{1/2} M_{ij}} \frac{1/\tau_L}{(I_D - I_A)^2 + (\hbar/2\tau_L)^2}$$

In this formula, V_D and V_A are the associated nuclear interaction matrix elements discussed previously; N_D and N_A here are the number of contributing Brillouin zones for the donor and acceptor nuclei, respectively; I_D and I_A are the donor and acceptor neutron binding energies; $\Delta\varepsilon_{ij}$ is the associated effective barrier energy for neutron hopping (it can be of a similar magnitude as in the case of elastic neutron hopping). In this expression, τ_L is the time associated with the lattice decay, within the framework of a model in which real energy transfer to the lattice occurs (as opposed to this being a virtual process). This type of model predicts reaction rates for inelastic neutron hopping that can occur at a nontrivial fraction of the elastic hopping rate in the presence of a suitable phonon laser.

Such a theory is naïve relative to the energy exchange with the phonons. Energy transfer to a lattice by phonon modes frequency shifting upward results in a final state lattice with the excess energy distributed over a large number of phonon modes on the high energy side of the phonon band gap. If the phonon band gap is associated with vacancies (specifically, if a change in the number of vacancies causes phonon modes to jump the band gap), then the lattice can decay through electronic or atomic recoil (as long as it changes the number of vacancies). The lattice decay time for this type of

[93] P. Hu, "Stimulated Emission of 29-cm⁻¹ Phonons in Ruby," *Phys. Rev. Lett.* 44: 417 (1980).

[94] P.L. Hagelstin, "New Lattice-nucleus Coupling Mechanisms and Possible Energy Production," *Proceedings of the Symposium on Fusion Engineering* (SOFE '95), forthcoming.

[95] P.L. Hagelstein, "Lattice-Induced Atomic and Nuclear Reactions," *Trans. Fusion Tech.* 26: 461 (1994).

process is computed to be extremely short—so short that perturbation theory is not appropriate.[95]

Consequently, an inelastic neutron hop within this theory would occur by virtual energy transfer to the lattice and subsequent decay by a large number of low energy recoil events. That the process is virtual appears to be extremely important within the theory, because it means that a much smaller number of phonons is required to be present in the mode for the overall process to occur. In essence, the lattice only has to have the possibility of accommodating a relatively small amount of energy in order to mediate the decay by recoil of a large amount of energy.[94]

1.18 Many-photon Configuration Space Theory and Applications

Project Staff

Professor Peter L. Hagelstein

We describe in the following sections some ideas that have been developed recently relating to light propagation in nonlinear fibers, and possible applications of the resulting theory. The motivation for much of this works came about from a series of discussions at the MIT Laboratory of Computer Science during the summer of 1994 concerning the possibility of quantum computation, and the application of quantum optics techniques to the problem.[96]

The premise of quantum computation seemed to require the use of single photons, in order to generate interference effects equivalent to the prerequisite quantum superposition. Yet it is very difficult to arrange for useful nonlinear interactions between single photons, because the associated fields are so weak. We would have liked to use optical pulses for fast switching, but single photon interference patterns resulting from the optical pulses would not produce the correct probability distributions needed for quantum computation.

The brainstorm that evolved in these meetings was to think about the quantum soliton itself as a single quantum object and consider the possibility of designing a new class of optical elements that would switch optical solitons as quantum objects. For example, an optical soliton incident on a beamsplitter would be fractionated into two optical pulses with partial energy depending on the reflection and transmission coefficients. This would not be appropriate for our purposes; we require a

beam divider that would swtich the soliton either one way or another as an intact quantum object in order to implement our vision of a quantum computer.

Unfortunately, the quantum radiation theory that is currently used for nonlinear optics problems is not particularly well-adapted for the treatment of such problems. The essential reason for this is that the questions posed above are configuration space questions, while the radiation theory is cast in terms of a second quantization formulation. To make progress, we require a configuration space description for quantum nonlinear optics. Such a project had never been attempted and ultimately proved to be quite a significant task. In the sections that follow, we provide a summary of some of the issues, results, and applications.

1.18.1 Photon Configuration Space Theory

To explain what a configuration space Schrödinger equation is for a photon, it is perhaps simplest to think first about the more familiar problem of what is the configuration space equation for a particle. The Schrödinger equation in configuration space for a nonrelativistic particle in quantum mechanics is

$$\hat{E}\psi(r, t) = \left[\frac{|\hat{p}|^2}{2m} + V(r) \right] \psi(r, t)$$

with $\hat{E} = i\hbar \frac{\partial}{\partial t}$ and $\hat{p} = -i\hbar\nabla$. This equation is used to describe the time evolution of the probability amplitude ψ relevant for the calculation of quantum effects (interference, tunneling, etc.).

Problems in quantum optics are presently not treated with configuration space models; instead, such problems are typically formulated using a second quantized theory. In the case of particles, a second quantized model is develop through the quantization of the wavefunction ψ to give

$$\hat{E}\Psi = \int \hat{\psi}^\dagger \left[\frac{|\hat{p}|^2}{2m} + V(r) \right] \hat{\psi} \, d^3r \, \Psi$$

This we recognize as a Schrödinger equation in second quantization. Here $\hat{\psi}$ and $\hat{\psi}^\dagger$ are field operators. This type of theory would appear as part of a description of the probability amplitude for a collection of noninteracting particles (or consist of

---

96 P.L. Hagelstein, N. Margolus, and M. Biafore, "Towards an Optical Quantum Computer Project," unpublished (1994).

probabilities that the collection contains different numbers of noninteracting particles). Second quantized models of particles are of considerable use in many-body quantum physics applications.

Quantum radiation problems are usually formulated using an underlying description of the radiation field that derives from a second quantized Hamiltonian of the form

$$\hat{E}\Psi = \int \frac{1}{2}\varepsilon_0 |\hat{E}|^2 + \frac{1}{2}\mu_0 |\hat{H}|^2 d^3r \, \Psi$$

where $|\hat{E}|^2$ and $|\hat{H}|^2$ are quantum squared electric and magnetic field operators. In this type of theory, the probability amplitude Ψ describes the radiation field, that will be in general a superposition of states each with a different number or different distribution of photons. Modern quantum optics research is described ultimately in terms of this type of theory (augmented with matter interactions, and typically cast in terms of a Heisenberg picture, instead of a Schrödinger picture).

In the case of particles, problems can be formulated and worked either in first quantization or in second quantization. The first quantization approach tends to be mathematically simpler; the second quantization approach tends to solve harder problems when the quantum problems can be solved. In the case of photons, quantum mechanical problems are uniformly worked using second quantization techniques; first quantization methods have not been applied to quantum radiation problems to any significant degree. The reason for this concerns difficulties associated with the photon configuration space, which has been said by some noted authors not to exist.

We have recently applied quantum field theory techniques developed for the analogous relativistic electron quantum theory to the photon problem[97] and have obtained a configuration space photon equation of the form

$$\hat{E}\psi(r, t) = \hat{\Lambda}_{++}\Big[\alpha_M \cdot c\hat{p} + \hat{V}_\varepsilon\Big]\hat{\Lambda}_{++}\psi(r, t)$$

In this theory, ψ is a 6 × 1 column vector, α_M is a 6 × 6 spin-1 matrix, and V_ε is a 6 × 6 nonlocal operator that includes the effect of matter from linear response theory applied directly to QED. The Λ_{++}

operators are projection operators that restrict interactions to the positive energy spectrum of possible quantum states.

The resulting configuration space theory suffers from a variety of problems that are well known in the literature: For example, the configuration space theory is not covariant, photons cannot be localized (so that all interactions with matter or other photons are inherently nonlocal), and $|\psi|^2$ cannot be interpreted as a probability density. While these problems are serious, the method that we used to develop photon configuration space equations maps the configuration space problem onto an equivalent second quantized QED problem, which is free of the problems which plague the configuration space theory.

Consequently, it is now possible to apply the configuration space theory systematically to quantum radiation problems, such as occurs in quantum nonlinear optics, to obtain formulations that are fundamentally simpler. In addition, the configuration space method provides additional insights and analogs to well known configuration space particle problems that may be obscured in a second quantized formulation.

1.18.2 Photon Configuration Space Description of Soliton Propagation

One of the most basic quantum problems of interest in quantum optics is quantum soliton propagation along an optical fiber. This problem has been analyzed by numerous authors, using formulations in second quantization. The results of these models indicate that the solitons largely behave as classical solitons with quantum fluctuations appearing in the center of mass location and in the relative phases of the component number states. We have applied the configuration space theory to this problem in order to benchmark the theory, and to understand quantum soliton propagation from a configuration space viewpoint.[98]

A soliton in a fiber from a photon configuration space point of view is a collection of photons that are bound around a photonic center of mass (photons do not have mass, but the concept of a center of mass is convenient here). The photons interact with other photons with an attractive approximate delta function interaction potential, forming a collective photonic ground state, that is a

[97] P.L. Hagelstein, "Many-Photon Configuration Space Equations," submitted to *Phys. Rev. A.*

[98] P.L. Hagelstein, "Application of Photon Configuration Space Equations to Optical Soliton Propagation," *Phys. Rev. A,* forthcoming.

bosonic analog to a nuclear ground state. In the case of the nuclear states, it is possible in the non-relativistic approximation to exactly separate center of mass and relative mass coordinates; we seek an equivalent separation for the photon configuration space wavefunction.

The configuration space theory in one dimension leads to a soliton number state wavefunction Ψ_n that can be written as a product

$$\Psi_n = \psi(x, t)\Phi(\xi_1, \bullet, \xi_{n-1})$$

where $\psi(x,t)$ is a wavefunction for the soliton center of mass, and where $\Phi(\xi_1, \bullet, \xi_{n-1})$. The Schrödinger equation for the photonic center of mass in a moving frame can be written

$$i\hbar \frac{\partial}{\partial t} \psi(x, t) = -\frac{\hbar^2}{2m} \frac{\partial^2}{\partial x^2} \psi(x,t)$$

where m here is a parameter that is related to the fiber dispersion. This Schrödinger equation is the same as that for a free particle; consequently, the configuration space analogy for soliton center of mass propagation is that of a free quantum particle. If the center of mass is initially localized, then the associated probability amplitude will spread; the spread in time is found from

$$\Delta x^2(t) = \Delta x_0^2 + \frac{\Delta p_0^2}{4m^2} t^2$$

When the relevant parameters are computed for the quantum soliton, it is found that this formula gives correctly the quantum fluctuations computed from the second quantized models. In this case, the underlying origin of the effect is perhaps simpler to understand.[98]

1.18.3 Soliton Configuration Space Position-Phase Wavefunctions

The second quantized theories naturally include states with different photon number, and it is of interest to compute the phase shifts and fluctuations in phase that occur for soliton propagation.

This problem is well known in the quantum soliton literature, and the computation of the spread in phase has been computed using second quantized techniques. We decided to attempt a computation of this effect using the configuration space approach.

We introduced the Fourier transform of the center of mass wavefunction weighted by the Fock space mixing coefficients;[98] for example, we define

$$\psi(x, \theta, t) = \sum_n a_n \psi_n(x,t) e^{in\theta}$$

The inverse transform is

$$a_n \psi_n(x,t) = \int_0^{2\pi} \frac{d\theta}{2\pi} \psi(x, \theta, t) e^{-in\theta}$$

The function $\psi(x, \theta, t)$ is termed a position-phase wavefunction. Although it could be argued that $\psi(X, \theta, t)$ is not really a wavefunction at all, it was found to behave very much like a wavefunction. The time evolution of $\psi(x, \theta, t)$ is given by

$$\psi(x, \theta, t) = \sum_n \int \frac{dk}{2\pi} a_n \psi(k) e^{ikx} e^{in\theta} e^{-iE_n(k)t/\hbar}$$

The energy $E_n(k) = \hbar\omega_n(k)$ is made up of the center of mass kinetic energy and the soliton binding energy. The dependence of energy on soliton number and center of mass momentum leads to a frequency of the form

$$\omega_n(k) =$$

$$\omega_0 + (n - n_0) \frac{\partial \omega}{\partial n} + \frac{1}{2} (n - n_0)^2 \frac{\partial^2 \omega}{\partial n^2} + \frac{1}{2} k^2 \frac{\partial^2 \omega}{\partial k^2}$$

The evolution equation for the position-phase wavefunction is then

$$i \frac{\partial}{\partial t} \psi(x, \theta, t) = \left[\omega_0 + \frac{\partial \omega}{\partial n} \left(-i \frac{\partial}{\partial \theta} - n_0 \right) + \frac{1}{2} \frac{\partial^2 \omega}{\partial n^2} \left(-i \frac{\partial}{\partial \theta} - n_0 \right)^2 - \frac{1}{2} \frac{\partial^2 \omega}{\partial k^2} \frac{\partial^2}{\partial x^2} \right] \psi(x, \theta, t)$$

This equation is simplified if we transform into a moving frame in θ; we obtain[98]

$$i \frac{\partial}{\partial t} \psi(x, \theta, t) =$$

$$\left[-\frac{1}{2} \left(\frac{\partial^2 \omega}{\partial n^2} \right) \frac{\partial^2}{\partial \theta^2} - \frac{1}{2} \left(\frac{\partial^2 \omega}{\partial k^2} \right) \frac{\partial^2}{\partial x^2} \right] \psi(x, \theta, t)$$

Using Ehrenfest's theorem, we obtain exact evolution equations for the fluctuations in both x and θ that are solved to yield

$$\Delta x^2(t) = \Delta x_0^2 + \frac{\Delta p_0^2}{4\hbar^2} \left(\frac{\partial^2 \omega}{\partial k^2} \right) t^2$$

$$\Delta \theta^2(t) = \Delta \theta_0^2 + \frac{\Delta n_0^2}{4} \left(\frac{\partial^2 \omega}{\partial n^2} \right) t^2$$

After substituting in the appropriate parameters specific to soliton propagation, these formulas are found to agree with the equivalent results obtained from second quantized models. Moreover, the evolution of the squeezing factor is also in agreement between the two models; this allows for a particularly simple physical interpretation of soliton squeezing as spreading of an initially localized free-particle wavefunction in θ-space.[98]

1.18.4 Quantum Soliton Center of Mass Interferometry

Configuration space wavefunctions are naturally adapted for the calculation of interference phenomena. While we are familiar with single photon interference effects, much less is currently understood about many photon interference effects. Such interference effects could be observed in principle with an interferometer of the type illustrated in figure 25. In this case, the configuration space soliton wavefunction at the detector is composed of two contributions from the different paths through the interferometer
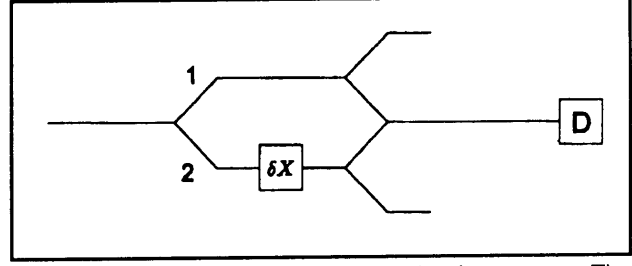
$$\Psi = \Psi_1 + \Psi_2$$

Figure 25. Soliton center of mass inteferometer. The soliton is assumed to be switched as a quantum object by quantum beam dividers (normal beamsplitters would fractionate the soliton).

The probability of detection is then proportional to

$$p_D = |\Psi_1|^2 + |\Psi_2|^2 + <\Psi_1|\Psi_2> + <\Psi_2|\Psi_1>$$

We can develop formulas in terms of the soliton center of mass position-phase wavefunctions for such calculations; it can be shown that the expectation value of a many-photon configuration space operator can be expressed in terms of the center of mass position-phase wavefunction as

$$< \hat{Q} > = < \psi(x, \theta, t) | \hat{Q}' | \psi(x, \theta, t) >$$

The "transformed" operator $\hat{Q}'$ can be related formally back to the matrix elements of $\hat{Q}$; we find

$$\hat{Q}' = \sum_{nm} \int \frac{d\theta'}{2\pi} e^{i(n\theta - m\theta')} < \Phi_n | \hat{Q} | \Phi_m > e^{(\theta' - \theta) \frac{\partial}{\partial \theta}}$$

The classical state position-phase wavefunction for soliton propagation is[99]

$$\psi(x, \theta, t) = [2\pi \Delta x_0 \Delta \theta_0 [1 + i\Phi_x(t)][1 + i\Phi_\theta(t)]]^{-\frac{1}{2}}$$

$$\times e^{ik_0 x} e^{in_0 \theta} e^{-i\omega_0 t} e^{-\frac{(x - <x>)^2}{4\Delta x_0^2[1 + i\Phi_x(t)]}} e^{-\frac{(\theta - <\theta>)^2}{4\Delta \theta_0^2[1 + i\Phi_\theta(t)]}}$$

This solution is characterized by eight basic parameters: the mean position $<x>$ and phase $<\theta>$; the center of mass momentum k_0 and the photon number n_0; the initial spread in center of mass position Δk and phase $\Delta \theta$; the dispersion of the center of mass position and phase as parameterized by the corresponding angles $\Phi_x(t)$ and $\Phi_\theta(t)$. The

99 P.L. Hagelstein, "Application of Photon Configuration Space Equations to Optical Soliton Propagation," *Phys. Rev. A*, forthcoming; P.L. Hagelstein, "Application of Photon Configuration Space Equations to Optical Soliton Center of Mass Interferometry," submitted to *Phys. Rev. A.*

expectation values of position and phase evolve according to

$$< x > = x_0 + \frac{\partial \omega}{\partial k} t$$

$$< \theta > = \theta_0 + \frac{\partial \omega}{\partial n} t$$

The initial center of mass spread Δx_0 and phase spread $\Delta \theta_0$ are in general arbitrary. However, for soliton propagation beginning with a classical soliton state the initial spread in center of mass position is related to the single photon spread through

$$\Delta x_0^2 = \frac{< x^2 >}{n}$$

in a sector of Fock space, and the initial spread in phase is due to the spread in photon number

$$\Delta \theta_0^2 = \frac{1}{4n_0^2}$$

The remaining time evolution of the wavefunction is accounted for in the increase in the angles Φ_x and Φ_θ, which are given by

$$\Phi_x(t) = \frac{1}{2} \frac{\partial^2 \omega}{\partial k^2} \frac{\Delta k}{\Delta x} t$$

$$\Phi_\theta(t) = \frac{1}{2} \frac{\partial^2 \omega}{\partial n^2} \frac{\Delta n}{\Delta \theta} t$$

We can use these results to computer the detection probability for various center of mass interferometry schemes. For example, if the interferometer produces a relative position delay with no accompanying phase delay or squeezing, then the detection probability is[100]

$$p_D = \frac{1}{2} \left[1 + e^{-\frac{\delta x^2}{8\Delta x_0^2}} \cos \frac{2\pi n_0 \partial x}{\lambda} \right]$$

If the interferometer produces a relative phase delay with no accompanying position delay or squeezing, then the detection probability is

$$p_D = \frac{1}{2} \left[1 + e^{-\frac{\delta \theta^2}{8\Delta \theta_0^2}} \cos(n_0 \delta \theta) \right]$$

The configuration space theory can be used systematically to evaluate soliton center of mass inteferometers, with arbitrary combinations of delays in position and in phase, momentum and photon number, as well as the degree of squeezing in either position or in phase. These results are new. Currently there exists no interferometers of this type; it is not presently certain that they can even be constructed. The motivation for pursuing such interferometry is the potential for obtaining λ/n interference fringes with light of wavelength λ.[101]

1.18.5 Possible Adiabatic Quantum Switching of a Soliton Center of Mass

We have applied the configuration space photon theory to nonlinear directional couplers and fiber Y-dividers.[102] While the development of a general quantum theory for such devices using a second quantization formulation has not yet been reported, the configuration space model has been applied directly with no particular difficulty. The immediate goal of our effort was the design of a quantum beam divider that could put a "macroscopic" quantum soliton into a superposition of two states. From the results of the analysis, we would be able to determine whether such a device could be developed.

The configuration space many-photon equations for a nonlinear coupler can be separated approximately into a center of mass equation and a relative coordinate equation; the approximate separation is implemented through the use of a Born-Oppenheimer type product wavefunction

$$\Psi(R,\{\xi\}, t) = \psi(R,t)\Phi_R(\{\xi\})$$

---

[100] P.L. Hagelstein, "Application of Photon Configuration Space Equations to Optical Soliton Center of Mass Interferometry," submitted to *Phys. Rev. A*.

[101] P.L. Hagelstein, "Many-Photon Configuration Space Equations," submitted to *Phys. Rev. A*; P.L. Hagelstein, "Application of Photon Configuration Space Equations to Optical Soliton Propagation," *Phys. Rev. A*, forthcoming; P.L. Hagelstein, "Application of Photon Configuration Space Equations to Optical Soliton Center of Mass Interferometry," submitted to *Phys. Rev. A*.

[102] P.L. Hagelstein, "Application of Photon Configuration Space Equations to Optical Soliton Center of Mass Switching," submitted to *Phys. Rev. A*.

The center of mass dynamics is described by a Schrödinger equation of the form

$$\left[i\hbar \frac{\partial}{\partial t} - v_{gr}P_x \right] \psi(R, t) =$$

$$\left[\frac{P_x^2}{2M_\parallel} + \frac{|P_T|^2}{2M_\perp} + V_\xi(R) \right] \psi(R, t)$$

The effective potential $V_\xi(R)$ seen by the center of mass wavefunction is given by

$$V_\xi(r) = \; < \Phi_R | H_\xi + V(R, \{\xi\}) | \Phi_R >$$

which is simply the relative coordinate Hamiltonian averaged over the relative coordinate wavefunction. This method of separating the center of mass and relative coordinates is in some ways like a Born-Oppenheimer approximation.

This method of approximation corresponds to a physical picture: A quantum soliton that propagates along a fiber may execute a weak transverse motion. When the transverse center of mass moves off center, it does so because the single photon states have developed an admixture from higher order fiber modes, which have a corresponding higher frequency. The total soliton energy is then greater, and this corresponds to a net dynamical motion of the transverse soliton center of mass. This transverse energy is split up in this picture into a kinetic contribution as defined within the framework of the paraxial approximation, and a potential contribution due to the presence of linear and nonlinear dielectric.

This model has been applied to the design of a quantum nonlinear Y-coupler and a nonlinear quantum directional coupler. Our initial effort focused on the design of a Y-coupler that would switch a quantum soliton initially in a single fiber into a superposition of two states corresponding to soliton propagation down one (or the other) of two exit fibers. The results of the analysis (figure 26) demonstrated clearly conditions for which adiabatic switching could produce such states in an ideal lossless coupler. Real fibers are lossy, and it was found that the characteristic switching length was greater than the single photon loss length. In prin-
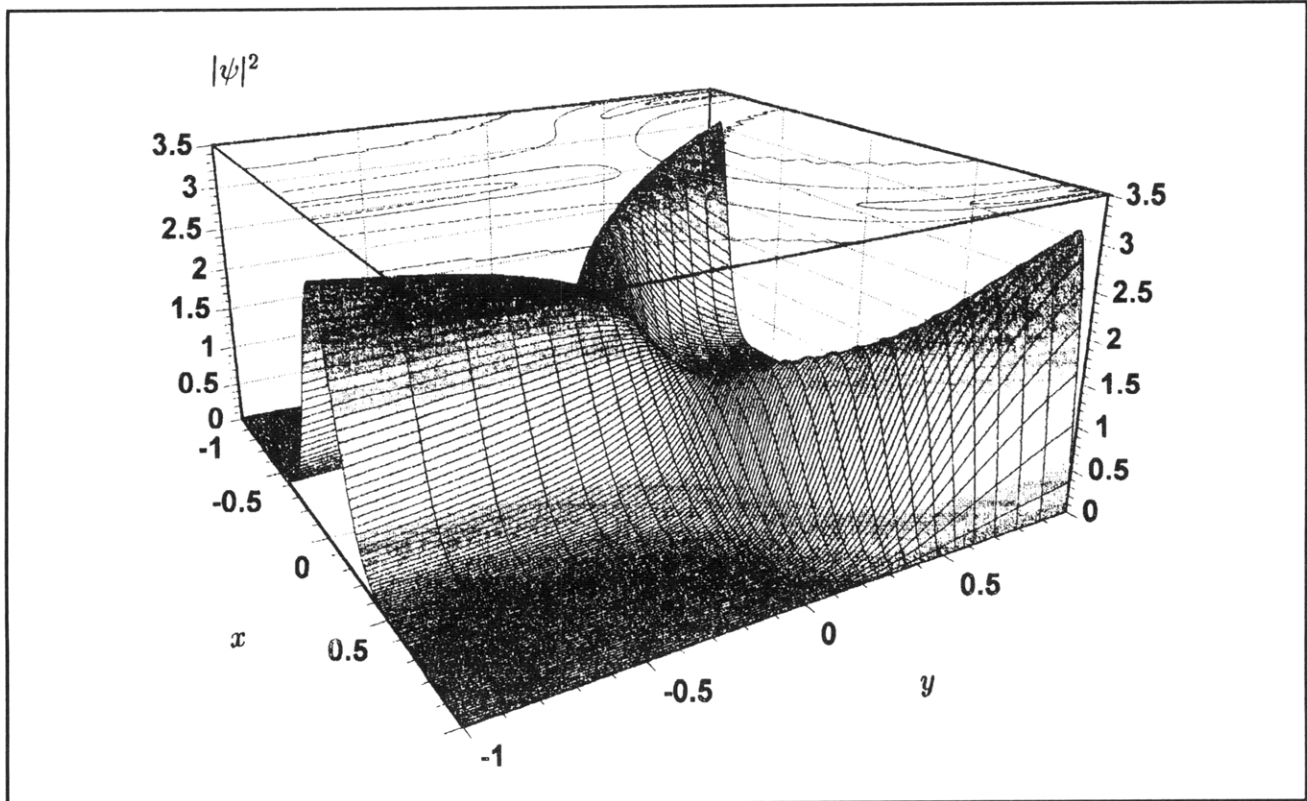

Figure 26. Wavefunction for the transverse center of mass for a quantum optical soliton in a Y-coupler in the adiabatic limit. The x-axis gives a normalized distance between the two fibers; the y-axis is a normalized measure of the strength of the nonlinear coupling relative to the splitting of the lowest modes (which corresponds to distance along the Y-coupler). On the left, the soliton is initially fractionated between the two couplers so that the center of mass is in the middle; on the right, the soliton is in a superposition of states of being mostly in one fiber or the other.

ciple, this implies that the desired superposition that would be required for the development of an interferometer could probably not be obtained. But even this conclusion is to some degree premature, as the question of the presence of an interference effect is known to depend on whether the results of the photon loss can be determined from a measurement. This problem is subtle; its resolution will ultimately require a combination of theoretical developments and an associated experimental effort.

A superior route towards resolution comes from consideration of the design of a quantum nonlinear directional coupler. In this case, the quantum soliton would switch by center of mass tunneling from one fiber to another, which can be accomplished much more easily than splitting the center of mass wavefunction between two fibers as in the case of the quantum nonlinear Y-coupler. The results of the configuration space model indicate that an ideal directional coupler can be readily designed that produces a quantum superposition for a macroscopic soliton. Once again, the switching length is found to exceed the single photon loss length.

While these initial results are either to be expected (since macroscopic quantum effects are at best elusive) or disappointing (since such a device would be extremely interesting), there are a number of variations of the initial approach that are of interest: (1) While it may not be possible to switch the soliton completely within a single photon loss length, it is certainly possible to generate other states that correspond to fractional splitting (like 60/40) which would show λ/n interference effects; (2) It is quite likely that the loss of a single or of a few photons will not destroy an interference pattern, as long as the loss is not measurable. Such questions will be of extreme interest if this field develops. (3) Much more relaxed constraints are obtained on the design of such optical elements if short pulses are used that are not solitons. It is not obvious whether the resulting states will exhibit quantum interference, but clearly there are interesting possibilities.

1.18.6 Application to Quantum Computation

There has been a growing realization that quantum computation, long considered to be highly speculative, is likely to have practical applications that are potentially important. The premise of quantum computation schemes is that extreme parallelism can be obtained by creating a computer that can be put into a quantum superposition of states. The computer then calculates and adjusts relative phases based on the results of the calculation. The result of the calculation is determined from a measurement of the state of the computer, and the answer will be probabilistic, reflecting the results of the calculations that were done in each state of the quantum superposition. The advantage of the approach over classical computation is that a single quantum computer can in principle be put into a superposition of perhaps 10^{100} states and perform computations that ultimately depend on the results of computations performed in each of these states. A highly parallel classical computer could not achieve equivalent computational power. The applications for such quantum computers, assuming that they can be developed, may be in the areas of factorization of large numbers and modeling of complex quantum systems (we will inevitably expect to see a new class of computer games).

We have been interested in the use of optical solitons and short optical pulses for a possible implementation of a quantum computer.[103] Nonlinear optical techniques can be used for fast switching, and low loss optical fibers are useful for applications in high bandwidth communications. Most current proposals for quantum computation involve the manipulation of electronic or nuclear spins or use of cavity QED techniques, both of which are very slow in comparison with optical switching. These proposals have the advantage that (1) they are based on experimentally demonstrated technology, (2) they provide an implementation of quantum computation on discrete bit, and (3) the associated phase coherence times are sufficiently long to allow on the order of perhaps 10^6 or more coherent quantum computations. Quantum computation with optical solitons could not achieve a competitive number of coherent quantum computations (intrinsic fiber loss produces an upper limit of about 10^3 coherent quantum computations in an ideal optical system).[104]

---

[103] P.L. Hagelstein, N. Margolus, and M. Biafore, "Towards an Optical Quantum Computer Project," unpublished (1994).

[104] P.L. Hagelstein, "Possibility of Quantum Computation Using Optical Pulses in Fibers," invited talk at the *First Japanese International Conference on Quantum Computation*, Osaka, Japan, December 1995.

Consequently, quantum computation based on optical pulses in fibers would not be competitive against the other leading approaches if the measure of quantum computational power is total number of coherent operations possible. There has been some exploratory discussion of the possibility of quantum error correcting schemes for quantum computation, which are at this point speculative relative the proposed applications. Should quantum error correction algorithms prove to be viable for quantum computation, then the the total number of coherent quantum computations would no longer be the dominant measure; instead, the rate at which quantum computation can be done will be more important. In this case, quantum computation based on optical technology has the potential to be faster by many orders of magnitude than the conventional approaches.[104]

Even if quantum error correction were shown not to be viable, there would still be an important reason to explore optical quantum computation. This is because the optical system is fundamentally a continuum quantum system, where groups of spins or two-state atomic systems constitute a discrete quantum system. The potential capabilities of discrete versus continuum quantum computers will be very different; the class of quantum problems that could be modeled using a continuum quantum computer represents a different class of problems than the class that can be modeled using a discrete quantum computer.[104]

1.18.7 Publications

Goodberlet, J., et al. "Observation of Gain in a Recombining H-like Boron Plasma." *J. Opt. Soc. Am. B* 12: 980 (1995).

Hagelstein, P.L. "Application of Photon Configuration Space Equations to Optical Soliton Propagation." *Phys. Rev. A.* Forthcoming.

Hagelstein, P.L. "Application of Photon Configuration Space Equations to Optical Soliton Center of Mass Interferometry." Submitted to *Phys. Rev. A.*

Hagelstein, P.L. "Application of Photon Configuration Space Equations to Optical Soliton Center of Mass Switching." Submitted to *Phys. Rev. A.*

Hagelstein, P.L. "New Lattice-nucleus Coupling Mechanisms and Possible Energy Production." *Proceedings of the Symposium on Fusion Engineering* (SOFE '95). Forthcoming.

Hagelstein, P.L. "Possibility of Quantum Computation Using Optical Pulses in Fibers." Invited talk at the *First Japanese International Conference on Quantum Computation*, Osaka, Japan, December 1995.

Hagelstein, P.L. "Many-Photon Configuration Space Equations." Submitted to *Phys. Rev. A.*
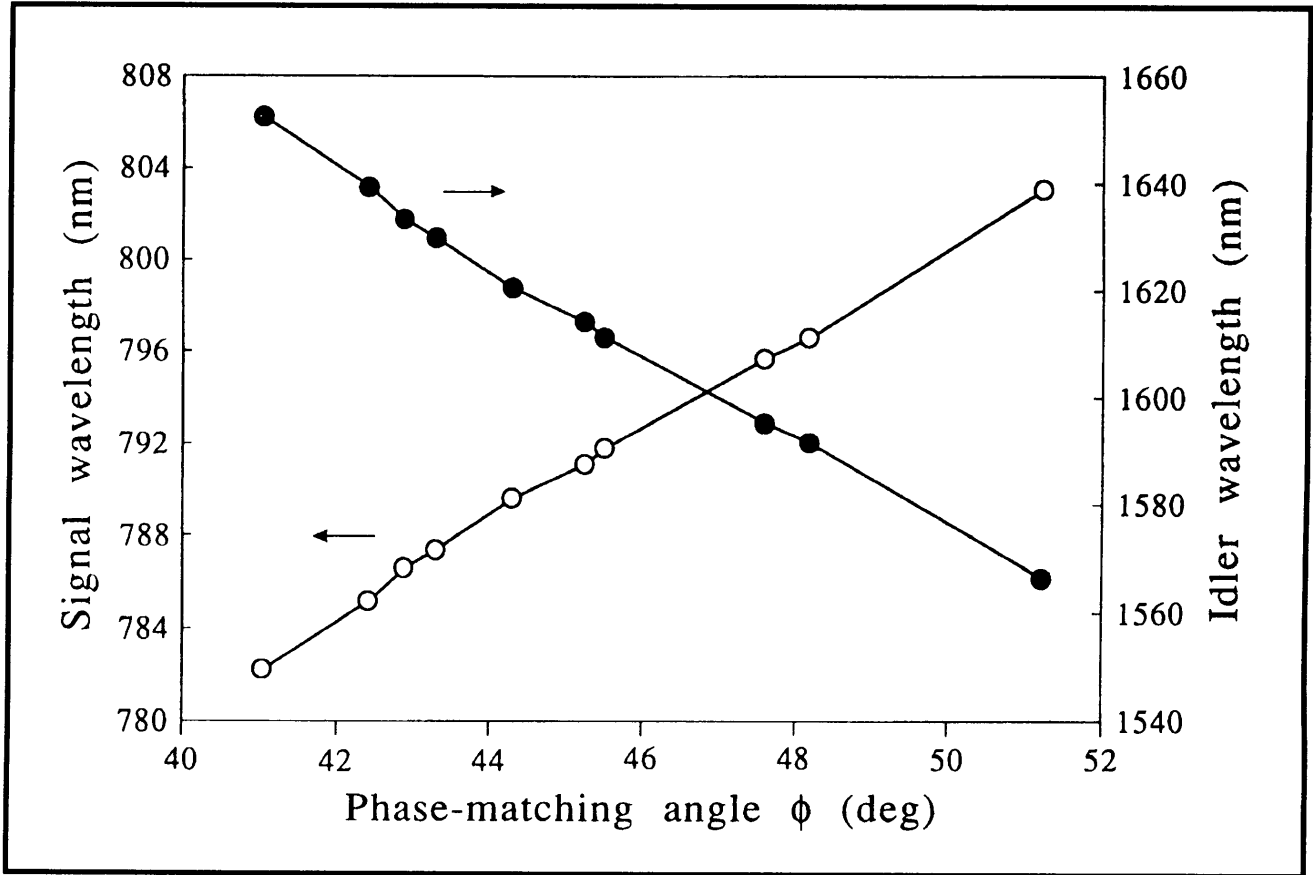
Tunable 1.6 μm source: Plot of input signal and output idler wavelengths versus internal CTA crystal phase matching angle φ for θ=90° and a pump wavelength of 531 nm.